Doctoral Thesis in Physics

Static and non-equilibrium magnetic proximity effects in $Pt/NiFe_2O_4$ and $Pt/Ni_{1-x}Fe_x$ heterostructures

Christoph Klewe

February 16, 2016

Bielefeld University
Department of Physics

Declaration

This work was done by myself. Text and figures were partly taken from corresponding publications, which originate directly from this work.

(Christoph Klewe)

Reviewers:

Prof. Dr. Günter Reiss

Prof. Dr. Thomas Huser

Bielefeld University, Department of Physics
Center for Spinelectronic Materials & Devices

Doctoral thesis
February 16, 2016

Contents

1 Introduction

The permanently growing requirements on computational processes urge the development of more and more powerful information technological devices. This ongoing progress can only be realized by pushing the limits of device sizes to continually smaller dimensions. Yet, the higher circuit densities consequently result in a rapidly increasing energy consumption in the respective applications. The generation of waste heat, mainly from Joule heating, represents a particularly large obstacle in this regard and prompts the search for more efficient methods of data processing and storage. The introduction of spintronics [1] marked a substantial advance in this field by combining conventional charge based electronics with the electron spin as an additional carrier of information. In particular, the generation, manipulation and detection of spin polarized currents constitute the basis for most spintronic effects and enable information transfer at lower charge current densities. However, despite this progress the power consumption still keeps rising and remains the most critical aspect in the development of modern information technology.

After the first report of a spin Seebeck effect in 2008 [2] and the discovery of the longitudinal spin Seebeck effect (LSSE) [3] in 2010 the new fields of spin caloric transport and more general spin caloritronics [4] were introduced, which focus on heat induced spin transport phenomena. While the first spin Seebeck experiment has been lively discussed and often could not be reproduced [5–8], the LSSE remains the most prominent spin caloritronic effect. It describes the generation of pure spin current in a ferromagnetic[1] insulator (FMI) by a temperature gradient. In the absence of

[1] For simplicity the term ferromagnetic is used to represent both ferro- and ferrimagnetism. Therefore, in what follows these two terms are implicitly considered when talking about ferromagnetism, unless stated otherwise.

mobile charge carriers in an insulating material the spin does not travel via motion of free electrons but is transported by magnonic spin waves. These spin waves propagate almost dissipationless, which makes the information transfer much less power consuming than via actual charge currents. This and the idea of utilizing waste heat in order to reduce energy consumption immediately excited a large interest in this field.

In particular, FMIs show a large potential for being implemented in spin caloric devices, while the application of ferromagnetic metals (FMM) can give rise to parasitic charge current effects, like the anomalous Nernst effect (ANE). These parasitic contributions can hamper an unambiguous observation of pure spin currents, while the lack of free charge carriers in insulating materials prevents the appearance of spurious effects and makes it possible to identify the observed spin current phenomena unequivocally.

In addition to the LSSE, a vast spectrum of other spin caloric and spintronic effects, like the recently observed spin Hall magnetoresistance (SMR) [9–12] also benefit from the suppression of charge currents in FMIs. In SMR based devices that consist of an FMI capped by a thin metal film, the insulating behavior of the FMI reduces electrical shorting through the magnetic layer and eliminates contributions from an anisotropic magnetoresistance (AMR). Therefore you can measure the SMR without parasitic effects [12]. These advances in the fields of spintronics and spincaloritronics promote the ongoing search for suitable FMIs to exhibit related effects, which are a lot more rare than their metallic counterparts.

The most frequently used paradigm system for such FMIs is the class of Fe based garnets, especially the heavily deployed Yittrium Iron Garnet (YIG - $Y_3Fe_5O_{12}$) [13], as it provides a considerable magnetic moment of about $5\,\mu_B$/f.u. [14, 15], i.e., 138 kA/m, while being a good electrical insulator with a band gap of $2.85\,\text{eV} - 2.88\,\text{eV}$ [16, 17]. But also other materials such as different compounds from the class of spinel ferrites, are ferromagnetic and insulating or semiconducting and thus exhibit all the attributes to be implemented in spin caloritronic devices.

In this regard, it is especially Nickelferrite (NFO - $NiFe_2O_4$) which shows interesting properties for studies on the outlined effects. Its less insulat-

ing character when compared to YIG gave rise to increased utilization of this material in spin caloric and spintronic experiments. The idea behind this was to use this particular property by observing changes in the LSSE/ANE signal when varying the electrical conductivity of NFO from a poorly conducting state at room temperature (RT) to a highly insulating state at low temperatures and, thus, to separate contributions from LSSE and ANE [18]. Analogously, these characteristics also promote investigations of the SMR in NFO based systems.

However, even the application of ferromagnetic insulating materials in spin caloric and spintronic experiments does not automatically enable a complete exclusion of charge carrier based parasitic effects. In contrast to the detection of conventional charge currents, the generation and observation of spin currents is far more challenging. One effective method to overcome this obstacle is converting the spin current generated in the ferromagnet (FM) into a conventional charge current via the inverse spin Hall effect (ISHE) in an adjacent non-ferromagnetic metal (NM). The ISHE is particularly strong in a number of heavy 5d transition metals with a large spin Hall angle, e.g., Ta, W, or Pt. Though, when Pt is used to detect spin currents in an attached magnetic film, a spin polarization in the Pt generated by a static magnetic proximity effect (MPE) might occur and induce additional spurious charge based effects. Thus, for the interpretation of experimental results, it is crucial to include and evaluate possible MPEs.

A common approach to measure the magnetic properties of a sample system element selectively is x-ray magnetic circular dichroism (XMCD). So far, two groups have investigated static MPEs in Pt/YIG structures, using XMCD though, with contradictory results. While Lu et al. observed an induced spin polarization in Pt when attached to YIG, Geprägs et al. did not find any evidence of magnetic proximity in their samples [19–21]. Similar XMCD measurements on Pt/$CoFe_2O_4$ (CFO) double layers did not yield any evidence of a static MPE [22]. Therefore, the question of a static MPE in Pt/FMI hybrids in general is still vividly discussed, but remains unanswered yet. One controversy in this context is the pronounced

film thickness dependence of XMCD, which may conceal small effects, if the Pt film thickness exceeds a few nm. Therefore, a more interface sensitive technique is needed in order to examine this more conclusively.

The first experimental chapter of this thesis focusses on the preparation of NFO thin films with different techniques for the application in spintronic and spin caloric devices. The film properties are studied in detail to obtain the optimum fabrication conditions and gain high quality samples. The fabricated films have already been successfully utilized in various investigations on the LSSE [23–25] and the SMR [12].

In order to rule out static MPE induced parasitic effects in these experiments, the interfacial magnetic properties of the Pt/NFO double layers will be adressed in the next chapter. In particular, x-ray resonant magnetic reflectivity (XRMR) is introduced as a powerful alternative to the commonly used XMCD when investigating interfacial spin polarizations, as it is highly interface sensitive and independent of the film thickness. Therefore, XRMR is well suited for studies on the static MPE. In addition to the XRMR measurements on Pt/NFO bilayers, auxiliary studies on YIG based heterostructures will be carried out for a more comprehensive analysis of the static MPE in Pt/FMI systems. Furthermore, the technique of XRMR will be explored in more detail and tested for its suitability for the observation of MPEs in different Pt/FMM reference samples. Especially, thickness independence as well as challenges in the quantitative analysis of experimental data are evaluated. The influence of the FM thickness and composition on the magnitude of the induced spin polarization is also monitored in different Pt/FM bilayer systems.

Finally, in the last chapter the Pt/NFO heterostructures will be tested for their magnetoresistive properties thus, their suitability in spintronic devices. In particular, the layers will be checked for the occurence of an SMR.

The majority of the results presented here have already been published in different peer-review journals or submitted for publication. The corresponding articles are referenced in the respective chapters.

2 Fundamentals

2.1 $NiFe_2O_4$ - Nickelferrite

A promising alternative to magnetic garnets for spin caloric and spintronic applications is the versatile class of spinel ferrites. A large number of these compounds exhibits ferrimagnetic and semiconducting or insulating properties making them particularly attractive for the observation of pure spin current effects. For example, the LSSE was already observed in (Mn,Zn)Fe_2O_4 [26], in $NiFe_2O_4$ [18], in $CoFe_2O_4$ [27,28] and in magnetite (Fe_3O_4) below the Verwey transition [29]. The class of spinel ferrites is characterized by the general formula AB_2O_4, where A and B denote divalent and trivalent cations, respectively. Each conventional unit cell of a spinel ferrite consists of 8 formula units AB_2O_4, leading to 32 divalent oxygen anions forming a face centered cubic structure within the unit cell. Two separate sublattices are formed, denoted as tetrahedral and octahedral, based on their coordination numbers 4 and 6 regarding the neighboring oxygen anions, respectively.

In this study, the focus is placed on the inverse spinel ferrite NFO, which shows both LSSE [18, 23] and SMR [12] in contact to a NM with a large spin orbit coupling. In the inverse spinel structure half of the B^{3+} cations reside on tetrahedral sites while the remaining B^{3+} and A^{2+} cations are located on octahedral sites [30]. For a better understanding of this complex lattice structure a schematic unit cell is illustrated in Fig. 2.1. In the case of NFO the A^{2+} correspond to Ni^{2+} cations and the B^{3+} cations resemble Fe^{3+} cations. The bulk lattice constant of NFO is 8.34 Å. Theoretically, NFO offers the advantage of switching on or off parasitic effects like the ANE by changing the probing temperature, due to its semiconducting character. The compound is a ferrimagnet below the

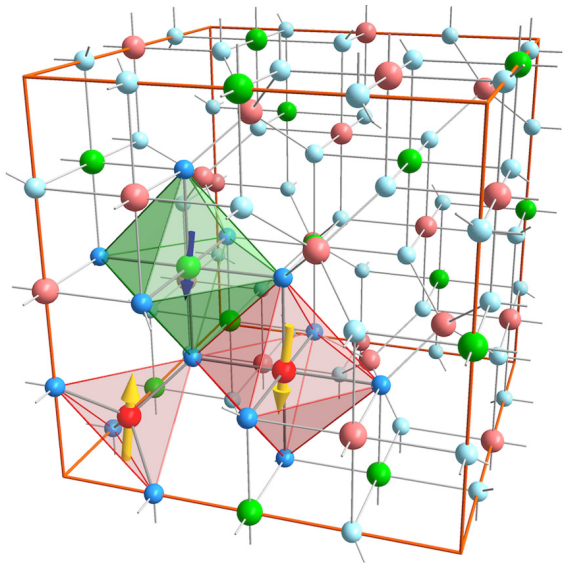

Fig. 2.1: Schematic depiction of the inverse spinel structure of NFO. The oxygen anions (blue spheres) are arranged in a face centered cubic lattice structure. Half of the Fe^{3+}, represented by red spheres, are statistically distributed across tetrahedral sites, while the remaining Fe^{3+} cations reside on octahedral sites. The Ni^{2+} cations (green spheres) are solely located on lattice sites with an octahedral configuration. Dissimilar lattice sites are antiferromagnetically coupled, while cations on equivalent positions exhibit a ferromagnetic order. The sketch was taken from Ref. [31] with permission from Physical Review B.

Curie temperature $T_C \approx 850\,K$ [32,33], with an antiferromagnetic coupling between the tetrahedral and octahedral sublattices. Even though NFO has been studied intensively for many years, there are still discrepancies in the literature values for the bulk magnetization, ranging approximately from 270 kA/m to 300 kA/m [34–36]. Theoretically, in the inverse spinel structure the magnetic moments from the antiferromagnetically coupled tetrahedral and octahedral Fe^{3+} sites cancel nearly exactly. Consequently, the macroscopic magnetization is mainly carried by the Ni^{2+} ions on the octahedral sites with a moment of about $2\,\mu_B$/f.u.. This value corresponds to a magnetization of about 256 kA/m.

The electronic structure of NFO shows a band gap around the Fermi level E_F. There are no consistent data on the width of the optical band gap of NFO in thin films available, but the experimental values are scattered in a large range between 1.5 eV and 4.3 eV [37–43]. Yet, the electronic properties are very sensitive to the structural quality. It has been suggested that the electric transport in ferrites is driven by charge carrier exchange between divalent and trivalent cations on equivalent lattice sites [44–46]. In the case of NFO, small amounts of excess Fe or Ni might enter the lattice on octahedral sites during the preparation process as Fe^{2+} or Ni^{3+} ions, respectively [44, 47]. Alternatively, an oxygen deficit could lead to incomplete oxidation of Fe atoms, generating Fe^{2+} instead of trivalent species. This promotes $Fe^{2+} \leftrightarrow Fe^{3+}$ or $Ni^{2+} \leftrightarrow Ni^{3+}$ hopping processes of electrons or holes, respectively [46, 48]. De Boer et al. proposed that such electron interchange processes require only little energy, as the charge carriers travel along the statistical cation distribution on the octahedral sites without altering the energy state of the lattice considerably [49]. Therefore, slight deviations from the correct stoichiometry resulting in Fe^{2+} or Ni^{3+} antisites in the octahedral sublattice can influence the electronic transport properties of NFO immensely.

2.2 Magnetic proximity effects

In general, the term magnetic proximity effect [50] is used when heterostructures of at least two materials with different long-range magnetic orderings in the immediate vicinity exhibit a transformation of their interfacial magnetic properties, due to a coupling with the respective other film. This is an important phenomenon under technological aspects, as these novel properties can create interesting new possibilities for applications, but can also interfere with well established effects. Therefore, it is crucial to ascertain the interfacial properties of magnetic composite structures carefully. When discussing MPEs, two different effects have to be considered separately. While the static MPE has been well known for decades, the non-equilibrium MPE was introduced just recently in the studies of

Nakayma et al. [9], Vlietstra et al. [11], and Althammer et al. [12] on the newly proposed SMR. Both effects manifest themselves in a similar phenomenon, i.e., the generation of spin polarization at the interfaces of a paramagnetic metal to a FM, but arise from very different origins.

2.2.1 The static magnetic proximity effect

The static MPE was already discussed in the 1950s - 1960s and is widely attributed to static magnetic exchange coupling across the interface of two materials. An early experimental study of this effect was carried out by J.J. Hauser in 1969, using the superconducting proximity effect [51]. By monitoring the superconducting transition temperature T_s in Pb-Pd-Cr and Pb-Pd-Fe, he observed a reduction of T_s with decreasing Pd thickness and thus showed that a Pd film in contact with ferromagnetic Fe and antiferromagnetic Cr is magnetized, i.e., exhibits spin polarization at the interface to the adjacent layer. For FM-Pd alloys a similar effect was reported even earlier [52, 53].

In general it is well understood that the static magnetic interface coupling associated with the MPE in thin film heterostructures is mainly governed by the interplay of two different mechanisms. In a description of the effect for ultra thin FM films of only a few monolayers on paramagnetic substrates, Cox et al. calculated that the strength of the magnetic coupling mainly depends on the degree of band hybridization at the interface and the occupancy of the interfacial band states around the Fermi level E_F [54]. Blügel et al. stated that these considerations are strictly valid only for films of a few monolayers thickness, while for deviating structures, i.e., in the dilute limit or for thicker films, exchange couling in terms of a Rudermann-Kittel-Kasuya-Yosida interaction (RKKY) additionally determines the interface magnetism [55–58]. In principle the RKKY interaction describes a coupling of localized spins mediated by conduction electrons. Consequently, both magnetic coupling via band hybridization as well as RKKY exchange interaction critically depend on the electronic properties of the materials, in particular the existence of electronic states around the Fermi level.

Furthermore, a possible expansion of the magnetization into a NM, i.e., a generation of a spin polarization at the interface of a NM/FM hybrid structure depends on the properties of the NM itself. Induced spin polarizations due to static MPEs are most likely to occur in strongly exchange enhanced Pauli paramagnets which are in close vicinity to the Stoner criterion [59], a simplified model to determine whether a material exhibits a spontaneous magnetization based on the minimization of the ground state energy. One practical expression of this rule is given within the formulation $I_\mathrm{F} \cdot N(E_\mathrm{F}) > 1$, where I_F is the exchange integral and $N(E_\mathrm{F})$ represents the density of states at the Fermi Level. These parameters can be directly determined from bandstructure calculations and, therefore, enable us to theoretically assess the occurrence of ferromagnetic order in a solid.

For the 3d transition metals Fe, Ni, and Co the Stoner criterion parameter exceeds the value one, making them ferromagnetic at finite temperatures. However, in materials where the Stoner criterion is missed closely, a perturbation like the exchange interaction with an adjacent FM film can alter the exchange energy enough to induce a spin dependent band splitting and, thus, a magnetic ground state in the NM.

A number of noble metals like Pt [60], Pd [52, 53, 61], and Ru [62], but also light transition metals like V [63] and Cr [64] are known to exhibit pronounced static MPEs in the proximity to a FM. Pt, for example shows a Stoner criterion parameter of $I_\mathrm{F} \cdot N(E_\mathrm{F}) \approx 0.6$ in its fcc and its hcp phase, while Pd even possesses a value of $I_\mathrm{F} \cdot N(E_\mathrm{F}) \approx 0.85$ in fcc configuration [65]. Hence these materials can easily be spin polarized.

Recently, Pt has been vividly discussed in this context, due to its application in a large number of spintronic and spin caloritronic studies. Besides the potential technological interest in novel interface properties in composite materials, an induced spin polarization in Pt adjacent to a FM can also generate new challenges when investigating certain effects. Especially pure spin current effects like the LSSE can be influenced by the presence of induced spin polarizations in a NM in terms of a static MPE. In particular, the possibility of additional static MPEs in heterostruc-

tures can give rise to alternative explanation models for the observed effects [66, 67] and renders the underlying theories questionable. The LSSE is commonly measured electrically by converting a spin current generated from an out-of-plane temperature gradient in a FMI into a detectable voltage via the ISHE in a NM. Thus, the observation of an LSSE requires the proximity of a NM to a FMI, which raises the question of static MPEs in NM/FMI heterostructures. An induced spin polarization in the NM could act as a FMM and again give rise to parasitic charge current effects like an ANE obscuring the LSSE [68]. Analogously, in measurements of the SMR, an apparent spin polarization in the NM created from a static MPE can promote the occurence of an AMR [69] and also hamper the observations.

Theoretically one would not expect a static MPE to occur in a NM/FMI bilayer, due to the lack of states around the Fermi level in the FMI. However, a large roughness, i.e., an intermixing of the NM and the FMI at the interface, or impurities and lattice imperfections might induce interface states around E_F in the FMI and enable a static MPE. Therefore, a careful examination of the NM/FM interface is imperative, in order to rule out parasitic effects when doing research in these areas. So far, there have been investigations of the interfacial magnetic properties of Pt/YIG bilayers by two different groups using XMCD to probe the Pt moment with contradictory results. Lu et al. found a significant spin polarization with an average moment of $0.054\,\mu_B$ per Pt atom at 300 K and $0.076\,\mu_B$ per Pt atom at 20 K in 1.5 nm Pt on YIG [19]. Geprägs et al., on the other hand, did not see evidence of a Pt spin polarization down to 1.6 nm Pt on YIG. For a 3 nm thick Pt layer they ruled out a moment up to an upper limit of $0.003\,\mu_B$ per Pt atom [20, 21]. Therefore, the question of static MPEs in Pt/YIG or more generally in NM/FMI heterostructures remains unanswered and is still controversially discussed in the scientific community.

2.2.2 Non-equilibrium magnetic proximity effects

Unlike the static MPE, the non-equilibrium MPE does not occur spontaneously in a heterostructure, but depends on the application of an external

perturbation, e.g., an electric current or a thermal gradient, to drive the system out of equilibrium. The first case is realized within experiments on the SMR in NM/FMI bilayers. When driving a charge current through a NM with a large spin orbit coupling (SOC), a spin Hall effect (SHE) can occur, which converts the charge current into a transverse spin current. The spin current then piles up to a spin accumulation, i.e., a spin polarization at the interfaces of the NM. Depending on the magnetization orientation of the underlying FM, the spins at the bottom interface are either "absorbed" in terms of a spin torque or "reflected" and converted back into a charge current via the ISHE. The result is a detectable change of the longitudinal resistance of the NM. Thus, the magnetic proximity to a FM alters the electronic properties of the NM. A more detailed description of the SHE and the SMR is given in section 2.3.2.

In LSSE experiments on NM/FMI bilayers a thermal gradient is applied perpendicular to the film planes, generating a spin current from the FMI into the NM, inducing a spin accumulation in the NM. Hence the application of a thermal gradient in such a structure alters the magnetic properties of a NM adjacent to a FMI. Strictly speaking, the LSSE only describes the generation of a spin current in a FM by an out-of-plane temperature gradient. However, the injection of this spin current into an adjacent NM can also be understood as a non-equilibrium MPE. The investigation of the LSSE will not be part of this work, but was mainly done by Daniel Meier within our work group [18, 23, 24].

The induced spin polarization from a static MPE and a non-equilibrium spin accumulation at the interfaces of a NM generated by the SHE differ fundamentally. In the case of a static MPE, the bandstructure is distorted and the bands are shifted via an exchange splitting in the NM, comparable to the bandstructure of a real FM. In the case of a non-equilibrium spin polarization, on the other hand, the bandstructure of the NM is not modified, but the occupancy of the spin-up and spin-down bands changes in terms of a shift of the chemical potentials for spin-up and spin-down electrons relative to each other. This also manifests itself in an imbalance of occupied states with spin-up and spin-down orientation and, thus, in

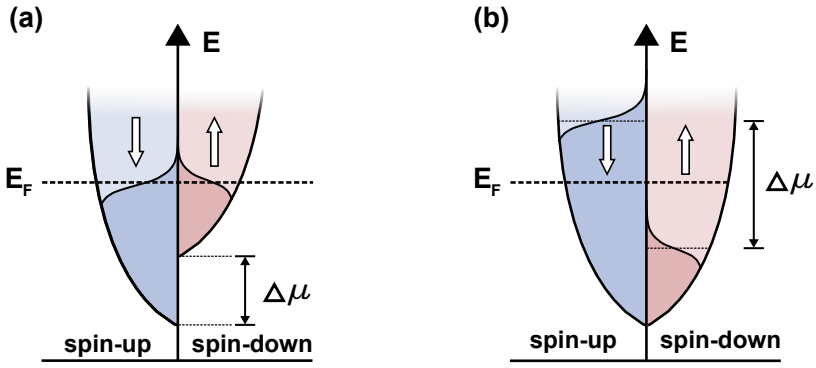

Fig. 2.2: (a) Schematic sketch of an exchange splitting $\Delta\mu$ of the spin-up and spin-down DOS in a FM. (b) Schematic sketch of a spin polarization due to shifted chemical potentials in the spin-up and spin-down DOS in a NM. The distribution function is shifted by a difference of $\Delta\mu$ in the chemical potentials μ for spin-up against spin-down.

a spin polarization. However, this phenomenon does not correspond to conventional ferromagnetism in terms of exchange splitting. This concept is sketched in Fig. 2.2.

2.3 Magnetoresistive effects

Magnetoresistance (MR) is the property of a material or a certain structure to show a change in resistivity depending on an external magnetic field or the magnetization of the system. At present, a large number of effects associated with MR are known and have a considerable impact on a wide range of technological applications, e.g., data storage devices or magnetic sensors. Recently, the SMR was added to this list. As described in section 2.2.2, the SMR is associated with a non-equilibrium MPE. Though there are no temperature gradients involved in the generation of this effect, it was found within the spin caloritronics community [9, 11, 12]. The motivation for this research was prompted by the unexpected finding of a magnetoresistive effect in Pt/YIG bilayers during studies on the LSSE in this system [66,70]. These first observations of an MR in Pt/YIG gave rise

to the assumption that the effect was actually caused by the well known AMR, due to a spin polarization present in the Pt layer, induced by a static MPE [66]. This explanation made the whole debate on the LSSE in Pt/YIG questionable, as a spin polarized Pt layer could induce parasitic charge current effects like the ANE contaminating the LSSE signal. Thus, a precise investigation of the magnetoresistance in systems commonly used for LSSE studies is indispensable for a clear understanding of the contributing effects. In particular, the distinct separation of contributions attributed to AMR and MR effects independent of an induced spin polarization in the Pt is in the focus of related investigations.

Furthermore, the AMR and the SMR exhibit a dissimilar dependence on the direction of an external magnetic field, which renders this novel effect particularly interesting for the development of new magnetic sensor systems.

2.3.1 The anisotropic magnetoresistance

The AMR was discovered in 1856 by William Thomson in Ni and Fe bulk samples [71]. Thomson found that the resistivity in these FMMs changes upon the application of an external magnetic field. However, in contrast to the colossal magnetoresistance, where the resistance change of a material in the presence of an external magnetic field is induced by the applied field itself, the AMR depends on the magnetization. Thus, the applied field only serves to manipulate the spontaneous magnetization of the material.

In a simplistic model the AMR can be understood by considering the charge distribution of the atoms in the crystal lattice, i.e., the atomic orbitals. Due to the spin orbit interaction the charge distribution is not spherical, but can be distorted for orbital quantum numbers $l \geq 1$. Since the asymmetry of the orbitals is connected to the spin angular momentum, the asymmetrical charge distribution follows the rotation of the spin when it is tuned in an external magnetic field. For different orientations of the electron orbitals with respect to the direction of the current this results

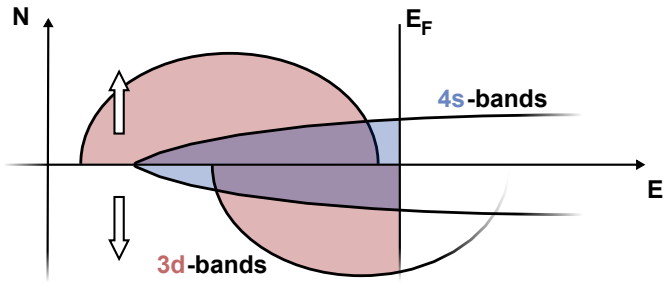

Fig. 2.3: Schematic depiction of a ferromagnetic 3d transition metal DOS with a bandgap in the spin-up 3d bands. The symmetrical 4s bands are displayed in blue and the exchange split 3d bands are shown in red.

in different scattering cross sections for the charge carriers and, thus, in a change of the resistivity for different magnetization orientations.

First explanations for the differences in the scattering cross section in 3d transition metals were given by Smit [72] and later by Campbell et al. [73] within the two channel conduction model by Mott, where the electrons are divided in spin-up and spin-down channels [74]. Mott assumed that the 4s electrons are primarily responsible for the electric current in a 3d transition metal. Therefore, the resistivity is mainly governed by scattering processes from s-states into unoccupied s- or d-states at the Fermi level E_F. He also assumed that during such a scattering event spin flip scattering processes are prohibited.

In Fig. 2.3 a scheme of the l-resolved density of states (DOS) for a ferromagnetic 3d transition metal (e.g., Fe) is illustrated. It is visible that there are states present at the Fermi level in both the spin-up and spin-down channel of the symmetrical 4s-bands of the conduction electrons, while for the 3d-bands only states in the spin-down channel are available around E_F. Since the DOS of the 3d-states is very large, s-d scattering potentially contributes as a major part to the resistivity. However, in the spin-up channel, the 3d-DOS does not provide unoccupied states at the Fermi level, allowing for only $4s_\uparrow - 4s_\uparrow$ transitions, while in the spin-down channel $4s_\downarrow - 3d_\downarrow$ transitions are also possible and contribute largely to the spin-down resistivity $\rho_\downarrow$. Hence, the spin-up resistivity $\rho_\uparrow$ is significantly

smaller than $\rho_\downarrow$, suggesting that the overall resistivity is mainly determined by $4s_\uparrow - 4s_\uparrow$ scattering.

However, this two channel conduction model in a 3d transition metal does not yield an explanation for an anisotropy in the resistivity as it does not account for spin orbit interactions. In the presence of SOC the d-bands exhibit an intermixing of spin-up and spin-down states, i.e., a small amount of $3d_\uparrow$-states is present in the $3d_\downarrow$-bands at E_F and vice versa. The $3d_\uparrow$-$3d_\downarrow$ mixing gives rise to $4s_\uparrow - 3d_\uparrow$ transitions into $3d_\uparrow$-states in the $3d_\downarrow$ dominated bands. Since the magnetization direction provides an axis for the spin orbit perturbation, this mixing of $3d_\uparrow$-states into the $3d_\downarrow$-bands is not isotropic. Therefore, an anisotropy exists in the resistivity depending on the magnetization orientation.

These considerations only give a simplified view on the origin of the AMR, but are convenient to get an idea of the principal mechanism of this spontaneous magnetoresistance anisotropy. As a result of the different scattering cross sections for different magnetization $\vec{M}$ orientations with respect to the electric current direction, the resistiviy in FMMs can vary by several percent. The AMR ratio is given by

$$\frac{\Delta\rho}{\rho_0} = \frac{\rho_\parallel - \rho_\perp}{\rho_0} \quad , \tag{2.1}$$

where $\rho_\parallel$ and $\rho_\perp$ are the longitudinal resistivity (resisitivity parallel to the probe current) for collinear and perpendicular magnetization-to-current configurations, respectively, and $\rho_0 = \frac{1}{3}(2\rho_\perp + \rho_\parallel)$ is an approximation for the isotropic resistivity of a fully demagnetized sample [75]. The longitudinal and transverse (resistivity transverse to the current) resistivities for a polycrystalline cubic sample as a function of the magnetization orientation can be written as

$$\rho_{\mathrm{long}} = \rho_\perp + (\rho_\parallel - \rho_\perp)m_\mathrm{j}^2 = \rho_\perp + \Delta\rho m_\mathrm{j}^2 \tag{2.2}$$

$$\rho_{\mathrm{trans}} = \Delta\rho m_\mathrm{j} m_\mathrm{t} - \rho_2 m_\mathrm{n} \tag{2.3}$$

where m_j, m_t, and m_n are the projections of the magnetization unit vector $\vec{m} = \frac{\vec{M}}{|\vec{M}|}$ on the axes parallel to the current (j), in-plane transverse to the current (t), and out-of-plane, i.e., parallel to the surface normal (n). In an analogous expression for the angle dependence of the resistivity on the magnetization direction, one can write

$$\rho_\mathrm{long} = \rho_\perp + \Delta\rho \cdot \cos^2(\theta_\mathrm{jM}) \tag{2.4}$$

$$\rho_\mathrm{trans} = \frac{\Delta\rho}{2} \sin(2\theta_\mathrm{jM}) \tag{2.5}$$

with θ_jM, the angle between the current direction j and the magnetization $\vec{M}$. Eq. (2.4) describes the behavior of the longitudinal resistivity under a rotating magnetization for a polycrystalline cubic sample.

Eqs. (2.2) and (2.3) were extended by Limmer et al. [76] for single-crystalline ferromagnetic materials with a cubic or tetragonal crystal structure, based on a series expansion in an analogous Ansatz to that of Birss [77] and Muduli et al. [78]. From Ohms law one obtains for the longitudinal and transverse resistivity

$$\rho_\mathrm{long} = \frac{E_\mathrm{long}}{J} = \vec{j} \cdot \bar{\rho} \cdot \vec{j} \tag{2.6}$$

$$\rho_\mathrm{trans} = \frac{E_\mathrm{trans}}{J} = \vec{t} \cdot \bar{\rho} \cdot \vec{j} \tag{2.7}$$

with the resistivity tensor $\bar{\rho}$ and $\vec{j}$ and $\vec{t}$ the unit vectors in the direction of the current J and the transverse direction t, respectively. The resistivity tensor $\bar{\rho}$ depends on the magnetization orientation $\vec{m}$ with respect to the crystallographic axes. Thus, it is necessary to determine a relation between ρ_long, ρ_trans, and the direction cosines m_i of $\vec{M}$, in order to model the experimentally accessible resistivities. Using Einstein's sum convention, $\bar{\rho}$ can be written as a series expansion in powers of m_i as

$$\rho_\mathrm{ij} = \alpha_\mathrm{ij} + \alpha_\mathrm{ijk} m_\mathrm{k} + \alpha_\mathrm{ijkl} m_\mathrm{k} m_\mathrm{l} + ... \quad . \tag{2.8}$$

Using the Onsager relations for cubic symmetry and inserting the resulting resistivity tensor into Eqs. (2.6) and (2.7) yields the expressions

$$\rho_{\text{long}}^{\text{cubic}} = A + C(\vec{j} \cdot \vec{m})^2 + (B - C) \sum_i j_{\text{i}}^2 m_{\text{i}}^2 \tag{2.9}$$

$$\rho_{\text{trans}}^{\text{cubic}} = C(\vec{j} \cdot \vec{m})(\vec{t} \cdot \vec{m}) + (B - C) \sum_i t_{\text{i}} j_{\text{i}} m_{\text{i}}^2 - D(\vec{n} \cdot \vec{m}) \tag{2.10}$$

for the longitudinal and transverse resistivity of a cubic system. The terms A, B, C, and D are resistivity parameters and consist of different combinations of the expansion coefficients α from Eq. (2.8). Applying the relation

$$m_{\text{i}} = j_{\text{i}}(\vec{j} \cdot \vec{m}) + t_{\text{i}}(\vec{t} \cdot \vec{m}) + n_{\text{i}}(\vec{n} \cdot \vec{m}) \tag{2.11}$$

to Eqs. (2.9) and (2.10) allows to calculate the longitudinal and transverse resistivities depending on the experimental conditions, e.g., crystalline texture, current- and field-direction. Averaging the summation terms in Eqs. (2.9) and (2.10) over all possible crystal orientations in space again leads to the expression (2.4) for a polycrystalline AMR.

A more detailed description of the calculations presented here is given in the works of Limmer et al. [76], McGuire et al. [75], Birss [77], and Muduli et al. [78]. In a complementary work, Limmer et al. [79] extended their calculations to the fourth order in the series expansion.

2.3.2 The spin Hall magnetoresistance

In order to tackle the SMR it is important to establish a solid understanding of the SHE first, as this is the driving force for the SMR.

Spin Hall effect For the description of the spin Hall effect it is convenient to distinguish clearly between the terms spin current and spin polarized current. The term spin current describes a pure transport of spins in a certain direction without an additional charge transfer in the same direction. This can be realized either by charge carriers of different spin directions traveling in opposite directions, such that the net charge

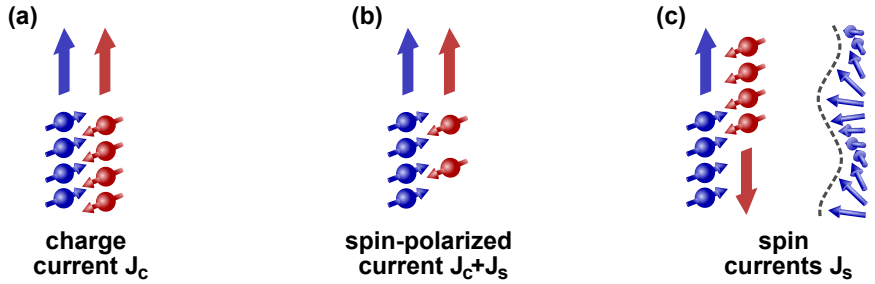

Fig. 2.4: (a) Conventional charge currents are generated by electrons of different spin orientations traveling in the same direction. (b) Spin-polarized currents are created by an imbalance of electrons with opposite spin traveling in the same direction. (c) Spin currents are created either by electrons with opposite spins traveling in opposite directions or by magnonic spin waves, transporting angular momentum via collective motion.

transport is zero, or by spin waves, so-called magnons, via a collective motion of coupled spin momenta. Spin polarized currents, on the other hand, transport both charge and spin momentum, due to an imbalance of spin-up and spin-down charge carriers in the electric current. Both phenomena are sketched in Fig. 2.4.

Phenomenologically, the SHE is the generation of a pure spin current perpendicular to an applied charge current. Therefore, it shows great potential for technological applications as a source of spin currents, which can be used to excite magnonic spin waves in FMIs or to switch the magnetization in an FM. It was already discussed theoretically by Dyakonov and Perel in 1971 [80] and shortly after by the groups of Lewiner and Nozières [81, 82]. Inspired by these considerations, the first experimental confirmation of the effect was given in 1972 by Chazalviel and Solomon, who measured the SHE quantitatively in InSb and later in Ge via spin-resonance experiments [83, 84]. After these studies the SHE was sparsely investigated, but was brought back to general attention and named almost 25 years later by Hirsch [85]. The first experimental confirmation after this revival of the SHE was presented by Kato et al. in 2004 [86], who used the magnetooptic Kerr effect (MOKE) to probe a spin accumulation transverse to a charge current in the non-magnetic semiconductor GaAs.

As the name already suggests, the SHE is closely related to the anomalous Hall effect (AHE). Both effects originate from an SOC; however, unlike the AHE and the ordinary Hall effect, the SHE is independent of the magnetization or the external magnetic field, but is solely determined by the strength of the spin orbit interaction. In fact, the AHE originates from the same mechanisms and can be understood as a special case of the SHE in an FMM. Here, the finite spin polarization of the initial charge current, due to the exchange splitting of the FMM bandstructure, creates an imbalance in the spin dependently scattered charge carriers, resulting in a net charge separation and an emerging voltage transverse to the applied current.

In the presence of a pronounced SOC, e.g., in a paramagnetic metal like Pt, the differential cross section for scattering at impurity atoms exhibits an asymmetrical contribution with respect to the spin state of the conduction electrons, leading to an effective spin separation and, thus, a spin current. A figure of merit for the efficiency of the charge-spin current conversion is given by the ratio between the spin Hall conductivity σ_{SH} and the electric conductivity σ, i.e., the spin Hall angle $\alpha_{\mathrm{SH}} = \frac{\sigma_{\mathrm{SH}}}{\sigma}$. The spin Hall angle basically determines the amount of spin current generated from a charge current and can theoretically attain values between 0 and 1. A relation between the induced spin current density $\vec{J}_{\mathrm{s}}$ and the applied charge current density $\vec{J}_{\mathrm{q}}$ can then be written as

$$\vec{J}_{\mathrm{s}} = \alpha_{\mathrm{SH}} \left(\frac{-\hbar}{2e} \right) \vec{J}_{\mathrm{q}} \times \vec{s} \quad , \tag{2.12}$$

with the spin polarization vector $\vec{s}$ pointing in the direction of the spin momentum [12, 87]. The counterpart of the SHE, i.e., the generation of a transverse charge current as a response to an initial spin current, is the ISHE, which is analogously defined as [87, 88]

$$\vec{J}_{\mathrm{q}} = \alpha_{\mathrm{SH}} \left(\frac{2e}{\hbar} \right) \vec{J}_{\mathrm{s}} \times \vec{s} \quad . \tag{2.13}$$

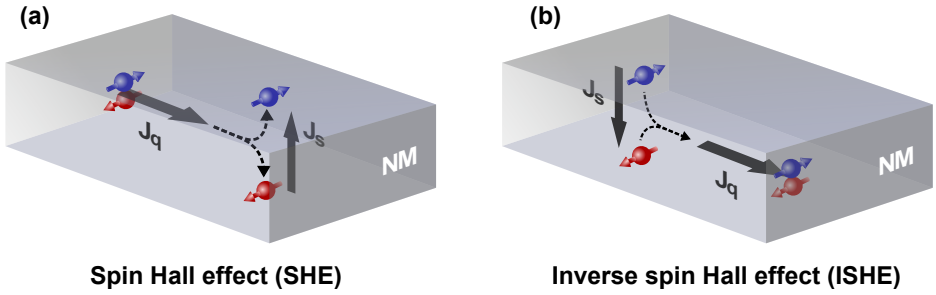

Fig. 2.5: (a) Conversion of a charge current into a transverse spin current via the SHE. (b) Conversion of a spin current into a transverse charge current via the ISHE.

The ISHE has become established as an effective tool to observe spin currents by converting them into a detectable voltage V_{ISHE}, e.g., in LSSE studies or in spin pumping experiments. The cross product in Eq. (2.12) indicates that the vectors $\vec{J}_{\mathrm{s}}$ and $\vec{J}_{\mathrm{q}}$, as well as $\vec{J}_{\mathrm{s}}$ and $\vec{s}$ are oriented orthogonally. Analogously, in Eq. (2.13) the vectors $\vec{J}_{\mathrm{q}}$ and $\vec{J}_{\mathrm{s}}$, as well as $\vec{J}_{\mathrm{q}}$ and $\vec{s}$ are orthogonal. Both the SHE and the ISHE are sketched in Fig. 2.5.

The spin Hall angle α_{SH} is a material specific property depending on the SOC. Especially heavy 5d transition metals like Ta, W, and Pt have been shown to exhibit a pronounced SHE with spin Hall angles of the order of $10^{-2} - 10^{-1}$ [89–91].

The microscopic mechanism behind the SHE consists of three different contributions, including skew-scattering, side-jump scattering, and an intrinsic contribution.

Skew-scattering As the name implies, the skew-scattering mechanism corresponds to an asymmetrical scattering of conduction electrons at impurities depending on the spin momentum of the electron [92]. Considering an electron moving in the vicinity of an impurity charge center, the impurity acts as a moving charge in the reference frame of the electron, inducing a magnetic field perpendicular to the electron trajectory. Since the induced field is inhomogeneous in space, i.e., it decays with the distance from the center, a spin dependent force acts on the electron due to

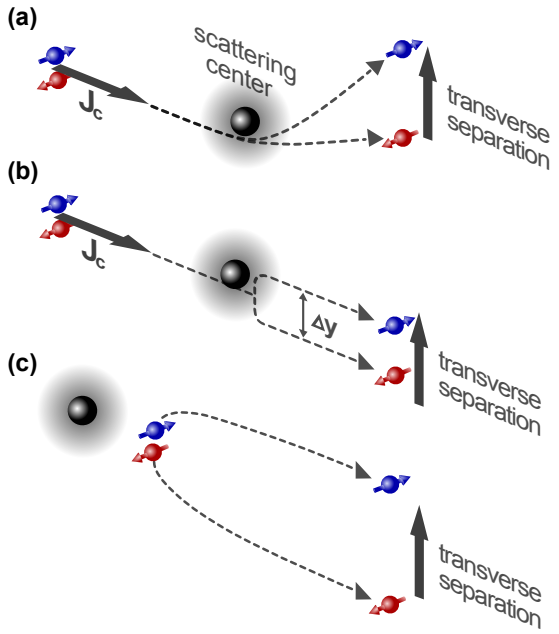

Fig. 2.6: (a) Skew-scattering mechanism. (b) Side-jump mechanism. (c) Intrinsic contribution.

a gradient in the Zeemann energy, leading to asymmetry in the scattering cross section for electrons of opposite spin. This process is displayed in Fig. 2.6(a). Mathematically, the skew-scattering can be treated within a spin orbit part $\propto \vec{s} \cdot \left(\vec{k} \times \vec{\nabla} V(q)\right)$ of the scattering potential, which leads to an asymmetrical contribution to the scattering cross section, i.e., to different scattering probabilities [93].

Side-jump-scattering Like skew-scattering, the side-jump mechanism also corresponds to an asymmetry in the scattering of conduction electrons at impurities with respect to their spin orientation. It was proposed by Berger [94] that a free electron, represented by a wave packet, traveling in x-direction and scattered at a central potential in the presence of a spin orbit coupling makes a small abrupt side jump Δy from its original trajectory, depending on its spin angular momentum (see Fig.

2.6(b)). Note that besides the sideways displacement a longitudinal component Δx occurs as well, but it does not contribute to the SHE. Usually, skew-scattering and side-jump-scattering are superimposed in a spin dependent scattering event, resulting in a small offset from the scattering center for the intersection of the electron trajectory before and after the scattering process. Unlike skew-scattering, which can be explained within the classical Boltzmann transport theory, the side-jump-mechanism is a non-classical effect [94]. The sideways displacement arises from a local distortion of the electron wave function at the impurity, generating a local current density. Typically the side-jump contribution is of the order of 10^{-11} m to 10^{-10} m and, thus, can become relevant for the SHE in the thin film regime for films with an electron mean-free-path (MFP) in the range of 10^{-9} m to 10^{-8} m.

It has to be noted that this description corresponds to a very simplified model. In fact the side-jump mechanism is a higher order effect and the net displacement does not arise from a single scattering event, but is the result of multiple scattering events.

Intrinsic contribution In addition to the asymmetrical scattering terms, a third, intrinsic contribution influences the SHE. While skew-scattering and side-jump correspond to a transversal asymmetry of the spin distribution from asymmetrical scattering at impurities, the intrinsic contribution influences the electron trajectory directly during the acceleration in between the scattering events by adding a transverse velocity (see Fig. 2.6(c)) [95]. Thus, the number of impurities does not explicitly determine this mechanism, but it strongly depends on the band structure of the ideal crystal. In principle, the intrinsic contribution originates from the precession of the spins around an effective magnetic field $B(k)$, depending on the wave vector k, which characterizes the band structure. The application of an electric field introduces a shift $\mathrm{d}k$ to the Fermi distribution in k space, driving it out of equilibrium [96]. The change in k and, thus, in $B(k)$ drags the spins out of alignment with the effective field. In order to realign with the field, the spins are canted with respect to

their original direction. The canting acts in opposite directions on the opposing sides of the Fermi surface, resulting in an effective spin current [96].

The contribution of each single mechanism to the SHE and their experimental separation are still vividly discussed [97, 98]. For example, Shushkov et al. [99] stated that the contribution from side-jump-scattering is more or less irrelevant compared to the skew-scattering. In contrast, different groups reported that this depends on the impurity ratio and the temperature range [94, 100, 101]. However, for the considerations of the SMR in this thesis mainly the phenomenology of the SHE and the ISHE, i.e., the generation of a transverse spin current in response to an applied electric field or vice versa, is of important relevance.

Experiments in the groups of Saitoh, Bauer, Goennenwein, and van Wees [9, 11, 12] on Pt/FMI hetereostructures showed that a thin film of Pt adjacent to an FMI exhibits an MR effect, which could not be explained by any of the well known MR effects, like AMR, colossal MR, positive MR, etc.. Even though sweeping the magnetic field between negative and positve values resulted in the typical major loop curves and promoted an explanation within the well known AMR model [19,66], $B-$field rotational measurements revealed that the observed MR deviates significantly from the AMR characteristics. Hence, they claimed that the origin of this new MR effect had to be different.

The first explanation for the observed results was given within the theory of the SMR [9–12]. Within this model, the SMR is explained by the interplay of the SHE, the ISHE, and a magnetization dependent spin torque, apparent at the interface of the NM and the FMI. The application of an in-plane electric field to an NM/FMI bilayer drives a charge current through the NM. If the NM exhibits a strong SOC, part of the charge current is converted into a transverse spin current via the SHE. The out-of-plane directed spin current amounts to a spin accumulation, i.e., a spin polarization at the NM interfaces. For the treatment of the SMR it is sufficient to consider only the fraction of the spin current deflected towards

the NM surface and the NM/FMI interface. However, it has to be noted that the SHE also creates spin currents in directions different from the plane normal. Depending on the magnetization orientation of the FMI the spin angular momenta deflected towards the NM/FMI interface can exert a torque on the FMI at the interface [10]. This spin torque transfer is covered in the Landau-Lifschitz-Gilbert-Slonczewski equation

$$\frac{\partial \vec{m}}{\partial t} = -\gamma \vec{m} \times H_{\text{eff}} + \alpha \vec{m} \times \frac{\partial \vec{m}}{\partial t} + \tau_{\text{s}} \tag{2.14}$$

by the Slonczewski term

$$\tau_{\text{s}} \propto \vec{m} \times (\vec{m} \times \vec{s}) \quad . \tag{2.15}$$

The Slonczewski spin torque term describes the transfer of spin angular momentum from the electron to the FMI. The gyromagnetic ratio γ gives the ratio between the electron's spin angular momentum and its magnetic moment. From the cross product in τ_{s} it is instantly clear that the spin torque term is maximum for a perpendicular arrangement of the spin and the FMI magnetization and vanishes for a collinear configuration. Therefore, in the case of a parallel or antiparallel orientation of the FMI magnetization regarding the spin no momentum transfer occurs and an equilibrium between the SHE induced spin current towards the NM interfaces and a diffusive spin current in the opposite direction builds up. In a simplified picture this mechanism can be understood as a reflection of the spin current at the interfaces, in which the spin direction is conserved. Analogously to the SHE, the back flowing spin current is converted to a charge current via the ISHE and again contributes to the initial charge current. In this equilibrium state, which corresponds to an open circuit condition, the resistivity of the NM is independent of the FMI.

If the magnetization of the FMI is aligned perpendicular to the spin polarization vector, the spin torque is maximum and a considerable fraction of the spins transfers angular momentum onto the FMI, resulting in a reorientation with respect to their former direction. This "absorption" of spin angular momentum reduces the back-flow of spins and thus re-

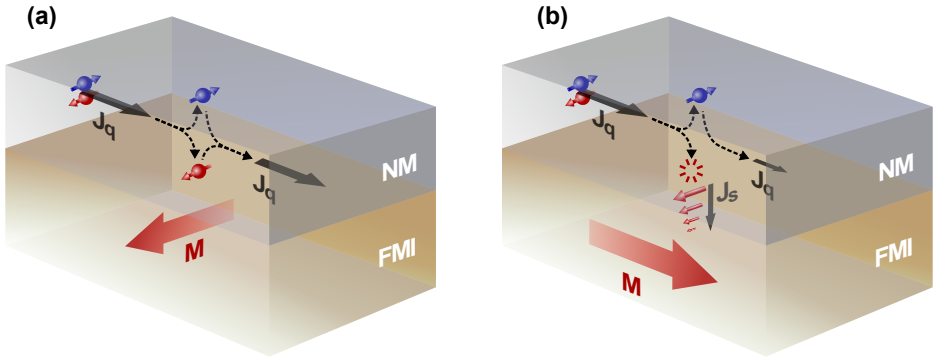

Fig. 2.7: The charge current J_q is converted via the SHE into a spin current J_s. (a) J_s is reflected at the NM/FM interface if the magnetization M is aligned collinear with the spin direction. (b) J_s is absorbed at the NM/FM interface, if the magnetization M is oriented perpendicular to the spin direction.

duces the ISHE contribution to the initial charge current (closed circuit condition). An illustration of these principles is sketched in Fig. 2.7. In the following the two different mechanisms will be referred to as reflection and absorption. As a result, the conductivity for magnetization orientation perpendicular to the spin orientation is reduced compared to a collinear alignment. This change in resistivity is the SMR.

Unlike the AMR, which depends on the angle between the magnetization $\vec{M}$ of the FMM and the direction of the charge current $\vec{J}_q$, the SMR depends on the angle between $\vec{M}$ and the spin polarization vector $\vec{s}$ of the conduction electrons deflected towards the NM/FMI interface. Since the spin polarization $\vec{s}$ and the charge current direction $\vec{J}_q$ are orthogonal, the SMR and the AMR can easily be distinguished in rotational $\vec{B}$-field measurements. Three possible measurement geometries are sketched in Fig. 2.8. The different geometries are denoted with ip (in-plane rotation), oopj (out-of-plane rotation around the current direction j), and oopt (out-of-plane rotation around the transverse axis t).

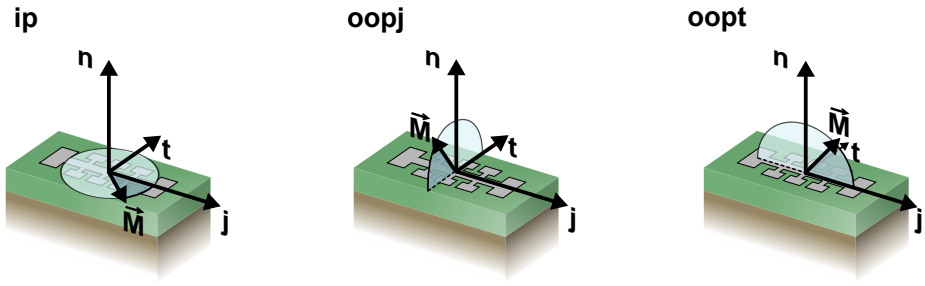

Fig. 2.8: Schematic sketch of three different rotational measurement geometries, allowing to distinguish between AMR and SMR. In the in-plane (ip) geometry the magnetic field is rotated in the film plane around the film normal n. In the two out-of plane geometries the magnetic field is rotated either around the current direction j (oopj) or around the transverse axis t (oopt).

The longitudinal resistivity in the AMR follows the well known $\vec{m}_\mathrm{j}^2$ behavior (see Eq. (2.2)), while the SMR obeys an $\vec{m}_\mathrm{t}^2$ dependence given by

$$\rho_\mathrm{long} = \rho_0 + \rho_1 \cdot m_\mathrm{t}^2 \quad , \tag{2.16}$$

where $|\frac{\rho_1}{\rho_0}| = \frac{\Delta\rho}{\rho_0}$ quantifies the SMR amplitude. Note that in this definition by Althammer et al. ρ_1 takes negative values and ρ_0 corresponds to the resistivity when $\vec{M}$ is perpendicular to $\vec{s}$, i.e., the resistivity is at its maximum [12]. Expanding this to an angle dependent equation gives

$$\rho_\mathrm{long} = \rho_0 + \rho_1 \cdot \cos^2(\theta_\mathrm{tM}) \quad , \tag{2.17}$$

with θ_tM, the angle between the direction $\vec{t}$ transverse to the current and the magnetization $\vec{M}$, analogous to Eq. (2.4) for the AMR. For a correct understanding of the different geometries of the AMR and the SMR, the two effects are sketched exemplarily for the different rotational measurement geometries in Fig. 2.9.

The transverse resistivity follows the same behavior as in the AMR case, which can be expressed as

$$\rho_\mathrm{trans} = \rho_2 m_\mathrm{n} + \rho_3 \cdot m_\mathrm{j} m_\mathrm{t} \quad . \tag{2.18}$$

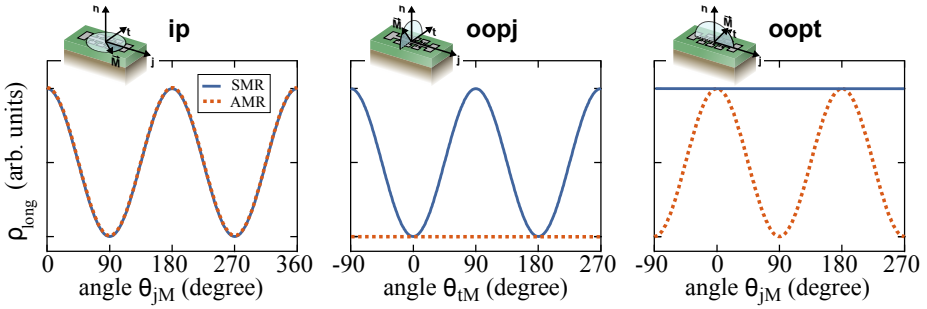

Fig. 2.9: Illustration of the angular dependence of the longitudinal resistivity for three different magnetic field rotation experiments. The corresponding measurement geometries are sketched in the repective insets, analogously to Fig. 2.8.

Thus, it is not suitable for distinguishing between the two effects.

The relative magnitude of the SMR can be calculated using the equation [10]

$$-\frac{\rho_1}{\rho_0} = \frac{\alpha_{\mathrm{SH}}^2(2\lambda_{\mathrm{NM}}^2\rho_{\mathrm{NM}})(t_{\mathrm{NM}})^{-1}G_{\mathrm{r}}\tanh^2\left(\frac{t_{\mathrm{NM}}}{2\lambda_{\mathrm{NM}}}\right)}{1+2\lambda_{\mathrm{NM}}\rho_{\mathrm{NM}}G_{\mathrm{r}}\coth\left(\frac{t_{\mathrm{NM}}}{\lambda_{\mathrm{NM}}}\right)} \quad . \tag{2.19}$$

The SMR is mainly governed by the thickness t_{NM}, the resistivity ρ_{NM}, the spin Hall angle α_{SH}, and the spin diffusion length λ_{NM} of the NM, i.e., the effective traveling distance during which the spin orientation is conserved. Furthermore, the real part G_{r} of the spin-mixing interface conductance is a measure for spin transport efficiency across the interface and affects the magnitude of the SMR.

In real SMR and AMR experiments magnetic anisotropies of the FMI have to be considered. Under the assumption of a single domain like switching, where the magnitude of $\vec{M}$ is nearly constant and only its direction changes in a rotating external magnetic field $\vec{H}$, magnetic anisotropies manifest themselves in a discrepancy of the angles (α, γ) and $(\alpha_{\mathrm{H}}, \gamma_{\mathrm{H}})$, where α and γ are the azimuthal and polar angles of $\vec{M}$, respectively, and α_{H} and γ_{H} represent the experimentally accessible angles of the applied

field $\vec{H}$. This discrepancy arises from the fact that the magnetization $\vec{M}$ and the external field $\vec{H}$ are not always parallel, but are aligned such that the free enthalpy G of the system is minimized [76]. In the presence of magnetic easy directions, the minimum value of the enthalpy is not necessarily reached when the magnetic field and the magnetization are parallel. The NFO samples investigated in this study primarily show a strong shape anisotropy resulting in a magnetic hard axis perpendicular to the (001) film plane, while other contributions can be neglected already at a small external field. Thus, the normalized enthalpy $G_{\mathrm{M}} = \frac{G}{M}$ can be written as

$$G_{\mathrm{M}}^{(001)} = -\mu_0 \vec{H} \cdot \vec{m} + B_{(001)} (\vec{n} \cdot \vec{m})^2 \quad , \tag{2.20}$$

where the first term refers to the Zeemann energy and the second term to a uniaxial perpendicular anisotropy with the anisotropy parameter $B_{(001)} = \mu_0 2\pi M_{\mathrm{eff}}$ and the effective magnitude of the magnetization M_{eff}.

It has to be acknowledged that Kobs et al. [103] and Lu et al. [67] have also reported SMR like effects in both Pt/FMM and Pt/FMI structures, yet, attributed their findings to alternative effects in terms of an anisotropic interface magnetoresistance (AiMR) and a so-called new Hybrid MR, respectively. However, they did not provide a conclusive microscopical explanation for the observed MR effects. Therefore, these interpretations are not detailed in this study.

2.4 Synchrotron radiation techniques

Since Wilhelm Conrad Röntgen received the first Nobel prize in physics for his discovery of x-rays [102], a large number of different characterization techniques to investigate the crystal structure (XRD, XRR, etc.), electronic structure (XANES, angle resolved XPS, EXAFS, etc.), and composition (XRF, XPS, EDX, etc.) of condensed matter has been developed. Especially the fact that x-rays enable a non-destructive insight into regions buried deep within the investigated structures makes these techniques extremely powerful. With the advent of sophisticated x-ray sources like

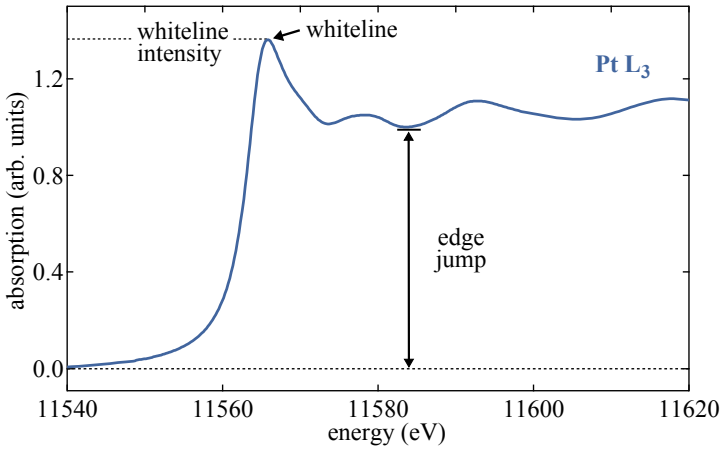

Fig. 2.10: Normalized L_3 absorption edge of Pt, as derived from *ab initio* calculations performed by Dr. Markus Meinert. The edge jump, whiteline, and whiteline intensity are displayed in the graph.

modern synchrotron facilities a new field of advanced measurement methods was established, which also allows for element specific characterization of the magnetic properties of materials. Today, a common approach to investigate the characteristics of nanoscopic heterostructures with a special focus on their magnetic properties is the application of XMCD in absorption and x-ray resonant magnetic scattering (XRMS). These techniques can provide magnetic, electronic and orbital information with element and valence specificity directly sensitive to the absorber site. The high element specificity is gained by the application of photon energies around resonant absorption edges of the probed material.

Such a resonant absorption or scattering state is reached for certain photon energies of the incident x-ray beam. For photon energies close to the element specific binding energy, i.e., where the resonance condition $\hbar\omega \simeq (E_\mathrm{c} - E_\mathrm{a})$ is fulfilled, strongly localized core level electrons with energy E_c can be excited into higher energetic, unoccupied conduction band states E_a with a photon frequency ω. At these specific energies, steep edges, the so-called absorption edges, occur in the x-ray absorption spectrum (XAS) of a material. An absorption edge is basically a step function

superimposed with a whiteline absorption peak due to the resonance, and characteristic pre- as well as near-edge features, which project details in the density of the final states. The calculated XAS of Pt around the L_3 absorption edge is shown exemplarily in Fig. 2.10. The spectrum was simulated by Dr. Markus Meinert within the FDMNES program [104].

The strongly localized character of the excited electrons leads to a high sensitivity to local features in the unoccupied states above the Fermi level in the electronic structure. The discrete binding energies allow for a large element specificity when measuring at an absorption edge of a certain material. The resonant absorption edges are denoted as K, L, and M edge depending on the initial core level 1s (K), 2s, and 2p (L), and 3s, 3p, and 3d (M) involved in the absorption process. Indices display the initial spin orbit quantum number j of the excited electron, e.g., L_2 and L_3 label the $2p_{\frac{1}{2}}$ and the $2p_{\frac{3}{2}}$ transitions, respectively.

In both resonant absorption and resonant scattering, the dipole approximation is valid and the momentum is conserved in the absorption and emission process. Consequently, when a polarized photon is absorbed or emitted, the orbital quantum number l of the electron changes by $\Delta l = \pm 1$. The different absorption edges are usually separated energetically by a couple of eV to several 1000 eV.

2.4.1 X-ray magnetic circular dichroism

XMCD is the polarization dependent absorption of circularly polarized light, depending on the magnetization orientation with respect to the helicity of the photons. It was first realized experimentally by Schütz et al. in 1987 [105]. In detail, x-ray absorption spectra (XAS) are collected either with a magnetization switching between parallel and antiparallel orientation with respect to a fixed photon helicity or vice versa. From the resulting spectra the XMCD asymmetry is determined as the difference. The imbalance of the absorption coefficient is particularly pronounced when the resonance condition is fulfilled. Therefore, in XMCD experiments the XAS are collected with circularly polarized light around the

absorption edges of a material. The XMCD yield is proportional to the magnetization M of the absorber according to the relation

$$I_{\mathrm{XMCD}} = I_+ - I_- \propto \mu^+ - \mu^- \propto \vec{P} \cdot \vec{M} = P_{\mathrm{C}} M_{\mathrm{P}} \cos(\phi) \quad , \qquad (2.21)$$

where $I_\pm$ denote the experimentally accessible intensity for parallel or antiparallel configuration of magnetic field and photon polarization, and $\mu^\pm$ are the corresponding attenuation coefficients as introduced in the Lambert-Beer law for optical absorption. The vectors $\vec{P}$ and $\vec{M}$ are the photon polarization vector and the magnetization vector, respectively. The absolute value P_{C} of the polarization vector $\vec{P}$ displays the degree of circular polarization and M_{P} is the magnitude of the magnetization in the direction of the photon helicity.

The mechanism behind the asymmetry in the XAS resulting in a finite XMCD ratio can be understood within a two step model [106]. Considering an incident circularly polarized x-ray photon with a helicity of ± 1 being absorbed by an electron from a spin orbit split core level, e.g., $2\mathrm{p}_{\frac{1}{2}}$ and $2\mathrm{p}_{\frac{3}{2}}$ states, the excitation probabilities are independent of the number of unoccupied final states, but are solely determined by the Clebsch-Gordan coefficients. Due to the momentum conservation, the photon's angular momentum must be transferred to the excited electron, yielding an orbital polarization of the excited electrons, which is identical for the $2\mathrm{p}_{\frac{1}{2}}$ and the $2\mathrm{p}_{\frac{3}{2}}$ core levels. Summation over all possible excitations weighted with their respective transmission probabilities shows that the excited electrons are spin polarized to a certain amount. This polarization is of opposite sign for the L_2 ($2\mathrm{p}_{\frac{1}{2}}$) and the L_3 transition ($2\mathrm{p}_{\frac{3}{2}}$), i.e., the two different photon helicities yield the same absolute value for the spin polarization of the excited photoelectrons, but with a reversed sign.

This generation of spin polarized electrons in the absorption process is solely based on quantum mechanical vector coupling rules and does not involve any magnetic contributions from the investigated material. The magnetic properties of the probed material become important in the second step of these considerations. The spin polarized electrons are excited into unoccupied final states above the Fermi level. In the case of an im-

balance of the spin-resolved DOS, i.e., a spin polarization at the Fermi level like in ferromagnetic materials, the transmission probability depends both on the degree of spin polarization of the excited electrons as well as the number of empty states of the respective spin species. This transmission probability is treated within Fermi's golden rule [107]. Conclusively, this results in different absorption coefficients for photons with opposite helicities regarding the magnetization orientation.

Commonly, x-ray absorption spectra are collected in two different geometries, depending on the investigated material and the focus of the study. Since the decay length of hard x-rays (above approximately 2 keV) in a solid is typically of the order of a few μm and even smaller in the soft x-ray range (below approximately 2 keV), transmission experiments are difficult to perform and require complex sample preparation. Therefore, it is more common to collect the XAS indirectly. In the total electron yield (TEY) the number of secondary electrons, in terms of photoelectrons and those created by Auger electrons from photonic excitations, is monitored and yields information on the strength of the absorption. Since only electrons close to the surface can be emitted, this technique is rather surface sensitive and mainly probes the topmost few nm. In the total fluorescence yield (TFY) the absorption is captured via the characteristic luminescence from the subsequent relaxation process. This technique allows for a much larger probing depth due to the larger decay length of the fluorescence. However, the TFY is more difficult to process in a quantitative analysis than the TEY data. The probing depth of both collection methods are sketched in Fig. 2.11

The XMCD yield can be evaluated quantitatively using the sum rule analysis introduced by Thole et al. [108] and Carra et al. [109]. The opposite signs in the spin polarization and the equal signs in the orbital polarization for electrons from different core levels $2p_{\frac{1}{2}}$ and $2p_{\frac{3}{2}}$ make it possible to separate spin and orbital contributions to the dichroic response. The sum rule analyses presented in this thesis were carried out by Dr. Markus Meinert and are thus not addressed here in more detail.

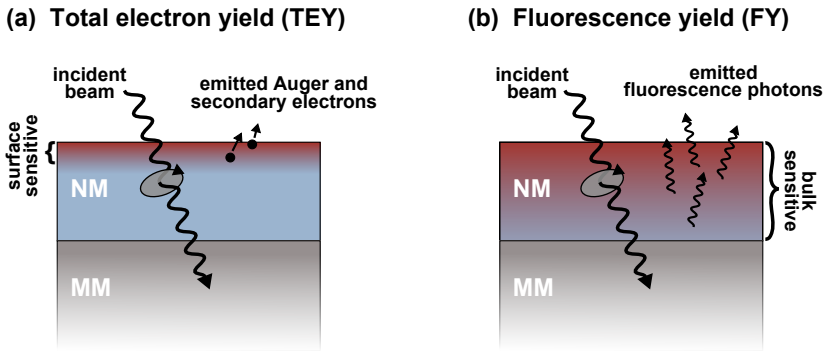

Fig. 2.11: Comparison between (a) XMCD in TEY, and (b) XMCD in FY. The XMCD in TEY is mainly surface sensitive while in FY the whole film volume is probed.

2.4.2 X-ray resonant magnetic reflectivity

For the examination of interface spin polarizations in terms of static MPEs it can be imperative to probe interfaces buried deep within the investigated sample structure. Unfortunately, the XMCD yield strongly depends on the film thickness, since either only the surface or a large fraction of the film volume is probed and contributes to the measured signal [63, 113, 115]. Therefore, a small interface-to-volume ratio may conceal contributions from the interfaces. Thus, data on the interface spin polarization from XMCD may become difficult to analyze for films thicker than a few nm. So far, most XMCD investigations on static MPEs in Pt were carried out on films with very small thicknesses, while larger thicknesses lead to a vanishing mean value of the deduced Pt moment [20, 60]. This is emphasized in Fig. 2.12. Furthermore, Ederer et al. have stated that the sum rule analysis carried out to extract the magnetic moments from XMCD spectra might result in large uncertainties and at best yields semiquantitative results for interface spin polarizations in Pt [116].

A relatively new technique to detect the element resolved magnetic properties of layer systems with a focus on their interfaces is XRMR [117, 118]. Contrary to XMCD in absorption, the magnetic circular dichroism in XRMR is observable in the interference of light reflected from the in-

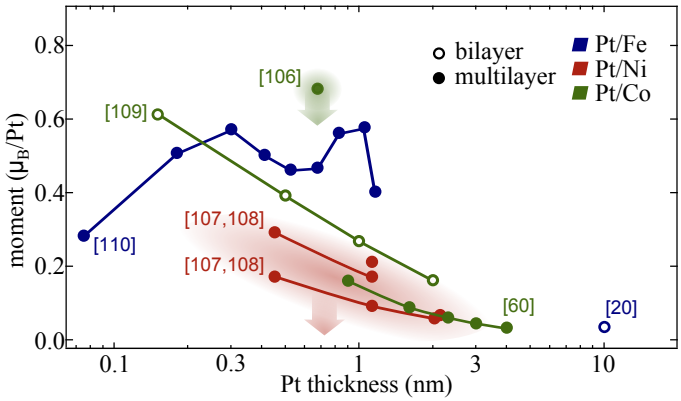

Fig. 2.12: Overview of publications investigating static MPEs in Pt/FMM bi- and multilayers by XMCD. Series from the same publication or comparable sample systems are connected by solid lines. The references are included in the graph. Note that the moments from Refs. [110–112] were measured at 10K, while the other values have been recorded at room temperature. Therefore, these results show a larger XMCD response and should be lower at RT, as indicated by the shaded areas and arrows.

terfaces. Therefore, this method is independent of the layer thickness as the main contributions to the signal originate from the surface and the interfaces.

Strictly speaking, XMCD is just a special case of the more general XRMS. While in the conventional XMCD only the absorption process is taken into account, in XRMS, or analogously XRMR in the low angle regime, the emission of a photon in a subsequent relaxation process from an equivalent virtual absorption state is observed as a scattering event. A comparison between a simplified excitation process, associated with the resonant absorption of a photon, and a resonant scattering event at the L_3 absorption edge of a ferromagnetic 3d transition metal is sketched in Fig. 2.13.

In general, off-resonant non-magnetic x-ray reflectivity (XRR) can provide information on the film thickness, roughness, and the optical properties, which are closely related to the electronic structure of layer systems. XRR is typically performed in a $\theta - 2\theta$ scattering geometry in a diffrac-

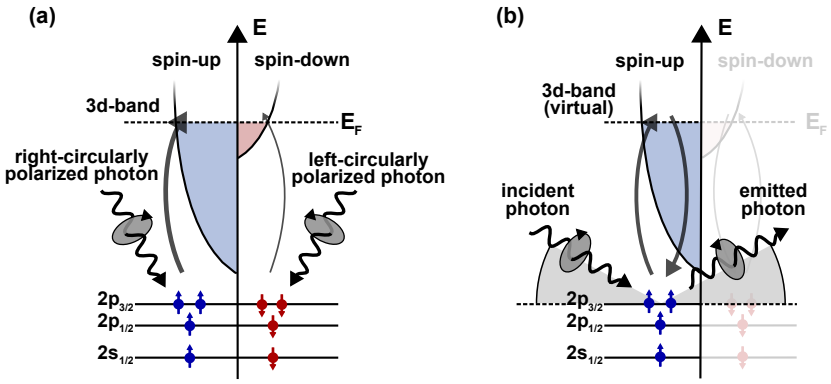

Fig. 2.13: (a) Resonant absorption process in a 3d transition metal. (b) Resonant scattering process in a 3d transition metal. For reasons of clarity, the spin-down channel is not shown in the resonant scattering. However, it does also contribute to the process.

tometer. At a small momentum transfer, the reflected light from the interfaces of a layer stack leads to interference, resulting in a characteristic oscillation pattern. The periodicity of these so-called Kiessig fringes critically depends on the film thickness and thus yields information on this property.

For grazing incidence in the specular regime, the XRR mechanism can be treated within an optical theory, i.e., the crystal structure can mostly be neglected, as the scattering vector $q = 2k \sin\theta$, with the wavenumber k of the incident beam and the angle θ between the incident beam and the film plane, is small compared to the reciprocal lattice vector. This assumption is even valid for the hard x-ray regime in the studies presented in this thesis, which enables the description in a continuum approach [119]. The

transmission and reflection of electromagnetic radiation at an interface can be calculated within the Fresnel equations

$$\begin{aligned} t_\mathrm{s} &= \frac{2n_1 \cos\alpha}{n_1 \cos\alpha + n_2 \cos\beta} \\ r_\mathrm{s} &= \frac{n_1 \cos\alpha - n_2 \cos\beta}{n_1 \cos\alpha + n_2 \cos\beta} \\ t_\mathrm{p} &= \frac{2n_1 \cos\alpha}{n_2 \cos\alpha + n_1 \cos\beta} \\ r_\mathrm{p} &= \frac{n_1 \cos\beta - n_2 \cos\alpha}{n_2 \cos\alpha + n_1 \cos\beta} \quad . \end{aligned} \tag{2.22}$$

Here, t_p (r_p) and t_s (r_s) are the transmission (reflection) coefficients for polarized light with the electric field vector parallel (p) and perpendicular (s) to the scattering plane, respectively. The prefactors n_1 and n_2 are the complex refractive indices of the two media, which, in general, describe the propagation of electromagnetic radiation in an optical medium. The index of refraction can be written as

$$n = 1 - \frac{r_\mathrm{e}}{2\pi}\lambda^2 \sum n_\mathrm{j} f_\mathrm{j}(E) \quad , \tag{2.23}$$

where r_e is the electron radius, λ is the wavelength of the light, n_j is the number of atoms of species j per unit cell and f_j is the corresponding complex scattering amplitude depending on the photon energy. The scattering amplitude is given by

$$f(E) = f_0 + f'(E) + \mathrm{i}f''(E) \tag{2.24}$$

where f_0 is the Thomson scattering amplitude for the off-resonant regime and the dispersive and absorptive scattering factors f' and f'', respectively, are relevant mainly in the vicinity of an absorption edge, i.e., in the resonant regime. These anomalous contributions are connected via the Kramers-Kronig relation

$$f'(E) = \frac{2E_0}{\pi} \oint \frac{f''(E)}{E_0^2 - E^2} \mathrm{d}E \quad . \tag{2.25}$$

In another formulation the index of refraction can be expressed as

$$n = 1 - \delta(E) + \mathrm{i}\beta(E) \tag{2.26}$$

Here the phaseshift and the attenuation of the incident light due to absorption in a material are treated in terms of the dispersive correction δ and the absorptive correction β, respectively. The parameter δ is essentially the real part of the correction in n and can be written as

$$\delta(E) = \frac{r_\mathrm{e}}{2\pi}\lambda^2(f_0 + f'(E)) \tag{2.27}$$

and the absorptive correction β is given by the imaginary part

$$\beta(E) = \frac{r_\mathrm{e}}{2\pi}\lambda^2 f''(E) \quad . \tag{2.28}$$

The parameter β is proportional to the absorption coefficient μ of a material and can be monitored directly by collecting an absorption spectrum. Both δ and β critically depend on the wavelength, i.e., the photon energy, and the optical properties of the medium. For photon energies in the x-ray range, the refractive index n of solid materials is generally smaller than unity ($n < 1$), i.e., they are optically less dense than vacuum ($n_0 = 1$). This leads to total reflection up to a critical angle θ_c, when x-rays propagate from vacuum into an optical medium. The direct correlation between the critical angle and the refractive index can yield information on the optical properties.

For heterostructures consisting of several layers, the transmission and reflection for s- and p-polarized electromagnetic waves at each interface can be calculated quantitatively on the basis of the Fresnel equations [120]. Since the beam is reflected at every interface it approaches, the wave field of the beam is treated within a multiple scattering analysis. This is achieved by using a recursive formula

$$R_\mathrm{i} = \frac{r_\mathrm{i} + R_{\mathrm{i}+1}\exp(2\mathrm{i}k_{\mathrm{i}+1}d_{\mathrm{i}+1})}{1 + r_\mathrm{i}R_{\mathrm{i}+1}\exp(2\mathrm{i}k_{\mathrm{i}+1}d_{\mathrm{i}+1})} \quad , \tag{2.29}$$

introduced by Parratt in 1954 [118, 121]. Here, r_i is the reflectivity of the electric field of one light beam at an interface, as derived from the Fresnel equations (Eq. (2.22)), and $R_\mathrm{i} = \frac{E_\mathrm{i}^\mathrm{R}}{E_\mathrm{i}^\mathrm{T}}$ is the ratio of the amplitudes of the partial waves in each film and defines the reflectivity of the total electric field in one layer. d_i is the thickness of the ith layer, while k_i displays the normal component of the wavevector in it.

However, in real systems with a finite roughness, the interfaces are not sharp edges between two materials, but in fact represent a non-abrupt transition between two media. The surface imperfection results in an increase of diffuse scattering and a reduction of the reflection of a beam at the interfaces. For the evaluation of XRR data this gradual transition can be treated as an interface profile function $p(z)$ and the reduction of the reflectivity can be approximated by multiplication of the Fresnel coefficients with the fourier transform of its derivative $\frac{\mathrm{d}p(z)}{\mathrm{d}z}$ [122]. A common approach to modeling the roughness of a layer stack is given within a Névot-Croce approximation [123], which allows an analytical description of the roughness under the assumption that the derivative of the optical profile across the interface is Gaussian shaped. Therefore, the evaluation of the reflectivity data provides information not only on the thicknesses, but also on the interface roughnesses of a layer stack. However, with specular XRR it is in general not possible to distinguish between different types of roughness on an atomic scale, since the reflectivity only projects the average over a large lateral area. Thus, the approach by Névot and Croce does not correspond to a specific kind of roughness, e.g., interface waviness or interdiffusion, etc., but is only based on the averaged electron density distribution parallel to the plane normal [124].

In the case of resonant magnetic scattering, i.e., in the vicinity of a circular dichroic active absorption edge it is necessary to introduce an additional magnetic scattering factor to the conventional scattering amplitude. Thus, the formula in Eq. (2.24) expands to

$$\begin{aligned} f(E) = \quad & -r_0 \left[(\vec{e}_\mathrm{f}^{\,*} \cdot \vec{e}_\mathrm{i}) \cdot \left(f_0 + f'(E) + \mathrm{i} f''(E) \right) \right. \\ & \left. + \mathrm{i} \, (\vec{e}_\mathrm{f}^{\,*} \times \vec{e}_\mathrm{i}) \cdot \vec{b} \cdot \left(m'(E) + \mathrm{i} m''(E) \right) \right] \end{aligned} \tag{2.30}$$

in first order [125]. $\vec{e}_{\mathrm{i}}$ and $\vec{e}_{\mathrm{f}}$ are the complex polarization vectors of the incident and the scattered x-rays, respectively, while $\vec{b}$ is the unit vector of the film magnetization. The terms m' and m'' are the magnetic contributions to the dispersive and the absorptive correction, respectively, and vary depending on the configuration of photon helicity and film magnetization. m' and m'' are also connected via the Kramers-Kronig relation (see Eq. (2.25)), analogously to the non-magnetic scattering factors f' and f''. In a small angle approximation the resonant magnetic scattering amplitude from Eq. (2.30) can be simplified to

$$\begin{aligned} f(E) = \quad & -r_0 \left[(f_0 + f'(E) + \mathrm{i}f''(E)) \right. \\ & \left. + P_{\mathrm{C}} \left(m'(E) + \mathrm{i}m''(E) \right) \right] \quad , \end{aligned} \tag{2.31}$$

where P_{C} is the degree of circular polarization of the polarized light. For hard x-rays the typical scattering angle range is below 4°, thus, the approximation can be used in this study.

Similarly to the optical parameters δ and β in Eqs. (2.27) and (2.28) the magnetooptical parameters $\Delta\delta$ and $\Delta\beta$, i.e., the magnetization dependent changes in the optical parameters, are defined as

$$\Delta\delta(E, M) = \frac{r_{\mathrm{e}}}{2\pi}\lambda^2 \cdot m'(E, M) \tag{2.32}$$

and

$$\Delta\beta(E, M) = \frac{r_{\mathrm{e}}}{2\pi}\lambda^2 \cdot m''(E, M) \quad . \tag{2.33}$$

The change in the optical parameters with the magnetization orientation regarding the photon helicity manifests itself in a change of the reflectivities $I_{\pm}$, i.e., at a fixed photon helicity the reflectivity varies for positive and negative magnetization and vice versa. Therefore, the asymmetry ratio

$$\Delta I = \frac{I_+ - I_-}{I_+ + I_-} \tag{2.34}$$

is a suitable measure in order to investigate interface magnetization. It is reasonable to consider the weighted reflectivities, i.e., the asymmetry ratio instead of the difference, since the XRR intensity varies over several orders

of magnitude. By modeling the magnetooptical profile and fitting the resulting simulation to the experimental data, the spatial distribution of $\Delta\delta$ and $\Delta\beta$ can be derived. Auxiliary XMCD measurements or theoretical calculations can be used to determine the magnetic moments per atom in the magnetized volume.

XRR/XRMR data processing

The evaluation of the XRR data and the XRMR asymmetry ratios is performed with the analysis tool ReMagX [126] developed by Sebastian Macke. The fitting algorithm for the non-magnetic reflectivity data I is based on the recursive Parratt algorithm [121] (see Eq. (2.29)). The roughnesses are modeled within a Névot-Croce approximation [123].

For the asymmetry ratio the fitting routine is based on the Zak matrix formalism [127]. Here, the roughness is also considered in the optical profile as a Gaussian distribution centered at the interface [128]. The fitting procedure is assessed using the χ^2 method. The "goodness of fit" χ^2 represents the weighted sum of the squared errors, i.e., the deviations between the experimental data and the expected values in terms of a simulated curve. χ^2 is minimized within the fitting procedure in order to gain the best agreement between experiment and simulation. The minimization procedure is based on the Simplex algorithm.

The relevant fitting parameters in the evaluation of the x-ray reflectivities are the thickness, the roughness and the optical parameters δ and β of each single layer. For the assessment of the magnetic moments from simulations of the XRMR asymmetries, additional magnetooptical parameters $\Delta\delta$ and $\Delta\beta$ with a certain spatial distribution have to be included into the fitting procedure. Prior to the simulations, the XRR curves have to be formatted to comply with the requirements of the fitting tool ReMagX. Therefore, the scattering angle θ has to be converted into the scattering vector q. Next, the data have to be normalized and a footprint correction has to be performed. The footprint is an artifact, present in the data at grazing incidence due to the limited size of the sample and the finite expansion of the beam [129].

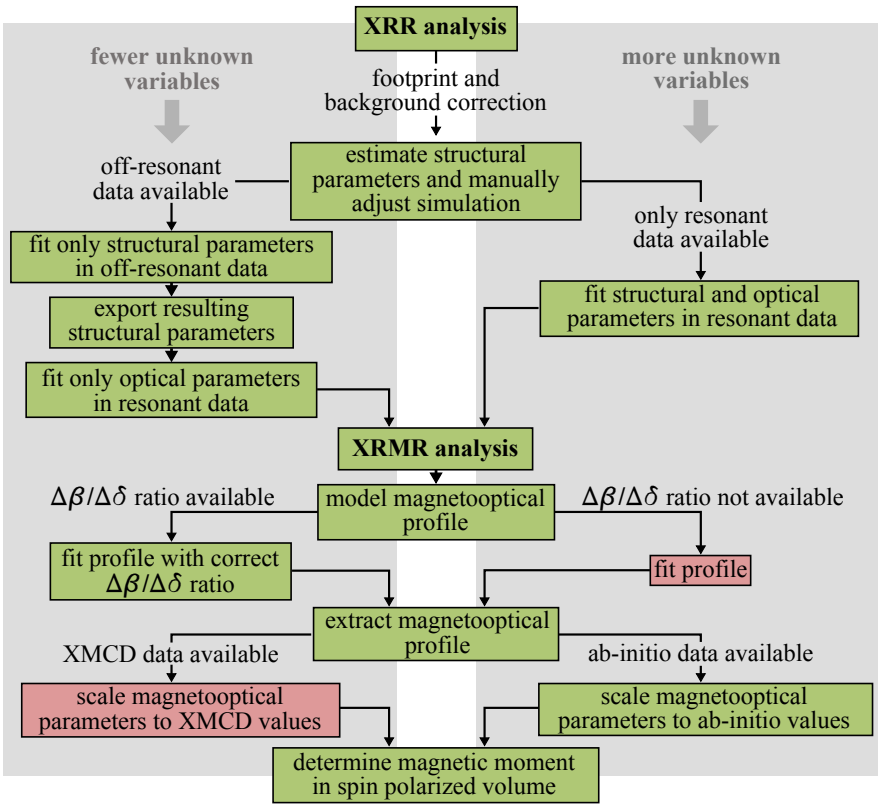

Fig. 2.14: Recipe procedure for the determination of induced magnetic moments by evaluation of XRR and XRMR data. The green blocks correspond to the general procedure used in this work, while the red boxes indicate alternative approaches.

In the next step of the experimental data processing the non-magnetic XRR curves have to be evaluated to gain information on the structural properties of the films, i.e., film thickness and roughness. Therefore, the fitting procedure starts with an educated guess of the structural and optical properties of the sample system. An estimate of the film thickness and roughness can usually be drawn based on information on the preparation process. Otherwise the thickness t can be estimated from the width of the Kiessig fringes Δq in the XRR curves via $t = \frac{2\pi}{\Delta q}$. With an approximation

of the mass density a starting point for the optical parameters δ and β can be derived from the Henke tables [130]. The tabulated values are only reliable far from the resonant absorption edges. Therefore, it is reasonable to evaluate off-resonant XRR, if available, in order to eliminate any influences from absorption edges. Starting from these values, the XRR data are simulated within the software. The curves are adjusted manually first, to get a rough agreement between the simulation and the experimental data, and subsequently fitted based on the recursive Parratt algorithm. Using the structural parameters gained in the fitting of the off-resonant XRR then allows to evaluate the optical parameters at the resonance by fitting the resonant XRR. Knowledge of the chemical composition of the constituent materials in the heterostructure helps to assess the resulting fitting parameters, in particular the optical constants, for their reliability and to adjust the model if necessary. If the fit converges with satisfactory results, the structural information gained can be used as an input for the subsequent XRMR analysis.

The fitting tool allows to model and vary magnetooptical profiles, i.e., the spatial distribution of $\Delta\delta$ and $\Delta\beta$, while keeping the structural parameters and the optical parameters δ and β constant. An appropriate model for the magnetooptical profile at the interface has to be estimated and a simulation based on the distribution of $\Delta\delta$ and $\Delta\beta$ can be fitted to the experimental asymmetry ratio. If the XRMR fit converges with a satisfactory result, the magnetooptical parameters can be scaled to optical data from *ab initio* calculations for a quantitative approximation of the magnetic moments per atom in the spin polarized volume. Additionally, absorption data from XMCD measurements can be utilized to scale the magnetooptical parameters and evaluate the magnetic moments, if available. In this study, different models for the magnetooptical profiles were tested in order to find the optimum fitting procedure for the XRMR analysis. The different approaches are discussed in detail in section 4.2.1. A recipe procedure for the XRR/XRMR data analysis is sketched in Fig. 2.14.

3 Fabrication and Investigation of $NiFe_2O_4$ thin films

In this chapter the fabrication and characterization of $NiFe_2O_4$ thin films with two different techniques will be discussed. In the first part, a short introduction to the preparation of NFO thin films using direct-liquid-injection chemical vapor deposition (DLI-CVD) will be given. Exemplary measurements of the film properties will be shown and the attributes of this deposition technique will be discussed. These results were gained in close collaboration with the group of Prof. Arunava Gupta during a research stay at the University of Alabama and only provide a rough overview of the studies on CVD NFO.
The second part will address results from sputter-deposited films. The film properties are investigated in detail and the optimum process parameters are evaluated. These experiments were published in Ref. [131] and the corresponding sections are based on this publication.

3.1 Chemical vapor deposition of $NiFe_2O_4$ thin films

DLI-CVD was utilized for the fabrication of NFO thin films. The employed setup belongs to the laboratory of Prof. Dr. Arunava Gupta and is located at the University of Alabama in Tuscaloosa, AL (USA). In the DLI-CVD process a liquid solution is evaporated at a certain temperature, depending on the constituents, and injected into a tubular process chamber along with a steady flow of oxygen through the system. Different temperature zones in the process tube allow for regulating the chemical reaction of

the solvents with the oxygen atmosphere. By positioning the substrate at the appropriate temperature region in the tube the growth conditions and thus the film properties can be controlled. Compared to many physical vapor deposition techniques like pulsed laser deposition (PLD) or sputter deposition the growth rate in DLI-CVD is much larger and promotes the growth of thick films up to the μm regime.

3.1.1 Experimental details

Preliminary work on the fabrication of NFO, using the DLI-CVD setup utilized in this study, was carried out by Li et al. and published in Ref. [132]. They determined the ideal process parameters for the DLI-CVD, including precursor solution injection rate, carrier gas flow rate, vaporizer temperature, inlet and outlet pressure, and substrate temperature. The values found constitute the basis for the experiments in this study.

Anhydrous $Ni(acac)_2$ and $Fe(acac)_3$ (acac=acetylacetonate) is used as metal organic precursors and dissolved in N,N-dimethylformamide (DMF) in a molar ratio of 1 : 2, according to the composition of NFO. The solution is evaporated by heated Ar gas at a temperature of 175°C in a Brooks Instruments DLI vaporizer system and injected into the quartz tube reaction chamber along with a steady flow of preheated oxygen. This approach minimizes the thermal decomposition of the precursors compared to evaporization from a hot metallic surface.

Li et al. deposited NFO films with thicknesses $\geq 1\,\mu$m at different substrate temperatures ranging from 500°C to 800°C. They checked their samples for their structural and magnetic properties in order to find the ideal deposition temperature. The optimum deposition temperature region, i.e., the area exhibiting the strongest reaction, was found at a temperature of about 550°C. Thus, in the present experiment the substrate was positioned at the corresponding site in the tube reactor. All films were deposited on (001) oriented, isomorphous $MgAl_2O_4$ (MAO) substrates with a lattice mismatch of about 3% in order to allow for an epitaxial growth. Li et al. also tested (001) oriented MgO substrates, which exhibit an even smaller lattice mismatch with NFO of only 1%, considering the double

lattice constant $2a_{\mathrm{MgO}} = 8.42\,\text{Å}$ of MgO. Nevertheless, they observed that the epitaxial NFO developed macroscopic cracks on MgO after deposition and cooling down, which they ascribed to high residual tensile stress. Therefore, the investigations discussed here concentrate on films deposited on MAO. The deposition rate was between 1.5 Å/s and 2 Å/s. Therefore, the film thicknesses are significantly larger than for the films prepared by sputter deposition.

3.1.2 Results and discussion

The structural properties of the NFO films were checked using scanning electron microscopy (SEM) and x-ray diffraction (XRD). SEM images of the films' cross sections were taken in a JEOL-7000 FEG SEM to get a rough estimate of the film thicknesses and the homogeneity of the films. The films produced are in the range of about 900 nm to 1.2 μm. In the SEM images it is visible, that some films show very large roughnesses, while others are rather smooth. The SEM cross section images of two NFO films are shown exemplarily in Fig. 3.1. Both films were deposited with the same deposition parameters. Yet, while the film in (a) shows a good homogeneity and a smooth surface within the sensitivity of the SEM image, the film in panel (b) exhibits a very large roughness and is not well suited for device preparation.

The SEM was also equipped with an energy dispersive x-ray spectroscopy detector (EDX) which was used to probe the chemical composition of the NFO samples.

The biggest obstacle during the production of NFO thin films in the DLI-CVD system was the reproducibility of samples. The EDX analyses of the films showed that the stoichiometry is subject to strong variations between the sundry depositions. The Fe:Ni ratio varies from 1.8 to 2.9, often far off from the desired ratio of 2. Where this large variation comes from is open to speculation. A possible reason for this is the unstable heating of the tubes transporting the vaporized solution and the oxygen to the reaction chamber. Both precursors show a high volatility but a low thermal stability above 200°C. Thus, it is imperative to control the tem-

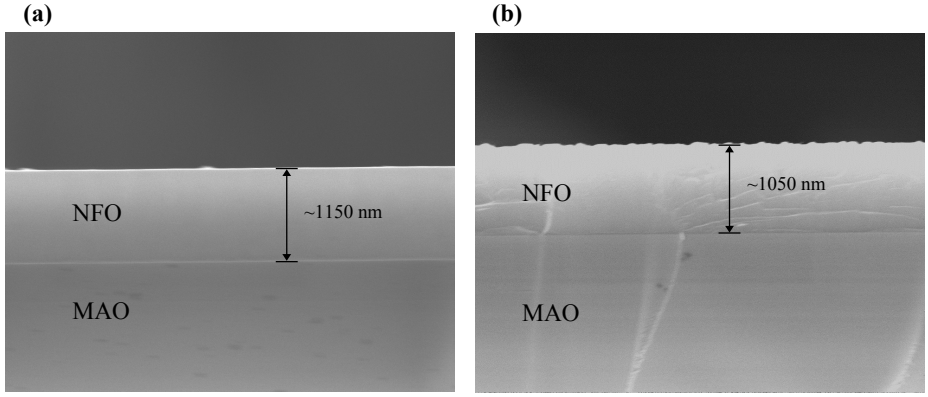

Fig. 3.1: SEM cross section images of two different NFO films.

perature of the evaporated solution very carefully, since too high or too low temperatures can cause the solution to decompose and the metallic constituents to precipitate. These error sources hamper the exact calibration of the composition and impair the electrical properties of the films.

Yet, it has to be noted that the EDX method itself introduces errors to the correct determination of the stoichiometry in thin films, as it can exhibit a probing depth of a couple of μm, which is larger than the film thicknesses. Hence, it also probes the subjacent substrate. It has been found that substrates of MAO and MgO can incorporate small contaminations of different elements, including Fe and Ni, which obscure the EDX and interfere with the results. This is reflected in the fact that the EDX results exhibit strong variations of up to 10% on the same sample. However, this does not solely account for the large discrepancies found in the compositions. The oxygen content could not be monitored with the EDX detector used, since the characteristic radiation from the light oxygen is below the detection limit.

In order to study the crystallographic properties of the films with strongly varying stoichiometries, XRD measurements were carried out in a Philips X'Pert Pro diffractometer with a Cu K_α source ($\lambda = 1.541874\,\text{Å}$) and a Bragg Brentano configuration. Diffraction patterns for a set of NFO sam-

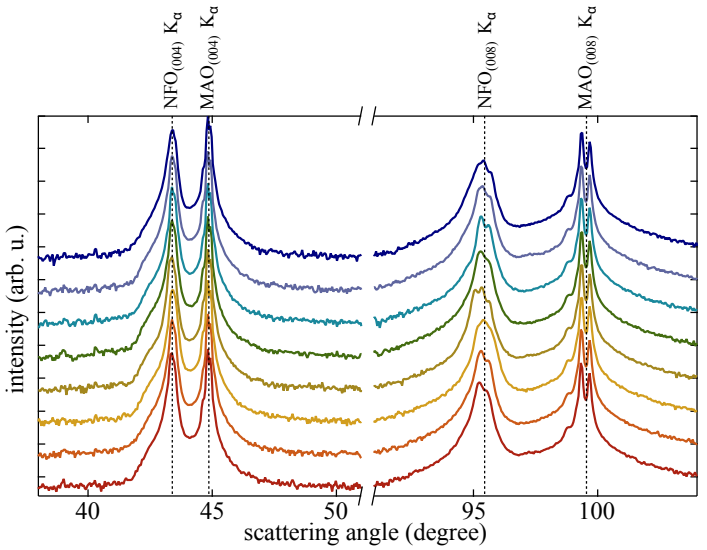

Fig. 3.2: XRD scans of 8 different NFO films prepared by CVD under identical process conditions. All films show the same features in the XRD patterns, corresponding to (004) and (008) peaks of bulk NFO (dashed lines).

ples deposited with identical process parameters are displayed in Fig. 3.2.

All the films investigated show an epitaxial growth in the (001) direction with pronounced (004) and (008) diffraction peaks, indicating a good crystallinity. The peak positions are consistent with the NFO bulk lattice constant of $a_{\mathrm{NFO}} = 8.34\,\text{Å}$. Hence, despite the mismatch to the MAO substrate no lattice strain is present. This reveals a complete lattice relaxation, which can be attributed to the large thickness of the films. The variations in composition are not visible in the peak positions, indicating that they do not modify the lattice structure considerably. This promotes the assumption that the films grow in the correct inverse spinel structure, while excess Fe (Ni) atoms either enter unoccupied lattice sites or replace Ni (Fe) ions on octahedral lattice sites.

The magnetic properties were investigated by means of alternating gradient field magnetometry (AGM) in a Princeton MicroMag with mag-

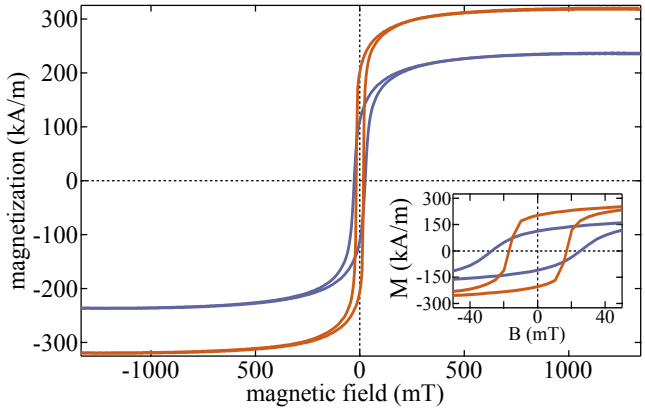

Fig. 3.3: Exemplary magnetometry curves (AGM) for two different NFO samples prepared under identical process conditions.

netic fields of up to 1.3 T. The magnetization curves for two exemplary samples are presented in Fig. 3.3. Both samples were deposited under the same process conditions; however, they show significantly different magnetizations. In particular, the saturation magnetizations of 235 kA/m (1.83 μ_B/f.u.) for sample 1 and 317 kA/m (2.48 μ_B/f.u.) for sample 2 deviate strongly. The coercivities (see inset Fig. 3.3) also show some large differences between $H_c \approx 26$ mT in sample 1 and $H_c \approx 17$ mT in sample 2. It has to be noted that the rough estimation of the film thicknesses from the SEM images of the sample cross sections adds an additional uncertainty to the calculation of the magnetization. Yet, these uncertainties do not account for the large variations between the samples completely. Instead they may be attributed to the divergence in stoichiometry. An enhanced magnetization could indicate an increased Fe:Ni ratio, thus, excess Fe residing on unoccupied lattice sites or replacing Ni cations on octahedral sites. This is in agreement with the EDX results, which yield a large Fe:Ni ratio of about 2.6 for sample 2, while sample 1 exhibts a slightly smaller ratio of about 2.4. However, even sample 1 incorporates a significant amount of excess Fe, while the magnetic moment is still below the literature bulk value of 2 μ_B/f.u.. This reduction in magnetic moment

might be an indication for antiferromagnetic pinning in antiphase boundaries, leading to incomplete saturation at the available fields of 1.3 T. The formation of these defects strongly depends on the growth conditions during deposition [31, 133–135]. Therefore, the large discrepancies in the magnetization data corroborate the former assumption of an unstable deposition process and a less than ideal reproducibility of the CVD process. Hence, a careful investigation of the chemical vapor deposited NFO samples is imperative before using them for spintronic and spin caloritronic experiments.

Another obstacle of the DLI-CVD in the setup presented is the vaccuum break between the fabrication of NFO and the subsequent deposition of additional layers, e.g., Pt, for spintronic and spin caloritronic devices. These drawbacks prompted the search for an alternative technique for the deposition of NFO thin films, applicable at the author's institution in Bielefeld. Thus, reactive sputter deposition was utilized to synthesize NFO, which is known to show a high reproducibility and allows to combine the fabrication of NFO films with the subsequent deposition of additional layers for spintronic and spin caloritronic applications. The results of this approach are described in the next section.

3.2 Sputter deposition of $NiFe_2O_4$ thin films

In addition to the DLI-CVD, as discussed in section 3.1, reactive dc magnetron co-sputter deposition was utilized to fabricate NFO thin films. The process of sputter deposition differs fundamentally from CVD. In principle, during a sputter deposition a solid target is bombarded with high energetic Ar^+ ions from an Ar plasma. The impacts lead to an ejection of atoms and atomic clusters from the target, traveling towards a substrate and consequently condensing at the surface. The base pressure in a sputter deposition system is in the ultra high vacuum range (uhv) to minimize contamination and impurification of the synthesized films, while the process pressure is typically of the order of 10^{-3} mbar, to allow for a stable plasma. In a conventional sputtering process Ar is injected into

the chamber as a process gas, as it is inert and does not react with the other constituents. In a reactive sputtering process, however, an additional reactive gas, e.g., O_2 or N_2, can be added or replace the inert gas completely in order to induce a reaction between the process gas and the sputter materials. This way it is possible to synthesize elaborate oxidic or nitric compounds.

3.2.1 Experimental and theoretical details

In this study, epitaxial NFO thin films were grown by means of ultra high vacuum reactive dc magnetron co-sputtering in a pure oxygen atmosphere at various substrate temperatures (400°C to 800°C). The substrate temperature can significantly affect the growth conditions and, thus, the film properties. Therefore, variation of deposition temperature makes it possible to tune the material properties and to optimize the sample. The base pressure in the exploited sputtering chamber was lower than 10^{-8} mbar. The O_2 pressure during sputtering was 2.2×10^{-3} mbar. The target-to-substrate distance was 21 cm at a target diameter of about 7.6 cm. The confocally arranged sources were tilted towards the substrate at an angle of 30° to the plane normal. The films were co-sputtered from elemental Ni and Fe targets. Analogously to the previous experiments, the films were deposited on (001) oriented, isomorphous MAO substrates with a lattice mismatch of about 3% to allow for epitaxial growth. The deposition rate was 0.14 Å/s, which is at least one order of magnitude smaller compared to the CVD deposition. The film thicknesses are 28 nm for the temperature series and 58 nm for samples deposited in a subsequent series at 680°C.

XRR was used to calibrate the film thickness. X-ray fluorescence (XRF) served to quantify the Ni:Fe ratio. Again the crystallographic properties of the films were checked using XRD in a Bragg Brentano configuration. XRR, XRF, and XRD were performed in the Philips X'Pert Pro diffractometer with a Cu K_α source, analogously to the previous experiment.

X-ray photoelectron spectroscopy (XPS) gave additional information about the cation valencies. The XPS measurements were performed using a PHI5600ci multitechnique spectrometer equipped with a monochromatic

Al K_α source (1486.7 eV) with 0.3 eV full width at half-maximum. The setup is located at the University of Osnabrück and the measurements were performed by Dr. Karsten Kuepper. The overall resolution of the spectrometer is 1.5% of the pass energy of the analyzer, 0.45 eV in the present case. Complementary Fe 2p spectra were also recorded with an Mg K_α standard non monochromatic x-ray source (1253.6 eV). The measurements were recorded with the sample at RT. The thin NFO films were rinsed with Isopropanol just before mounting them into the loadlock of the experimental chamber. No other preparation of the sample surface, e.g., by Ar ion sputtering, was performed, in particular to avoid a reduction of the Fe and Ni ions. The spectra were calibrated with a corresponding measurement of the Au $4f_{7/2}$ level (84.0 eV) of a gold foil.

Again, the magnetic properties were checked with AGM. Atomic force microscopy (AFM) studies of the surface topography were done with a Bruker AFM Multimode instrument using Bruker FMV-A probes in tapping mode. Optical spectroscopy in the range of 0.8 to 5.5 eV was performed in a Perkin Elmer Lambda 950 Spectrometer. Reflection and transmission spectra were recorded to obtain the absorption coefficient and derive the optical bandgap. The transport properties were investigated by temperature dependent dc conductivity measurements in a cryostat with a two-point probe technique.

Element specific XAS, XMCD, and magnetic linear dichroism (XMLD) measurements were taken at RT at beamline 4.0.2 of the Advanced Light Source, Berkeley. The substrate luminescence was detected with a photodiode to measure the absorption signal of the films in addition to the sample drain current (total electron yield). The magnetic field of 500 mT was switched for every energy, either in the film plane (XMLD) or parallel to the beam with the sample surface including an angle of 30° with the beam. The XMLD spectra were taken along the [100] direction of the NFO film. The resolving power of the beamline was set to $E/\Delta E \approx 6000$. The degree of circular polarization was 90%.

The absorption spectra were calculated within atomic multiplet and crystal field theory with the CTM4XAS program. [136] The crystal field

parameter for the octahedral Ni^{2+} was set to $10Dq = 1.1\,\text{eV}$ and the Slater integrals were reduced to 75% and 90% of their atomic values for the d-d and p-d interactions, respectively, to account for screening. For the octahedral (tetrahedral) Fe^{3+} we chose $10Dq = 1.6\,\text{eV}$ ($10Dq = -0.8\,\text{eV}$). In this case the Slater integrals were reduced to 75% and 85%. An exchange field of $g\mu_B B = 10\,\text{meV}$ was applied to break the spin symmetry. For Ni, a Lorentzian broadening of 0.15 eV (0.3 eV) was applied to the L_3 (L_2) edges to account for lifetime effects. For Fe, the Lorentzian broadening was set to 0.2 eV (0.4 eV). An additional Gaussian broadening of 0.15 eV was applied to account for the finite resolving power of the instrumentation. Additionally, the calculated spectrum of the octahedral Fe^{3+} was shifted by 0.23 eV to higher energy. Both species were weighted 1:1. These parameters were chosen to obtain a best fit to the experimental data and are close to the parameters suggested in earlier publications [137, 138]. The XMCD and XMLD evaluations presented here were performed by Dr. Markus Meinert.

3.2.2 Results and discussion

Variation of deposition temperature

Stoichiometry and crystal structure

By adjusting the sputter parameters according to the XRF observations, Ni:Fe ratios between 1.02:1.98 and 0.97:2.03 were obtained for the films, close to the correct composition. In Fig. 3.4 (a) the results of XRD measurements are presented. In the XRD patterns (004) Bragg peaks are visible for all samples, i.e., all the films show a crystalline structure with epitaxial growth in the [001] direction. The peaks get more pronounced with increasing deposition temperature. Weak Laue oscillations were observed at the (004) peak in the 600°C curve, indicating the smoothest interfaces for this deposition temperature.

A significant out-of-plane strain is visible in all samples. The deviations of the vertical lattice parameter with respect to the bulk lattice constant ($a_{bulk} = 8.34\,\text{Å}$) can be derived from the peak positions in the

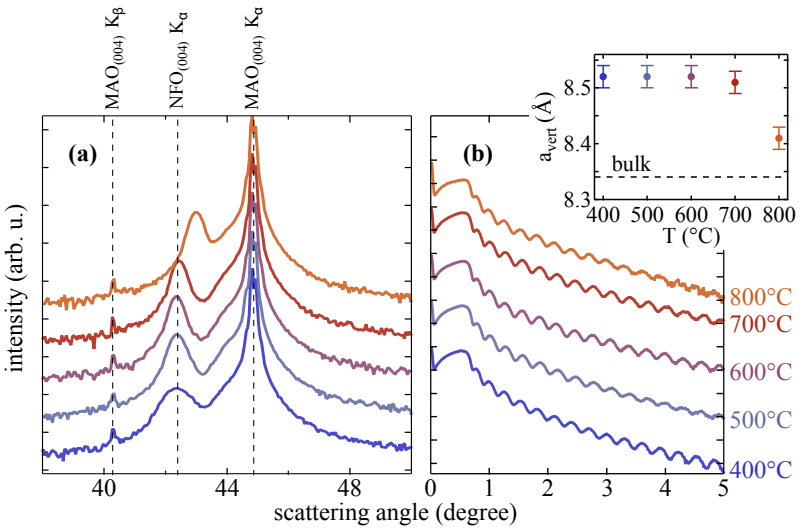

Fig. 3.4: (a) XRD and (b) XRR patterns of NFO films for different deposition temperatures. Inset: vertical lattice parameter a_{vert} plotted against deposition temperature.

XRD scans (see inset in Fig. 3.4). The films deposited at 400°C, 500°C, and 600°C show the same vertical lattice parameter $a_{vert} = 8.53$ Å, which is in good agreement with the values found by Foerster et al. in pulsed laser deposited thin films on MAO, but is significantly larger than the bulk value [139]. The increase of the vertical lattice parameter with respect to the bulk value implies that the films are tetragonally distorted, i.e., expanded in the direction perpendicular to the surface and compressed in the film plane, due to a comparatively large mismatch with the MAO (001) substrate ($a_{MAO} = 8.08$ Å). However, with increasing deposition temperature the lattice parameter decreases leading to $a_{vert} = 8.51$ Å and $a_{vert} = 8.41$ Å for the films sputtered at 700°C and 800°C, respectively. This is visible in the shifted (004) diffraction peaks in the XRD patterns. This trend in lattice distortion can be explained by an increased strain relaxation at higher thermal energies.

The well pronounced Kiessig fringes in the XRR curves shown in Fig. 3.4(b) indicate smooth surfaces for all sputtered films with roughnesses in

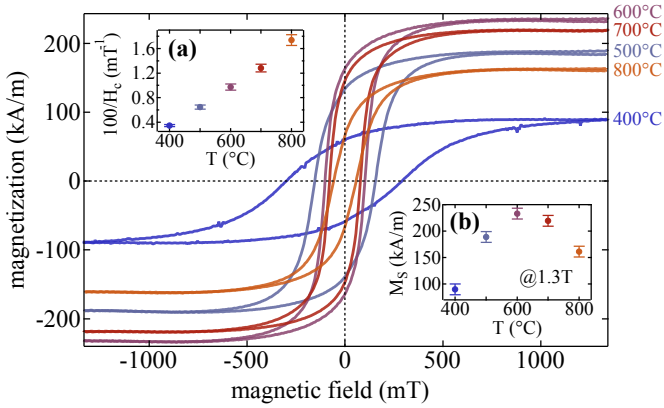

Fig. 3.5: Magnetization curves (AGM) of NFO for different deposition temperatures. Inset (a): The reciprocal coercivity H_C^{-1} over deposition temperature. Inset (b): Saturation magnetization at 1.3 T over deposition temperature.

the range of 0.3 nm to 0.4 nm. The films deposited at 600°C and 700°C show the smallest values while the 800°C sample shows the highest roughness.

Magnetic properties

Fig. 3.5 displays the magnetization after subtraction of a linear background. The coercivity and saturation field are significantly larger than the values observed for the chemical vapor deposited films, which might be attributed to the much smaller thicknesses and the larger strain of the sputtered films. The coercivity is found to decrease with increasing temperature (see inset (a) of Fig. 3.5). Since a lower coercivity can be generated by fewer pinning centers and, therefore, fewer defects in the material, this reciprocal dependence between coercivity and deposition temperature confirms a lower defect density for higher deposition temperatures [140].

The saturation magnetization shows a different behavior. It increases from 400°C to 600°C, but decreases slightly for 700°C and drastically for 800°C deposition temperature. This trend in the temperature dependence is depicted in inset (b) of Fig. 3.5. The highest saturation magnetization

of about 236 kA/m (1.84 μ_B/f.u.) is observed for deposition at 600°C, but is still lower than the literature values [34–36]. A lower magnetization in thin films with respect to bulk has been observed in NFO before [34], as well as in other inverse spinel ferrites like magnetite (Fe_3O_4) [141]. Again, the reduced magnetization at 1.3 T may arise from antiferromagnetic pinning in antiphase boundaries, the density of which critically depends on the preparation conditions [31,133–135]. Another mechanism of reduction of the magnetization may be the formation of disordered regions between crystallites [34]. The large coercive field of the films (around 100 mT) is in agreement with a relatively high defect density. In both cases, full saturation is obtained at much higher fields, so the background subtraction in measurements with only a few Tesla may contain substantial uncertainties.

Sample deposition at 680°C

Structural and magnetic properties

Based on the former results, additional samples were produced at a substrate temperature of 680°C with a thickness of about 58 nm and more detailed studies were carried out. The samples again crystallized well with a (001) orientation and show smooth surfaces in the XRR diffraction patterns (not shown). The vertical lattice parameter $a_{vert} = 8.48$ Å is less expanded than in the corresponding films from the temperature series, due to an increased lattice relaxation with increasing thickness. An in-plane lattice parameter $a_{ip} = 8.19$ Å was derived from an analysis of the (066) peak. As expected, the values reveal a pronounced tetragonal distortion for growth on MAO (001) substrates with $a_{vert}/a_{ip} = 1.035$. The unit cell volume is reduced by about 2% with respect to bulk material. The additional samples had a slightly lower magnetization (around 200 kA/m, i.e., 1.53 μ_B/f.u. considering the reduced unit cell volume) than the films prepared earlier for the deposition temperature series. No out-of-plane anisotropy was observed, in line with the theoretical prediction by Fritsch et al. [142] for NFO films with in-plane compressive strain.

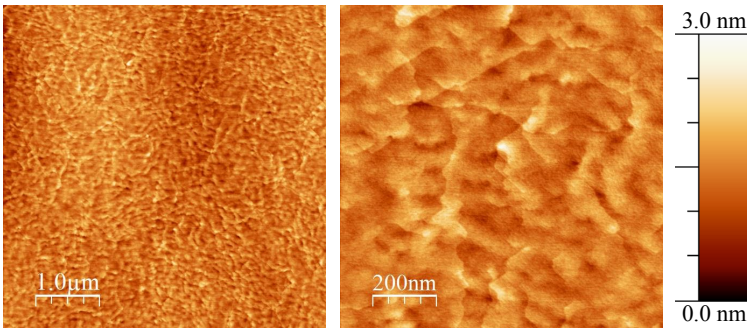

Fig. 3.6: AFM measurements on a 58 nm NFO thin film sputtered at 680°C. Left: 5 μm× 5 μm scan range. Right: 1 μm × 1 μm scan range. In both scan ranges the roughness is remarkably low (σ_{RMS}=0.27 nm, σ_{avg}=0.21 nm).

To confirm the low roughness, additional AFM measurements were conducted. Images of a 5 μm × 5 μm and a 1 μm × 1 μm tapping mode scan are shown in Fig. 3.6, revealing a smooth and homogeneous growth on the MAO (001) substrate. In both cases the roughness is about 0.27 nm (RMS) and 0.21 nm (average). The low roughness of the films is beneficial for the integration of NFO in spin caloric devices, as it enables high interface quality and, therefore, high spin mixing conductances across the interfaces. This might increase the effect amplitude for spin caloric effects considerably [143].

The following sections refer to studies on the 58 nm thick films grown at 680°C.

Electronic properties

Fig. 3.7 depicts the optical absorption spectrum of an NFO film in an energy range from 0.8 eV to 5.6 eV. Experimental data by Holinsworth et al. [42, 144] and a calculated spectrum by Meinert et al. [145] are shown for comparison. The absorption coefficient α(E) was obtained from the measured transmission and reflectance spectra by $\alpha = \frac{1}{d}\ln\left(\frac{1-R}{T}\right)$. The absorption spectrum of the investigated NFO sample is very similar to both that of a PLD fabricated thin film (Holinsworth et al.) as well as to

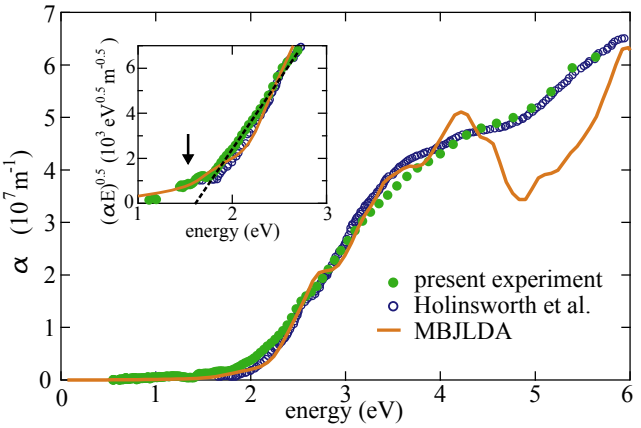

Fig. 3.7: Optical absorption spectrum taken at RT for a NFO film sputtered at 680°C. For comparison, experimental data from Ref. [144] and a theoretical calculation from Ref. [145] are shown. Inset: Tauc plot $(\alpha E)^{0.5}$ versus energy for the determination of the minimum gap. The arrow indicates the mBJLDA minimum direct gap.

the calculated spectrum. The Tauc plot ($(\alpha E)^{0.5}$ versus energy) displayed in the inset of Fig. 3.7 helps to determine the minimum gap, which seems to be slightly smaller than for the PLD film, as indicated by the straight line in the inset. From this plot, a gap energy $E_{\mathrm{gap}} \approx 1.55\,\mathrm{eV}$ is obtained. In contrast to common notion, it has been shown that this type of plot does not necessarily indicate the presence of a direct gap in NFO [145].

Resistivity measurements were performed to study the electronic transport properties of the NFO films. A sample was patterned into a strip of $950\,\mu\mathrm{m}$ length and $70\,\mu\mathrm{m}$ width. The results are shown in Fig. 3.8. At 295 K a RT resistivity of $\rho \approx 12\,\Omega\mathrm{m}$ is found, corresponding to a measured resistance of about $3\,\mathrm{G}\Omega$ in the strip. For the resistivity an uncertainty of at least 15% is estimated, mainly arising from locally not well-defined contacting. This resistivity is one to three orders of magnitude larger than values found in other sputtered NFO thin films, which were deposited in a mixed Ar/O_2 atmosphere [36, 146].

The energy required for the thermally activated charge transport can be derived by linear regression of the temperature dependent resistivity. The

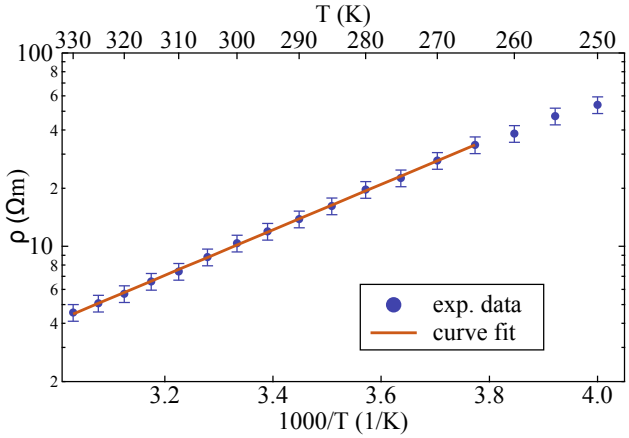

Fig. 3.8: Temperature resolved resistivity measurement on a sample sputtered at 680°C. From the curve fitting an activation energy of 0.23 eV was derived. The error in the data is mainly arising from uncertainties in the contacting and does not significantly alter the outcome of the curve fitting procedure.

ρ vs. 1/T curve was fitted with the equation $\rho \propto \exp(\frac{E_a^{ext}}{k_B T})$ for impurity induced conduction in extrinsic semiconductors in order to determine the thermal activation energy. In the high temperature region above 265 K a straight line segment in the $\ln(\rho)$ plot is present and can be fitted with the above relation (see Fig. 3.8). For the specimen investigated in this project an activation energy $E_a^{ext} = 0.23\,\text{eV}$ is obtained. This result is of the same order as the values found by Lord et al. in sintered NFO specimens, Austin et al. in NFO single crystals, and Ponpandian et al. in NFO nanoparticles [44, 47, 147]. However, the value is six times smaller than the bandgap found by optical spectroscopy in this study. Since the electric conductivity is sensitive to all charge transport mechanisms present in the film, chemical impurities can significantly lower the observed activation energy. As outlined in section 2.1, the conduction mechanism in NFO via hopping along the cation distribution on octahedral lattice sites is very sensitive to impurities and therefore slight deviations in the oxidation states can significantly reduce the activation energy. However, the very high resistivity of the films prompts the conclusion that only a

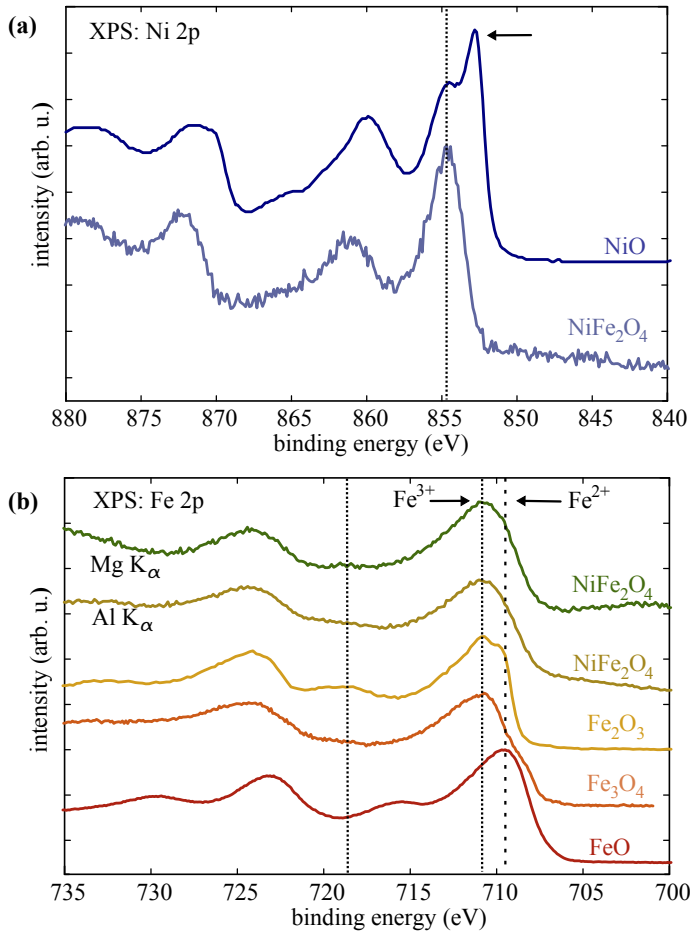

Fig. 3.9: (a) The Ni 2p XPS of NFO with a corresponding NiO spectrum [148] as a reference. (b) The Fe 2p spectrum of NFO recorded with Al Kα and Mg Kα source, respectively. Fe 2p spectra of α-Fe_2O_3, Fe_3O_4, and FeO for comparison [149, 150] are also shown. The dashed line around 719 eV marks the position of a charge transfer feature for Fe^{3+} ions in oxidic materials.

small number of defects is present and that the stoichiometry is close to the desired NFO composition. This aspect is discussed in more detail in the next section.

Cation distribution and element resolved magnetic moments

Ni 2p and Fe 2p core level XP spectra were taken to evaluate the valencies of Ni and Fe. The Ni 2p XP spectrum of NFO (Fig. 3.9(a)) shows the Ni $2p_{3/2}$ (854.2 eV) and Ni $2p_{1/2}$ (871.6 eV) main peaks followed by a rich satellite structure due to corresponding charge transfer excitations. Except for an intense peak at the low binding energy side of NiO [148] (marked by an arrow in Fig. 3.9(a)), which can be attributed to an intrinsic feature found for NiO [151, 152], the Ni 2p spectra of NFO and NiO are very similar to each other. This is consistent for Ni^{2+} ions in a high spin state.

Fig. 3.9(b) displays the Fe 2p XP spectrum of NFO along with reference spectra of α-Fe_2O_3, Fe_3O_4, and FeO for comparison [149,150]. The Fe $2p_{3/2}$ binding energy of 710.8 eV matches that of the corresponding Fe_2O_3 peak. However, since the Fe 2p spectrum recorded with the monochromatic Al K_α source is to some extent overlapped by an Ni $L_3M_{23}M_{45}$ Auger peak the typical charge transfer feature for Fe^{3+} ions in oxidic materials (around 719 eV) appears to be obscured. Therefore, an additional measurement with a standard non monochromatic Mg K_α source was performed. Here the Ni $L_3M_{23}M_{45}$ Auger does not overlap the Fe 2p spectrum and the characteristic charge transfer feature appears, even though somewhat weaker in intensity compared to that of Fe_2O_3. However, the Fe 2p spectrum recorded with the Mg K_α source resembles the hard x-ray PES spectrum of Jaffari et al. [153]. Hence, a divalent Ni and a trivalent Fe valence state in this NFO thin film was observed.

Experimental and computed XAS, XMCD, and XMLD spectra of Ni and Fe are shown in Figs. 3.10 and 3.11. The agreement between experimental and computed spectra for Ni is almost perfect, indicating that Ni^{2+} occupies solely octahedral sites. For Fe, too, a good fit to the measurements is obtained with the parameters given in section 3.2.1. In particular, no characteristic features of Fe^{2+} in the octahedral sites (as in Fe_3O_4) are found, such as a shoulder at the onset of the L_3 and L_2 XAS spectra, a much larger negative first peak in the L_3 XMCD spectrum or a positive peak at the onset of the L_3 XMLD spectrum [137,154]. The corresponding

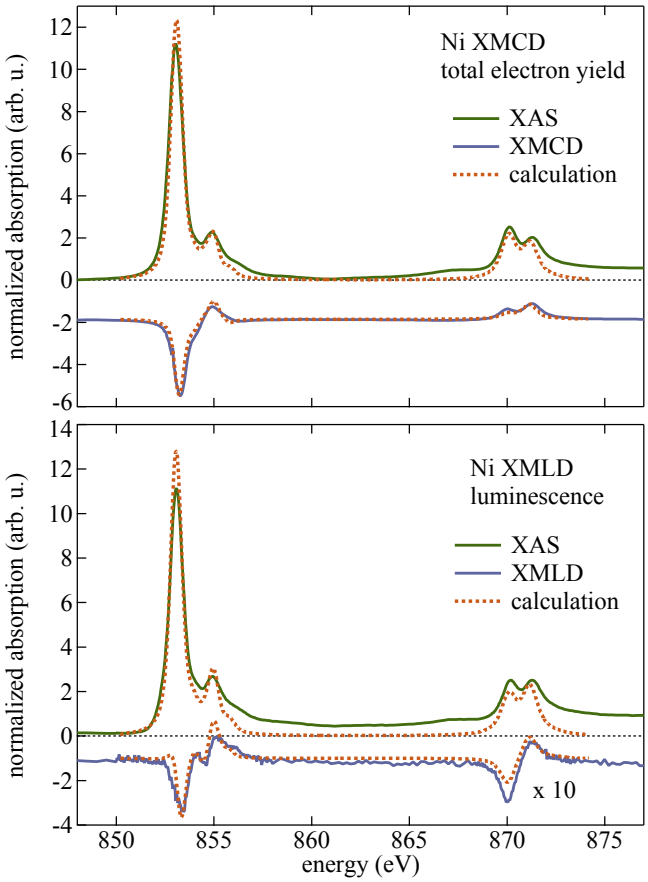

Fig. 3.10: Experimental and computed XAS, XMCD, and XMLD spectra of Ni in NFO. The XAS spectrum is normalized to 1 at 40 eV above the L_3 onset.

positions are marked by arrows in Fig. 3.11. Thus, it may be concluded that there is only a small fraction of Fe^{2+} present at the octahedral positions, in agreement with the XPS results.

Evidence for the complete structural inversion (Fe equally occupies tetrahedral and octahedral positions) comes from the sum rule analysis [108,109] of the Fe XMCD spectrum. The total spin magnetic moment is $m_{\mathrm{spin}}^{\mathrm{Fe}} = (0.10 \pm 0.05)\,\mu_{\mathrm{B}}$ per atom, where the rather large relative uncertainty comes from the non-trivial absorption background structure. The

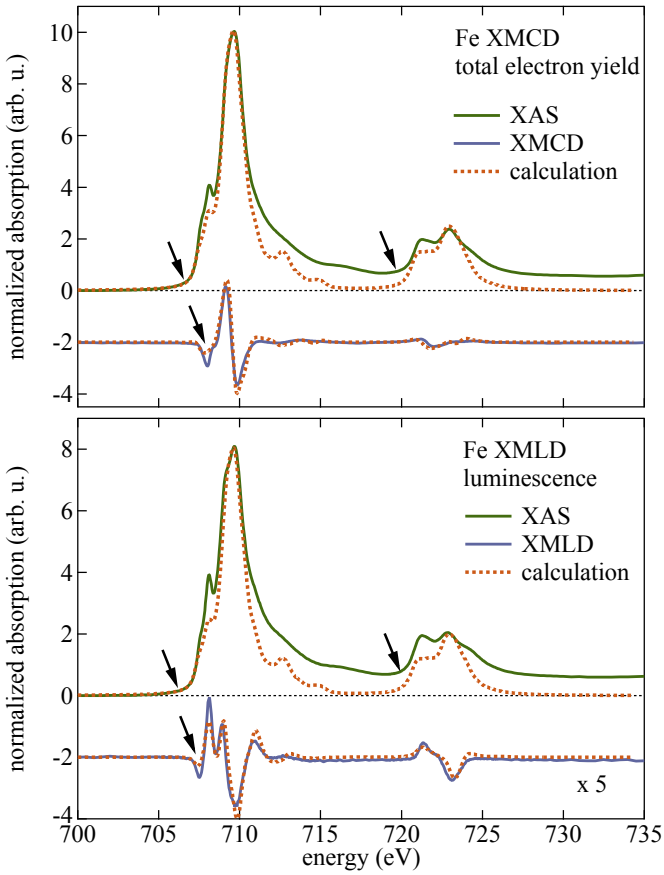

Fig. 3.11: Experimental and computed XAS, XMCD, and XMLD spectra of Fe in NFO. The arrows mark positions at which characteristic features of Fe^{2+} should appear if it was present on octahedral sites. The XAS spectrum is normalized to 1 at 40 eV above the L_3 onset.

ratio of orbital and spin magnetic moments is $m_{\mathrm{orb}}^{\mathrm{Fe}}/m_{\mathrm{spin}}^{\mathrm{Fe}} = (0.12 \pm 0.02)$. Thus, although the XMCD signal of Fe is large in amplitude, pointing to the presence of large magnetic moments, they compensate nearly completely. This is exactly what is expected for the inverse spinel structure, in which the tetrahedral and octahedral Fe^{3+} sites give rise to different XMCD spectra, so they do not compensate. However, the magnetic mo-

ments should cancel nearly exactly [142, 155]. In the normal spinel structure, Fe^{3+} would only occupy octahedral sites and have parallel magnetic moments. Consequently, it is mainly the Ni^{2+} sites that contribute to the macroscopic magnetization. The sum rule analysis of the Ni spectra is difficult due to the complicated background. However, the orbital to spin moment ratio does not depend on the normalization, so it may be deduced with good accuracy. In agreement with an earlier estimate, a ratio of $m_{\mathrm{orb}}^{\mathrm{Ni}}/m_{\mathrm{spin}}^{\mathrm{Ni}} = (0.24 \pm 0.02)$ is found [156]. With the total magnetization of $m = 200\,\mathrm{kA/m}$, i.e., $1.53\,\mu_{\mathrm{B}}$/f.u. from the AGM measurement, the spin magnetic moment of Ni can be deduced to be $m_{\mathrm{spin}}^{\mathrm{Ni}} = (1.06 \pm 0.15)\,\mu_{\mathrm{B}}$ and the orbital magnetic moment $m_{\mathrm{orb}}^{\mathrm{Ni}} = (0.25 \pm 0.10)\,\mu_{\mathrm{B}}$.

3.3 Conclusion

NFO thin films were fabricated by means of DLI-CVD and reactive dc magnetron co-sputter deposition in a pure oxygen atmosphere.

The DLI-CVD fabricated films are in the thickness range of about $1\,\mu$m and show an epitaxial growth with a good crystallinity in the XRD patterns when deposited on (001) oriented MAO substrates. EDX measurements revealed large variations in composition when the films are deposited with identical process parameters, indicating low reproducibility. Exemplary measurements in an AGM were performed to probe the magnetization. The films exhibit small coercive and saturation fields. However, they show significant discrepancies in their magnetic properties, confirming the variations in the deposition processes.

The films fabricated by sputter deposition are significantly thinner, with thicknesses between 28 nm and 58 nm. X-ray diffraction and reflectivity studies on the sputter deposited samples revealed that the films crystallized well with low roughnesses on MAO (001) substrates at different deposition temperatures. A mismatch induced strain was visible for all films, which relaxes for higher deposition temperatures and thicknesses. Magnetic investigations reflected the ferrimagnetic behavior of the sputtered NFO thin films with a reduced magnetization compared to bulk

samples. From the data obtained the ideal deposition temperature for device oriented application was derived to be between 600°C and 700°C. An additional series sputtered at 680°C with comparable crystallographic and magnetic properties showed low roughness and bandgaps very similar to values found in films deposited by pulsed laser deposition. XPS, XAS, XMCD, and XMLD spectra yield a cation distribution as expected for an inverse spinel structure. A nearly complete compensation of the Fe moments on tetrahedral and octahedral sites was observed. The macroscopic magnetization is mainly carried by the Ni^{2+} ions. A semiconducting behavior with a low activation energy of $E_a^{ext} \approx 0.23\,eV$ and a large RT resistivity of about $\rho \approx 12\,\Omega m$ was confirmed by conductivity measurements, further promoting the utilization of sputtered NFO thin films in spin caloric and spintronic applications.

The films synthesized using the two different deposition techniques show different properties, e.g., in their magnetization, which might be attributed to the huge divergence in film thicknesses. Despite the limited reproducibility, the low coercive fields and saturation fields make the chemical vapor deposited films preferable for experiments, where only small magnetic fields are available. The sputtered films are of high quality and exhibit structural and electronic properties that make them very suitable for further spintronic or -caloric experiments. Yet, they show larger switching and saturation fields, more difficult to attain with conventional magnets. Thus, these films are well suited for experiments where large magnetic fields can be realized.

4 Investigations of static magnetic proximity effects in Pt/FM bilayers

This chapter addresses results on the static MPE. XRMR is used to detect proximity induced spin polarizations in bilayers consisting of Pt adjacent to different Ni-Fe-based FMMs ranging from pure Fe to pure Ni. Three different approaches to simulating the magnetooptical profiles of $\Delta\delta$ and $\Delta\beta$ as a function of the coordinate perpendicular to the interface are presented. The optimum fit routine is evaluated. Photon energy dependent data combined with optical data from *ab initio* calculations are used to quantitatively determine the spatial distribution of the induced magnetic moments in Pt across the interface. The interface sensitivity of XRMR and its benefits for investigations of interface spin polarizations are shown in a series of Pt/Fe heterostructures with different Pt thicknesses. The FM thickness dependence of the static MPE is tested in a series of Pt/Fe bilayers with different Fe thicknesses. Furthermore, the induced magnetization is observed depending on the Fe content of the underlying ferromagnet and conclusions are drawn with respect to the coupling strength of the individual materials.
In the second part, the focus lies on the vividly discussed question of a static MPE in Pt adjacent to ferromagnetic semiconductors and insulators. The evaluation of XRMR measurements on Pt/NFO and Pt/YIG bilayers provides upper limits for potential static MPEs in these systems. Some of the results presented here

are published in Ref. [157]/ [158], or submitted for publication [25, 159] and various sections are based on the corresponding articles. Slight differences between the values given here and those in the references originate from small variations in the fitting procedures, but are clearly within the uncertainty limits.

4.1 Experimental and theoretical details

The Pt/FM bilayer samples with metallic FMs were fabricated by dc magnetron sputter-deposition on (001) oriented MAO substrates at RT. The Ar process pressure was $2 \cdot 10^{-3}$ mbar. The Pt/NFO bilayers were deposited both via DLI-CVD on a (001) oriented MAO substrate, analogous to the description in section 3.1 and by reactive sputter deposition in compliance with the procedure outlined in section 3.2. The investigated Pt/YIG and YIG/Pt films were provided by the group from the Walther-Meißner-Institute in Garching and were fabricated by pulsed laser deposition similar to the method used for the samples in Refs. [20] and [21].

The synchrotron measurements were carried out at the resonant scattering and diffraction beamlines P09 of the third generation synchrotron PETRA III at DESY (Hamburg, Germany) [160], BM28 of the ESRF (Grenoble, France) [161], and I16 of the Diamond Light Source (Oxfordshire, United Kingdom) [162]. At all three beamlines a 6-circle diffractometer was used to perform XRR scans in a θ-2θ scattering geometry.

All measurements were performed at RT. Except for the studies at varying photon energies, the XRMR data were collected at a specific energy close to the peak of the Pt L_3 absorption edge, where the dichroic response is supposed to have its maximum. At this photon energy the XRR scans were collected using circularly polarized x-rays, while a magnetic field was switched between parallel and antiparallel orientation to the in-plane projection of the incident beam at every incidence angle. However, since the energy calibrations of the beamlines can differ slightly, the photon energies for each measurement are given within the forthcoming sections along with XA spectra across the Pt L_3 edge.

To apply the external magnetic field at beamline P09 at DESY a four coil electromagnet was constructed at Bielefeld University. The maximum field applied was ±85 mT. The degree of circular polarization was (99±1)% for left and right circular polarization as determined from a polarization analysis with a Au(111) analyzer crystal. Here, all measurements were carried out with left circular polarization after having confirmed that right circularly polarized x-rays change the sign of the XRMR effect. The circular polarization was realized by two 600 μm thick diamond plates at the eight-wave plate condition mounted in series.

At beamline BM28 at ESRF an electromagnet with up to ±200 mT was applied in order to switch the magnetization during the measurements. Here, the degree of circular polarization was $(88 \pm 1)\%$ for left and right circular polarization. The reduced circular polarization has to be taken into account as a factor when deriving quantitative magnetic moments from the reflectivity data. Circular polarization was obtained by utilizing a 780 μm thick diamond crystal at the quarter-wave plate condition. At BM28, the XRMR asymmetry ratios were collected for both polarizations and were averaged afterwards.

At beamline I16 at the Diamond Light Source the same four coil electromagnet was used, as at beamline P09, DESY. Thus, a magnetic field of up to ±85 mT was available in this setup. The degree of circular polarization was $(81 \pm 5)\%$ for left and $(74 \pm 5)\%$ for right circular polarization. The linearly polarized synchrotron radiation was converted to circularly polarized light via a 400 μm thick diamond crystal at the quarter wave plate condition. The degree of circular polarization was determined indirectly from the reduction of linear polarization at the Bragg condition, assuming a total polarization far from the reflex.

From the collected data the non-magnetic reflectivity $I = \frac{I_+ + I_-}{2}$ and the asymmetry ratio $\Delta I = \frac{I_+ - I_-}{I_+ + I_-}$ can be determined, with $I_\pm$, the XRR intensity for positive and negative magnetic field, respectively.

To obtain the magnetic moment of the Pt, the absorption coefficients at the L_3 edge of Pt were calculated for various fixed spin momenta with FDMNES [104] in the full-multiple-scattering mode. The computed ab-

sorption spectra were fitted to experimental values far below and above the edge with the CHOOCH program [163], which also produced the dispersion data by a Kramers-Kronig transformation. It was checked that $\Delta\delta$ and $\Delta\beta$ are directly proportional to the magnetic moment of the Pt.

4.2 Results and discussion

In Fig. 4.1 the absorption of a Pt(3.4 nm)/Fe(9.2 nm) sample at the Pt L_3 edge is presented. The experimental data obtained by fluorescence was taken at beamline P09 at DESY and fits closely to a simulation derived from *ab initio* calculations. The whiteline intensity (ratio of absorption maximum and edge jump) is about 1.31, which indicates a mainly metallic state for Pt (1.25 for metallic Pt, 1.50 for $PtO_{1.36}$, 2.20 for $PtO_{1.6}$) [164]. The simulated spectrum was shifted 1.7 eV to higher energies to fit the experimental data. The maximum of the absorption peak is located at a photon energy of about 11567.5 eV. From the simulation of the Pt absorption edge the dependence of the magnetooptical parameters $\Delta\delta$ and $\Delta\beta$ on the photon energy can be derived. The *ab initio* calculations show the typical behavior of the complex refraction index close to the resonance, i.e., both $\Delta\delta$ and $\Delta\beta$ show finite values in a small range of energies around the absorption edge but vanish far above and below the edge. While the change in absorption $\Delta\beta$ is positive with a maximum at about the peak of absorption, the variation of the dispersion $\Delta\delta$ crosses zero around the absorption edge. However, the maximum in $\Delta\beta$ is slightly shifted to lower energies with respect to the whiteline of the absorption spectrum. For Pt it is well known that the maximum of the magnetic dichroism is located slightly below the absorption edge [117,165]. Therefore, the XRMR asymmetry ratio is expected to be most pronounced for photon energies in this range.

Fig. 4.2(a) shows resonant XRR scans of the Pt/Fe sample for positive and negative magnetic field at a photon energy of 11567.5 eV, in accordance with the maximum of the absorption peak (compare dashed line in Fig. 4.1). The curves are denoted as $I_{\pm}$ for positive and negative magnetic

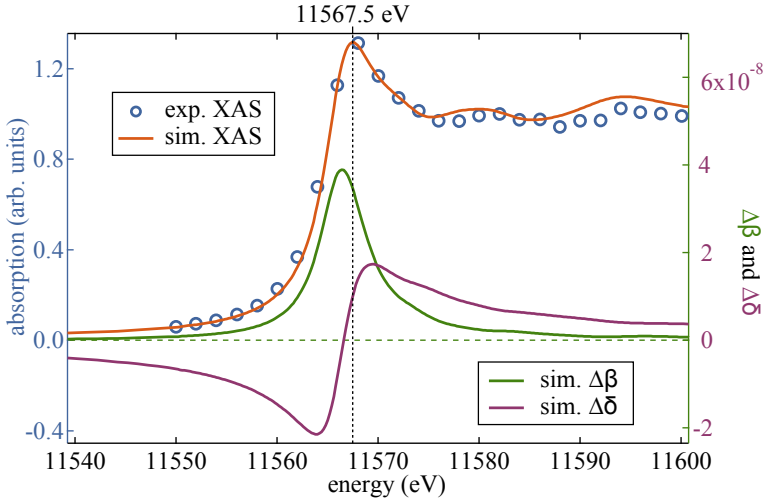

Fig. 4.1: Experimental and calculated energy dependent XA spectra and corresponding simulated magnetooptical parameters $\Delta\delta$ and $\Delta\beta$. The simulations were shifted by 1.7 eV to higher energies to fit the experimental data correctly. The dashed line corresponds to a photon energy of 11567.5 eV at the maximum of the absorption peak.

field, respectively. The XRR intensities are plotted against the scattering vector q. The XRR curve mainly shows oscillations due to the thicker Fe film. Oscillations of larger periodicity caused by the thinner Pt film on top of the supporting Fe layer are superposed upon these strong oscillations but are only barely visible. From this "beating effect" one can estimate that the ratio of Fe to Pt film thickness is roughly 1:3. The thickness, roughness, and the optical constants δ and β of the layers are obtained by fitting the average of the XRR curves. A schematic XRR model consisting of different layers which was used for the simulation is shown as an inset in Fig. 4.2(a). Note that the sketched interfaces only indicate the center of the transition from one material to the other, while the actual width of the transition is determined by the interface roughness. Therefore, the magnetooptical parameters strongly depend on the roughness and along with that the slope of the chemical profile. The Fe thickness is 9.2 nm

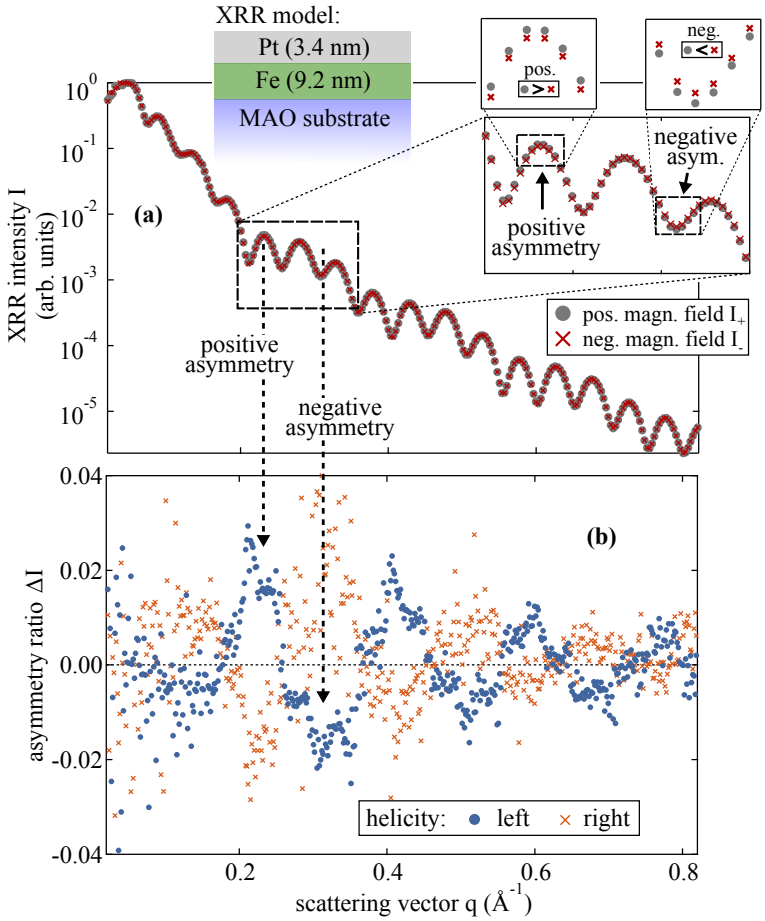

Fig. 4.2: (a) XRR scans for positive and negative magnetic field taken with left photon helicity. (b) XRMR asymmetry ratio of the Pt(3.4 nm)/Fe(9.2 nm) bilayer as derived from the XRR scans for left (blue markers) and right (dashed orange line) photon helicity. The data were taken at a photon energy of 11567.5 eV.

with a roughness of about 0.3 nm and the Pt thickness is 3.4 nm with a roughness of about 0.3 nm.

Calculating the XRMR asymmetry ratio ΔI allows for identifying small deviations between the XRR curves I_+ and I_-, as visible in the zoomed regions in the insets of Fig. 4.2(a). The derived XRMR asymmetry ratio

is displayed in Fig. 4.2(b) for both left and right circular polarization. In both cases, pronounced oscillations are visible with an amplitude of about 2% indicating an induced spin polarization in the Pt. The sign of the effect changes for opposite photon helicities. Additionally, for perpendicular alignment between incident beam and external magnetic field the effect vanishes completely, confirming the magnetic origin of the observed asymmetry. In the following, all measurements were taken with left-handed circular polarization, unless stated otherwise.

4.2.1 Magnetooptical profiles

In order to extract the spin polarization of the interfacial Pt from the experimental data, the XRMR curve has to be fitted by implementing the change in the optical constants as magnetooptical parameters $\Delta\delta$ and $\Delta\beta$ with a certain spatial distribution across the interface. An overview of three different approaches, used to simulate the asymmetry ratio of the Pt(3.4 nm)/Fe(9.2 nm) hybrid (see Fig. 4.2(b)) by modeling different magnetooptical profiles, is presented in Fig. 4.3. In all cases, the structural and optical properties from the evaluation of the reflectivity in Fig. 4.2(a) were used for the simulations.

In the first approach, depicted in Fig. 4.3(a), the Pt film is divided into an unpolarized layer and an additional fully spin polarized layer with a finite roughness (see inset (a)). The resulting magnetooptical profiles for $\Delta\delta$ and $\Delta\beta$ arise from the convolution of the magnetooptical parameters with the interface roughnesses between the two separate Pt layers and between the spin polarized Pt and the Fe film. The illustrated distribution of $\Delta\delta$ and $\Delta\beta$ was obtained by fitting the thickness, the roughness, and the magnetooptical constants of the polarized Pt layer, while keeping the total Pt thickness constant. However, in order to limit the set of fit parameters, the $\Delta\beta/\Delta\delta$ ratio was fixed at 3.4, as derived from the optical data from the *ab initio* calculations at the applied photon energy of 11567.5 eV (see dashed line in Fig. 4.1). The effective spin polarized film thickness appears to be about (1.1 ± 0.1) nm in this model, while the roughness derived through fitting is about 0.4 nm.

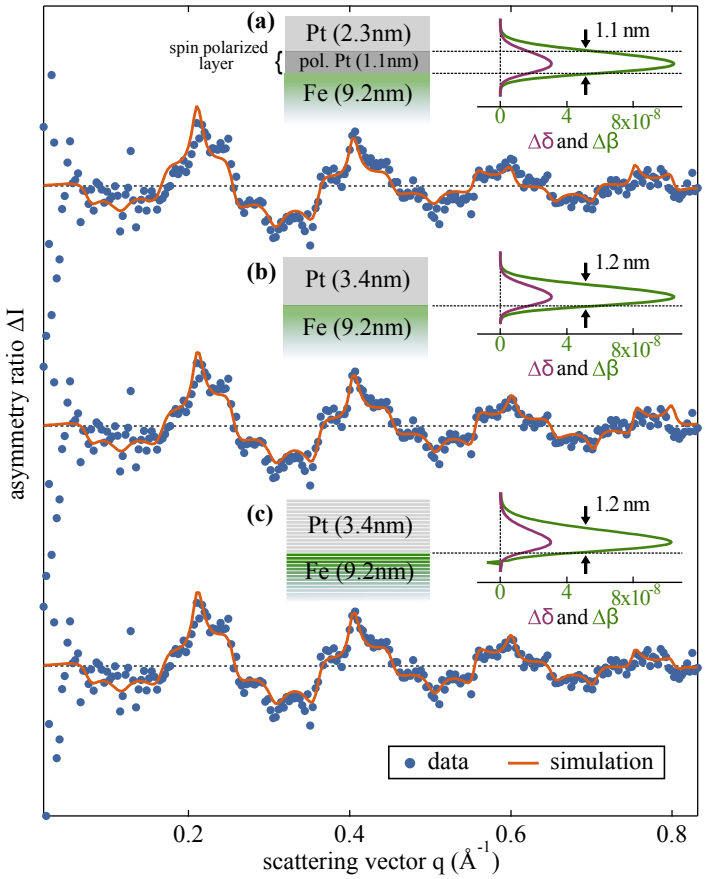

Fig. 4.3: The XRMR asymmetry data was fitted using three different approaches, i.e., (a) insertion of a thin spin polarized layer in the Pt, (b) convolution of a Gaussian shaped magnetooptical profile with the Pt/Fe interface roughness, and (c) an adaptive layer segmentation with separate spin polarized layers. For each model the asymmetry ratio simulation and the corresponding magnetooptical profile are displayed.

The second model is illustrated in Fig. 4.3(b). Instead of including an additional Pt layer, the magnetooptical profiles are estimated by a convolution of a Gaussian shaped profile with the interface roughness. In this approach the median, the variance and the amplitudes, $\Delta\delta$ and $\Delta\beta$ of the Gauss distributions, are fit parameters. Again, $\Delta\beta/\Delta\delta$ was set to

3.4. This approach results in a fit curve very close to the experimental data and a realistic magnetooptical profile. The FWHM of the magnetooptical profiles, i.e., the effective width of the spin polarized Pt, is about (1.2 ± 0.1) nm. This approach was also used by Brück et al. to model the asymmetry ratio of spin polarized Mn in Fe/MnPd bilayers [166].

The third model is shown in Fig. 4.3(c). Here a layer segmentation is used to simulate the spatial distribution of $\Delta\delta$ and $\Delta\beta$. Starting with the profile from the second model, the system is divided into thin sublayers with a distinct thickness and zero roughness. In this case the interface roughnesses are modeled by a gradual transition of the optical constants from one sublayer to the other. Each of the sublayers can exhibit a finite value for $\Delta\delta$ and $\Delta\beta$, which are fitted to obtain the best simulation for the experimental data. This allows for a high degree of freedom for the shape of the magnetooptical profiles. Again, the resulting FWHM of the magnetooptical profiles is about (1.2 ± 0.1) nm.

During evaluation of the three approaches, distinct differences between the simulated and experimental data appear. The first model of a spin polarized Pt interlayer shows the largest deviations between simulation and experiment. This is reflected in a larger χ^2 goodness of fit of $\sim 1.85 \cdot 10^{-5}$ compared to $1.46 \cdot 10^{-5}$ for the second model and $1.25 \cdot 10^{-5}$ for the third model. Also, since the roughness is treated as a Gaussian distribution around the interface, the results may not altogether fit this model if the roughness is in the same range or larger than the polarized interlayer thickness. The second model leads to a convincing fit but shows some slight deviations for high values of the scattering vector q, while the third model describes the data very well for the entire range. However, this model requires prior evaluation of the experimental data based on one of the other models, consumes much more computing time and works with a large set of correlated fitting parameters. Despite these increased expenses, the improvement of the fit is marginal. Further, the magnetooptical profiles of all three approaches differ only slightly. Within the experiment the second model simulates the data with the smallest number of parameters

and results in a plausible fit. Therefore, this model was chosen for the following data evaluation.

4.2.2 Photon energy dependence

In order to determine the exact magnetic moment per atom induced in the Pt, photon energy dependent XRMR measurements were taken on the same Pt/Fe sample as exploited in the previous section. However, these studies were performed in a subsequent experiment. Since the experiments were carried out six months apart, only asymmetry ratios gained during this measurement series were taken into account for the analysis of the energy dependence of the magnetooptical parameters. Discrepancies between the results from former measurements (as presented in the previous section) and the energy series performed here are discussed later in this section. Again, the measurements were performed at beamline P09 at DESY for photon energies between 11540 eV and 11600 eV around the Pt L_3 absorption edge (see Fig. 4.4(a)). Beyond this range the amplitude of the asymmetry ratio vanishes almost completely, while it is most pronounced for energies between 11565 eV and 11571 eV, close to the absorption edge. Due to the absence of dichroic effects in the off-resonant regions far above and below the edge any influences from other absorption edges can be excluded. In Fig. 4.4(a) the region between q= 0.2 Å^{-1} and q= 0.4 Å^{-1} is highlighted, and a dashed line marks the position of the first minimum of the asymmetry ratio to illustrate the phase shift in the asymmetry ratio with respect to the photon energy. The evaluation indicates that the phase shift is mainly determined by the change of $\Delta\delta$, while the change in amplitude is primarily governed by the variation of $\Delta\beta$ with energy. This correlation can be seen by comparing the amplitude and phase shift of the asymmetry ratios depicted in Fig. 4.4(b) with the simulated curve of the magnetooptical parameters $\Delta\delta$ and $\Delta\beta$, shown in Fig. 4.1.

Prior to the asymmetry ratio, the non-magnetic XRR curves, obtained from averaging the XRR curves measured for positive and negative field, are fitted. The structural parameters are deduced from the reflectivity

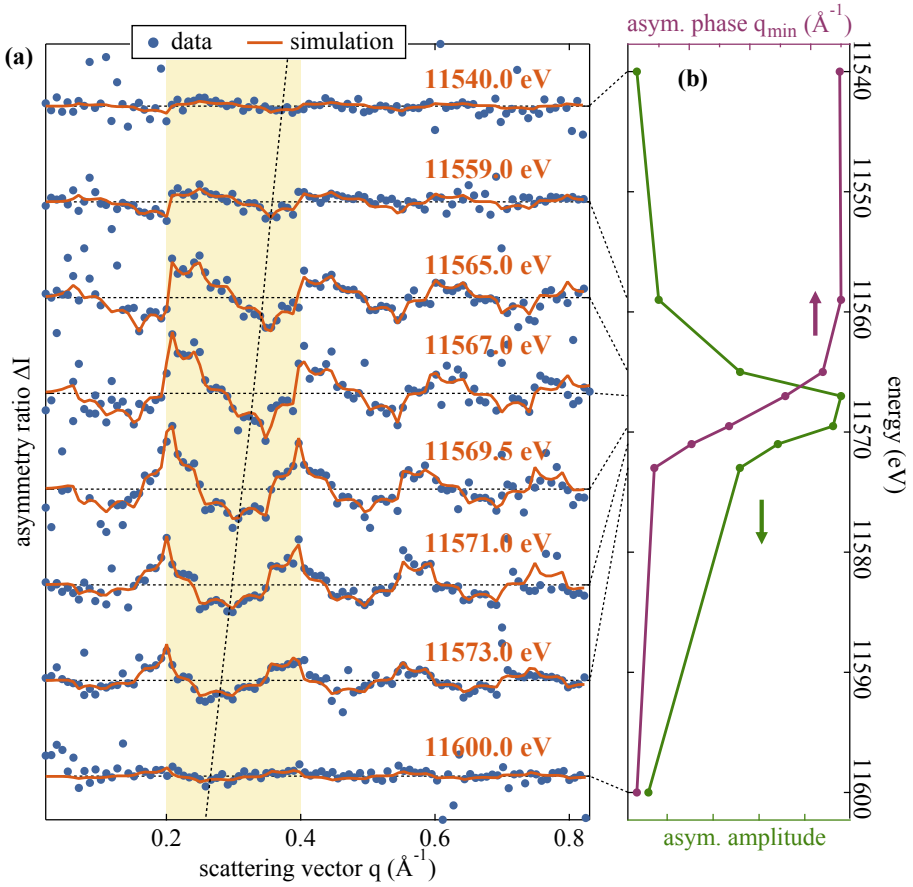

Fig. 4.4: (a) XRMR asymmetries and fits for Pt(3.4 nm)/Fe(9.2 nm) at different photon energies around the Pt L_3 absorption edge. The region between q= 0.2 Å^{-1} and q= 0.4 Å^{-1} is highlighted to illustrate the phase shift. The positions of the minima are further traced by a dashed line. (b) Asymmetry amplitude and phase shift of the oscillations, as evaluated from the raw asymmetry data.

data collected off-resonant, at a photon energy of 11540 eV, and kept constant for the remaining energies, while only the optical parameters δ and β were adjusted to the XRR scans. Based on these values, the spatial distribution and the quantitative values of the magnetooptical parameters are extracted from simulations of the asymmetry ratios. As outlined in

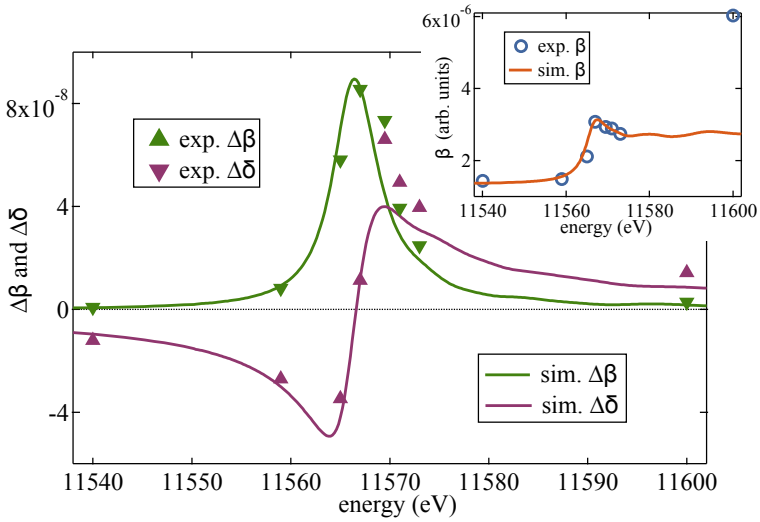

Fig. 4.5: Magnetooptical parameters as derived from the energy dependent XRMR studies on Pt(3.4 nm)/Fe(9.2 nm). The corresponding simulation from *ab initio* calculations was scaled to the experimental data in order to extract the magnetic moment. The inset displays the absorption coefficient β, which was experimentally obtained from simulations of the respective XRR curves.

the previous section the XRMR data are fitted using the second simulation model based on a Gaussian shaped magnetooptical profile convoluted with the interface roughness, as described in section 4.2.1. Again, the ratio $\Delta\beta/\Delta\delta$ is fixed to the corresponding values for each energy which are obtained from the *ab initio* calculations for spin polarized Pt (see Fig. 4.1).

A comparison between the results from simulations of the experimental data and theory is displayed in Fig. 4.5. The experimentally determined values for the magnetooptical parameters $\Delta\delta$ and $\Delta\beta$ show the predicted behavior. The magnetic moment induced in the Pt by magnetic proximity is determined by scaling the magnetooptical data from the *ab initio* calculations to these values as illustrated in Fig. 4.5. Again, the calculated spectra are shifted to higher energies by 1.7 eV, taking into account the experimental XAS shown in Fig. 4.1. A magnetic moment of

$m_{\mathrm{Pt}} = (0.46 \pm 0.10)\,\mu_{\mathrm{B}}$ per Pt atom in a (1.2 ± 0.1) nm thick effective layer at the interface to the Fe is found. This value is somewhat smaller than the value found for the identical sample during the previous measurements at 11567.5 eV in a prior beamtime (see Fig. 4.2). From the evaluation of the corresponding XRMR curve and the resulting magnetooptical profile, as presented in Fig. 4.3, a magnetic moment of $m_{\mathrm{Pt}} = (0.61 \pm 0.10)\,\mu_{\mathrm{B}}$ can be derived for the first experiment.

In the following the two subsequent experiments are labeled experiment A (first measurement taken at a photon energy of 11567.5 eV) and experiment B (measurements taken six months later within the energy variation series) for reasons of clarity. In particular, the data taken at a photon energy of 11567 eV within experiment B are compared to experiment A. The slightly different photon energies in experiment A and B are considered within the $\Delta\beta/\Delta\delta$ ratios.

The reason for the discrepancies in the observed magnetic moments is open for speculation. Since many parameters, both optical and structural, can have a strong impact on the magnetooptical response in XRMR experiments, a definite assignment of the deviations observed in the respective data to a certain origin is challenging.

The energy dependence of the absorptive correction β_{Pt} of the Pt layer was derived from fitting the energy dependent XRR curves taken in experiment B and is shown in the inset of Fig. 4.5 along with a theoretical calculation of the Pt absorption spectrum scaled to the data. Apart from an outlier at a photon energy of 11600 eV, the experimental β_{Pt} values from the XRR evaluation are well in line with the theoretical absorption spectrum. The absolute values deviate slightly from the values tabulated in the Henke tables [130]. Off-resonant, the literature values of the absorptive correction are $\beta_{\text{pre-edge}} \approx 1.4 \times 10^{-6}$ before and $\beta_{\text{post-edge}} \approx 3.5 \times 10^{-6}$ beyond the edge, while the experimentally derived values are $\beta_{\text{pre-edge}} \approx 1.4 \times 10^{-6}$ and $\beta_{\text{post-edge}} \approx 2.7 \times 10^{-6}$. Thus, the experimental edge jump is smaller than the literature value by a factor of about 0.6.

At the resonance, the XRR fitting yields a maximum value of $\beta_{\text{reson.}} \approx 3.1 \times 10^{-6}$ at a photon energy of 11567.0 eV. This corresponds to a whiteline intensity of about 1.3, in good agreement with the peak height found in the experimental XAS (see Fig. 4.1), and confirms the reliability of the XRR results. However, an evaluation of the reflectivity data taken in experiment A based on the structural parameters determined in the energy series does not yield satisfying agreement between the simulation and the experimental data.

These discrepancies prompt the assumption that the structural parameters have changed slightly in the time between the experiments. Since the experiments were performed six months apart, one possible reason for the changes in the curves might be aging effects altering the surface and the interfaces of the investigated sample. This could result in a different interface coupling between the Fe and the Pt film and, thus, influence the magnetic response. Additionally, the XRR results of experiment A yields significantly larger values of β_{Pt} than the subsequent energy dependent experiments. This does also have a considerable impact on the analysis of the induced magnetic moment. Therefore, the influence of β_{Pt} on the XRMR evaluation will be discussed in the next section.

4.2.3 Influence of optical parameters on the XRMR asymmetry ratio

The change in the optical constants δ_{Pt} and β_{Pt} with magnetization, i.e., the magnetooptical parameters $\Delta\delta$ and $\Delta\beta$ represent a direct measure for the spin polarization of a medium. However, the absolute magnitude of δ_{Pt} and β_{Pt} can also have a strong impact on the outcome of simulations of the XRMR asymmetry and influence the width and magnitude of the resulting magnetooptical profiles. Therefore, the correct determination of the optical constants is crucial for an accurate evaluation of the magnetic interface properties, as the magnetooptical response in the XRMR simulations is highly sensitive to slight varations of δ_{Pt} and of β_{Pt} of the Pt layer.

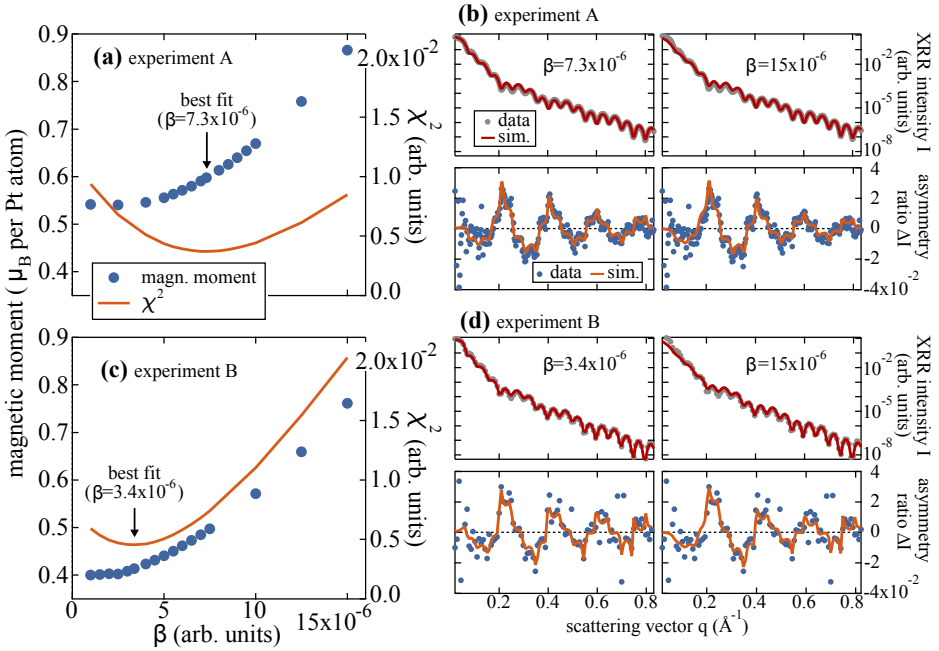

Fig. 4.6: Magnetic moments, as derived from the XRMR asymmetry ratios from (a) experiment A and (c) experiment B, using different β values in the prior XRR evaluation. (b) and (d) display graphs of the corresponding XRR and XRMR simulations.

To illustrate this dependence, different simulations were performed for experiments A and B with different β_{Pt} values. (Note: The scan taken at a photon energy of 11567 eV during experiment B is considered in the comparison) The simulations were carried out by fitting the XRR curves with a fixed β_{Pt}. With this approach several simulations were carried out for β_{Pt} values between $1 \cdot 10^{-6}$ and $15 \cdot 10^{-6}$. In each case, first the XRR curve was fitted for a certain β_{Pt} value, while the other optical and structural parameters were completely free during the fitting procedure. The results from the fit were then used as an input for the subsequent XRMR analysis, where only the magnetooptical profile was varied analogously to the approach in section 4.2.1.

The results of the simulations are shown in Fig. 4.6. Here the resulting moments are displayed for both experiments. In order to compare the quality of the fit results, the χ^2 values for each XRR simulation are also plotted. In each graph, the minimum in χ^2 corresponds to a fit with all structural and optical parameters fitted freely, including β_{Pt}.

Fig. 4.6 (a) shows simulations for experiment A. The β_{Pt} dependence reveals that for larger values of β_{Pt} the resulting magnetic moment increases significantly. The goodness of fit χ^2 exhibits a minimum in terms of a best fit around $\beta_{\mathrm{Pt}} = 7.3 \cdot 10^{-6}$.

Analogously, Fig. 4.6 (c) shows the same simulations for experiment B. The χ^2 minimum of the simulations is located at $\beta_{\mathrm{Pt}} = 3.4 \cdot 10^{-6}$, a much smaller value than in experiment A. The trend of an increase of the magnetic moment for increasing β_{Pt} is also observable in this set of simulations. Yet, the overall magnetic moments are distinctly smaller than the ones obtained from the data of experiment A.

When comparing the results from experiments A and B large discrepancies are visible, even though the same sample was analyzed, just at different times. Fitting of the reflectivity data from experiment A with a complete set of free parameters (best fit) yields a magnetic moment of about $(0.61 \pm 0.10)\,\mu_{\mathrm{B}}$ per atom in the effective spin polarized volume, as published in Ref. [157]. For experiment B the magnetic moment gained from the best fit is $(0.41 \pm 0.10)\,\mu_{\mathrm{B}}$ per Pt atom in the spin polarized volume. (Note that this value differs slightly from the moment found in the previous section within the analysis of the energy dependent data, since here the structural parameters were also fitted, while before they were set to the values determined off-resonantly. However, this deviation is small and within the error bars of $\pm 0.10\,\mu_{\mathrm{B}}$ per Pt atom.)

Selected results from fitting the XRR and XRMR data from experiments A and B are presented in Fig. 4.6 (b) and (d), respectively. In each case, the simulations for the best fit, i.e., the minimum in χ^2, and for a fit with $\beta_{\mathrm{Pt}} = 15 \cdot 10^{-6}$ are displayed. As obvious from the χ^2 values, the XRR simulations from the best fit ($\beta_{\mathrm{Pt}} = 7.3 \cdot 10^{-6}$ in experiment A and $\beta_{\mathrm{Pt}} = 3.4 \cdot 10^{-6}$ in experiment B) and the fit with $\beta_{\mathrm{Pt}} = 15 \cdot 10^{-6}$ strongly

differ in quality, especially in experiment B, where the slope of χ^2 vs β_{Pt} is very steep. However, in both experiments the XRMR simulations result in very similar curves. The comparison shows that the same asymmetry ratio can be reproduced by simulations based on magnetooptical profiles with very different magnitudes, depending on the optical and structural parameters. Therefore, the evaluation of the asymmetry ratio is not entirely unambiguous, but can result in strongly differing magnetic moments if the XRR analysis contains uncertainties. In particular, the simulations with a variation of the absorptive correction clearly show, that a larger β_{Pt} in the XRR fitting results in a larger magnetic moment found in the XRMR analysis.

Analogously to the variation of β_{Pt}, changes in the dispersive correction δ_{Pt} show a similar trend. Determining the structural and optical parameters with a fixed δ_{Pt} in the XRR analysis and using the values found for the subsequent XRMR analysis results in an increase of the magnetooptical profiles with increasing δ_{Pt}.

The discrepancies between the magnetic moments for different δ_{Pt} and β_{Pt} values indicate that detailed knowledge of the optical parameters is important for a reasonable XRMR analysis. From the Henke tables [130], a value of $\beta_{\mathrm{Pt}} = 3.56 \cdot 10^{-6}$ can be extracted for energies just above the L_3 edge jump. However, the tabulated values are not completely accurate, in particular in close vicinity to an absorption edge, but more or less describe a step function across the edge, neglecting the occurrence of fine structure features and the whiteline peak at the resonance. Thus, they only give a rough estimate of the real absorption coefficient. For the results from experiment B the XRR fit with a complete set of free fitting parameters converges at $\beta_{\mathrm{Pt}} = 3.4 \cdot 10^{-6}$, close to the literature value (Note: This value also differs slightly from the value given in section 4.2.2, since the structural parameters were also fitted in this evaluation.). The data taken within experiment A, however, yields an absorption coefficient of $\beta_{\mathrm{Pt}} = 7.3 \cdot 10^{-6}$, when all parameters are fitted freely. This value deviates by more than a factor of 2 from the literature value, which suggests that the analysis of the magnetooptical parameters and, thus, the induced

magnetic moment, contains uncertainties in this procedure. However, the differences in the curve fitting, leading to different β_{Pt} values for the two experiments, do not completely account for the large differences in the magnetic moments. In particular, the magnetic moments gained from the different simulations of experiment B are overall at a lower level than the values obtained for experiment A.

Besides the optical parameters, the structural parameters can also have a large influence on the magnitude of the magnetooptical response. In particular, the roughness between the NM and the FM layer can affect the magnetic coupling significantly. Therefore, for the correct evaluation of the magnetooptical profiles, an exact determination of the roughnesses is imperative. However, in experiment A the XRR was only collected resonantly at the $\mathrm{L_3}$ absorption edge at a photon energy of 11567.5 eV, which can introduce uncertainties in the analysis of both the optical and structural parameters. The steep change in the optical constants, due to anomalous charge scattering at energies across the absorption edge, results in a rapid change of the reflectivity properties of a medium with changing photon energy. Especially, for a layer system consisting of materials with a small contrast in their optical properties, the vicinity of an absorption edge can have a strong impact on the sensitivity to interfacial roughness.

For a more precise quantitative evaluation of the induced magnetic moments, off-resonant XRR measurements are beneficial. Far from the influence of an absorption edge, the structural parameters can be determined more accurately by relying on literature values for the optical parameters. Knowing the correct structural properties one can then derive the optical constants around the resonance by keeping the thicknesses and the roughnesses fixed in the resonant XRR analysis. Using the parameters gained in this procedure as input for the subsequent XRMR analysis enables a more unambiguous determination of the magnetooptical profiles and consequently of the induced magnetic moments per atom in the spin polarized volume. This approach was already outlined in Fig. 2.14.

However, as mentioned in the previous section, the structural parameters determined from XRR collected off-resonantly within the energy series

in experiment B do not yield satisfactory results in the simulations of the XRR curves taken in experiment A, which strongly implies that the sample has experienced a structural transformation in the interval between the experiments. From the data available on this sample, a profound evaluation of the exact origin of these discrepancies is not possible any more. Yet, even within these deviations the values derived from both experiment A and B are in agreement with the magnetic moments per Pt atom in Pt/Fe bilayers reported in Ref. [114].

4.2.4 Pt thickness dependence

In order to investigate the interface sensitivity of XRMR, a series of Pt(x nm)/Fe($\sim$ 10 nm) double layers with Pt thicknesses between 1.8 nm and 20 nm was analyzed. The data were taken at DESY at a photon energy of 11567.5 eV. Thus, the $\Delta\beta/\Delta\delta$ was again set to a constant value of 3.4 in the evaluation of the asymmetry ratios. The results of the XRR and XRMR experiments are presented in Fig. 4.7. The experimental XRR curves with the corresponding simulations are displayed in the panels (a), (c), and (e). The Pt film thicknesses, as derived from the curve fittings, are 1.8 nm, 5.8 nm, and 20 nm, which are also given in the respective insets. The XRMR data and simulations are displayed in Fig. 4.7 (b), (d), and (f). Since the signal-to-noise-ratio was particularly poor for the 1.8 nm Pt sample, the asymmetry ratio was averaged over 8 measurements.

The XRMR curves all show a similar amplitude of about 2%, which is consistent with the 3.4 nm Pt sample discussed previously. The magnetooptical profiles, i.e., the spatial distribution of the induced spin polarizations, are shown in Fig. 4.7 (g). All magnetooptical profiles are in the same range, thus, the bilayers show comparable Pt spin polarizations. The spin polarized volumina are between (1.2 ± 0.1) nm and (1.3 ± 0.1) nm in width. Again, by scaling to optical data from *ab initio* calculations, the induced magnetic moments per atom can be estimated. The calculated moments are $(0.42 \pm 0.10)\,\mu_B$ per Pt atom for 1.8 nm Pt, $(0.48 \pm 0.10)\,\mu_B$ per Pt atom for 5.8 nm Pt, and $(0.44 \pm 0.10)\,\mu_B$ per Pt atom for 20 nm Pt. Thus, the films all exhibit a very similar magnetic moment. This indicates

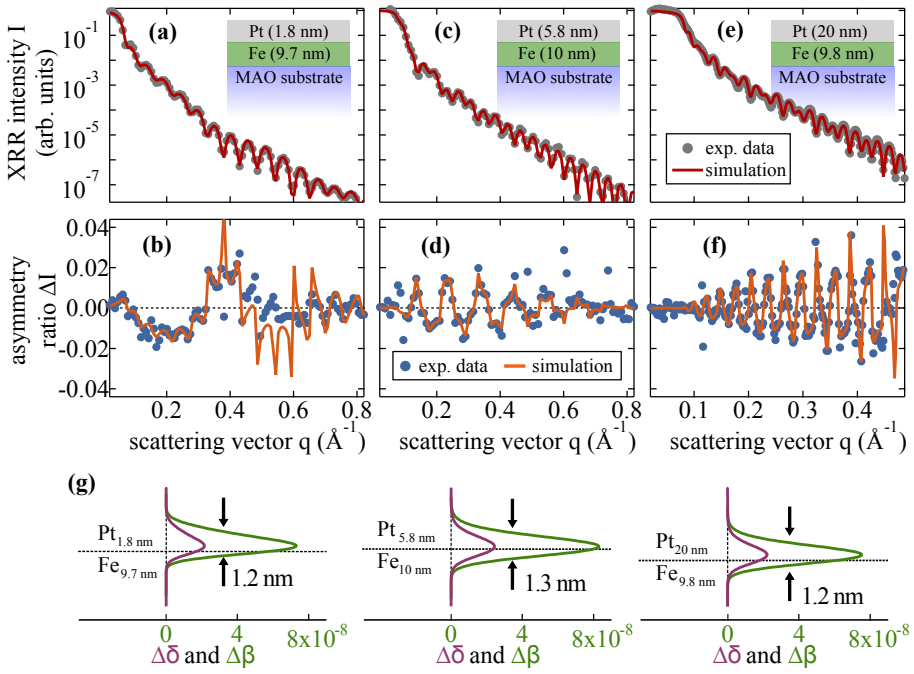

Fig. 4.7: XRR intensity I and corresponding asymmetry ratios ΔI for Pt(x nm)/Fe with (a),(b) $x = 1.8$ nm Pt and 9.7 nm Fe (average of 8 curves), (c),(d) $x = 5.8$ nm Pt and 10 nm Fe and (e),(f) $x = 20$ nm Pt and 9.8 nm Fe. For the asymmetry simulations the magnetooptical profiles in (g) are used.

that the observed effect is mainly independent of the film thickness, i.e., the static MPE induces a similar spin polarization for all film thicknesses in the range investigated. The short range interface interaction only influences a few monolayers of the Pt, which is reflected in the narrow spatial distribution of the magnetooptical profile. This is well in line with the theoretical predictions for the static MPE [54, 58]. Thus, a significant deviation from these findings can be expected only for Pt film thicknesses in the sub-nanometer range.

The magnetic moment derived for the 3.4 nm thick Pt was $(0.46 \pm 0.10)\,\mu_B$ per Pt atom in experiment B, which is also well in line with these findings for the Pt thickness dependent series. The large mag-

Tab. 4.1: Overview of induced magnetic moments derived from XRMR studies on Pt/Fe bilayers with different Pt thicknesses.

composition	Pt thickness (nm)	FM thickness (nm)	magnetic moment (μ_B per atom)
Pt/Fe	1.8	9.7	0.42
	3.4	9.2	0.61 (exp. A)
			0.46 (exp. B)
	5.8	10.0	0.48
	20.0	9.8	0.44

netic moment of up to $(0.61 \pm 0.10)\,\mu_B$ per Pt atom as derived in experiment A, however, deviates slightly from these values, most probably due to structural differences in the samples. The magnetic moments for the different double layers are summarized in Tab. 4.1.

The thickness independence of the XRMR asymmetry ratios and the derived magnetic moments clearly demonstrate the high interface sensitivity of this technique, while the absolute volume of the Pt film only has minor influence on the magnetooptical response. This is particularly beneficial when probing interfacial spin polarizations. It allows to directly examine the devices from spin caloritronic experiments, regardless of their film thicknesses, while for XMCD it can be necessary to measure different samples with smaller Pt thickness. Therefore, XRMR represents a powerful approach to investigate the static MPE and is an important alternative to the thickness dependent XMCD.

4.2.5 Fe thickness dependence

In addition to the investigation of the Pt thickness, the Fe thickness was also varied in order to test it for a correlation with the induced spin polarization. A series of Pt($\sim 3\,$nm)/Fe($x\,$nm) bilayers of different Fe thicknesses was deposited on MAO substrates by sputter deposition, in analogy

to the samples discussed in section 3.2. In contrast to the previous XRR and XRMR experiments, the experiments on the Pt($\sim$ 3 nm)/Fe(x nm) series were carried out at beamline BM28 at the ESRF.

On each sample non-magnetic off-resonant and resonant XRR curves were collected at photon energies of 11465 eV and 11565 eV, respectively. In order to find an accurate model for the structural and optical parameters, the reflectivities were evaluated sequently, according to the procedure outlined in section 2.4.2, i.e., first the off-resonant XRR was fitted using literature values for the optical constants and subsequently the resonant XRR was evaluated using the structural information from the off-resonant fit. The resonant XRR curves, along with the corresponding simulations, are displayed in Fig. 4.8 (a), (c), and (e). The Fe film thicknesses, as derived from the curve fittings, are 1.1 nm, 5.7 nm, and 18.2 nm, while the Pt layers vary between 3.2 nm and 3.4 nm. The precise values are displayed in the respective insets.

The XRMR data were also collected at a photon energy of 11565 eV and evaluated, using the structural and optical parameters gained from the XRR simulations. The asymmetry ratios taken on the heterostructures with Fe film thicknesses of 1.1 nm and 5.7 nm are averaged over two data sets, i.e., one for left and one for right photon helicity. For the sample with the thickest Fe film four data sets have been used for averaging (two for each light polarization). Note that before averaging the data, the sign of the curves taken with right handed circular polarization was reversed. The experimental XRMR data, along with the respective simulations, are shown in Fig. 4.8 (b), (d), and (f). The corresponding magnetooptical profiles are displayed in Fig. 4.8 (g). In this experiment a $\Delta\beta/\Delta\delta$ ratio of -3.5 was determined for the energy applied, using energy dependent measurements of the magnetic response at a fixed scattering vector q, i.e., the value of the first maximum in the XRMR scans. The result is shown exemplarily for the Pt(3.3 nm)/Fe(5.7 nm) hybrid structure in Fig. 4.8 (h), along with the theoretical predictions for the magnetooptical parameters from *ab initio* calculations. The data were taken at a scattering vector of $q = 0.22\,\text{Å}^{-1}$. The calculated $\Delta\delta$ and $\Delta\beta$ spectra are shifted in energy

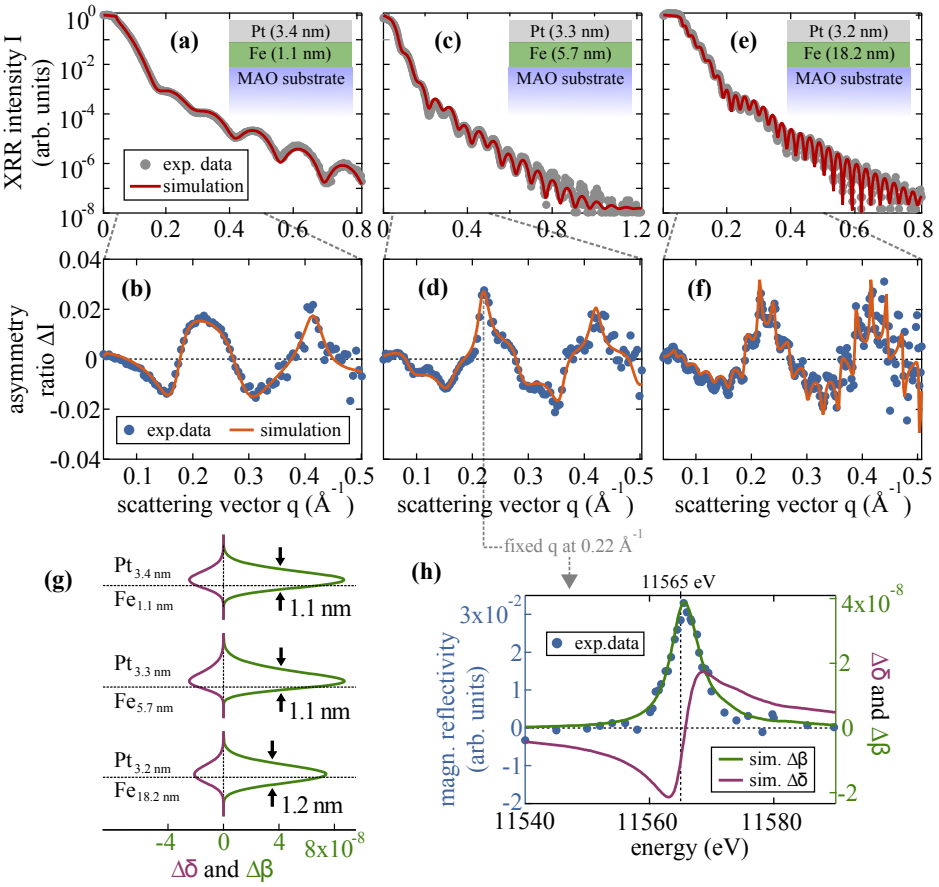

Fig. 4.8: XRR intensity I and corresponding asymmetry ratios ΔI for Pt/Fe with (a),(b) 3.4 nm Pt and $x = 1.1$ nm Fe (average of 2 curves), (c),(d) 3.3 nm Pt and $x = 5.7$ nm Fe (average of 2 curves), and (e),(f) 3.2 nm Pt and $x = 18.2$ nm Fe (average of 4 curves). For the asymmetry simulations the magnetooptical profiles in (g) are used. The magnetic response for varying photon energy from the Pt(3.3 nm)/Fe(5.7 nm) bilayer and simulations of $\Delta\delta$ and $\Delta\beta$ from *ab initio* calculations are displayed in (h). The experiment was performed at a fixed scattering vector $q = 0.22\,\text{Å}^{-1}$. The XRMR was carried out at a photon energy of 11565 eV (dashed vertical line) yielding a $\Delta\beta/\Delta\delta$ ratio of -3.5.

to fit the position of the experimental data. The dashed line marks the photon energy at which the resonant measurements were conducted and

Tab. 4.2: Overview of induced magnetic moments derived from XRMR studies on Pt/Fe bilayers with different Fe thicknesses.

composition	Pt thickness (nm)	FM thickness (nm)	magnetic moment (μ_B per atom)
Pt/Fe	3.4	1.1	0.53
	3.3	5.7	0.53
	3.2	18.2	0.45

defines the $\Delta\beta/\Delta\delta$ ratio. Since it is located at slightly smaller energies than the maximum of the magnetic reflectivity, the $\Delta\beta/\Delta\delta$ ratio is negative. It has to be noted that, since the energy dependent asymmetry ratio is collected in reflectance instead of fluorescence, it does not solely correspond to the magnetic response from the absorption, like in XMCD experiments, but also contains dispersive contributions.

Again, the magnetic moments per Pt atom are determined by scaling the magnetooptical parameters to optical data from *ab initio* calculations, taking into account the slightly reduced photon polarization of $(88 \pm 1)\%$. The calculated moments are $(0.53 \pm 0.10)\,\mu_B$ per Pt atom for 1.1 nm Fe, $(0.53 \pm 0.10)\,\mu_B$ per Pt atom for 5.7 nm Fe, and $(0.45 \pm 0.10)\,\mu_B$ per Pt atom for 18.2 nm Fe. These results are also summarized in Tab. 4.2.

Within the uncertainty limits, the values are consistent with the magnetic moments derived for the Pt(x nm)/Fe(~ 10 nm) samples with varying Pt thicknesses, as presented in the previous sections. The derived magnetic moments do not show a considerable Fe thickness dependence, which would indicate a difference in the coupling between the Pt and the Fe layer. Even the thinnest Fe film of only 1.1 nm thickness generates a strong static MPE in the Pt. Thus, only the first couple of monolayers contribute to the interface coupling, while the bulk does not have a significant influence on the expansion of magnetization into the NM. Anal-

ogously to the results from the Pt thickness series, this is in agreement with the predictions for the static MPE.

4.2.6 FMM material dependence

Results from investigations on different Pt/FMM bilayer systems are presented in Fig. 4.9. Again, the XRR and XRMR data were collected at beamline P09, DESY at a photon energy of 11567.5 eV. Thus, for the XRMR evaluation a $\Delta\beta/\Delta\delta$ ratio of 3.4 was applied.

Here, $Ni_{33}Fe_{67}$, $Ni_{81}Fe_{19}$, and Ni were implemented as the FMM in addition to the already discussed Pt/Fe samples. For each layer combination the respective XRR scans are shown in Fig. 4.9(a), (c), and (e).

The film thicknesses of the FMMs are in the range of 8.3 nm to 9.8 nm, while the Pt layers exhibit thicknesses between 3.2 nm and 3.3 nm, as was derived from the XRR evaluation. The exact values for each heterostructure are shown in the insets of the XRR graphs. However, it has to be noted that fitting the experimental reflectivities for $Pt/Ni_{33}Fe_{67}$ and $Pt/Ni_{81}Fe_{19}$ with a full set of free structural and optical parameters does not yield reasonable results. In particular, the absorptive coefficients diverge in the fitting procedure. One possible reason for this is the angular resolution of the experimental data, which might not be sufficient to reproduce the reflectivity features correctly. This introduces an additional uncertainty to the data analysis. In order to gain more physically reasonable results, the optical parameters were fixed to the corresponding literature values from the Henke tables in the XRR analysis.

The XRMR asymmetry ratios are displayed in Fig. 4.9(b), (d), and (f). Both the $Pt/Ni_{33}Fe_{67}$ and the $Pt/Ni_{81}Fe_{19}$ sample show a finite amplitude in the asymmetry ratios (see Fig. 4.9(b) and (d)), implying a significant amount of spin polarized Pt. The corresponding magnetooptical profiles used for the asymmetry ratio simulations are shown in Fig. 4.9(g). The induced magnetic moments of the Pt as determined from the magnetooptical profiles are $m_{Pt/Ni_{33}Fe_{67}} = (0.44 \pm 0.10)\,\mu_B$ and $m_{Pt/Ni_{81}Fe_{19}} = (0.21 \pm 0.10)\,\mu_B$ per atom for Pt adjacent to $Ni_{33}Fe_{67}$ and $Ni_{81}Fe_{19}$, respectively.

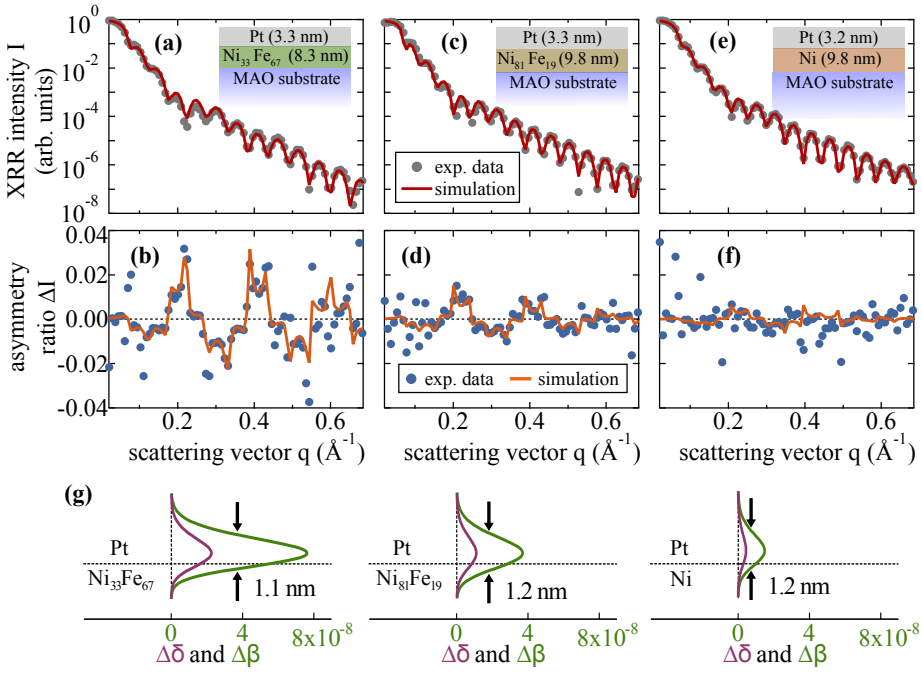

Fig. 4.9: XRR scans and XRMR asymmetry ratios for different Pt/FMM bilayer combinations. (a),(b) Pt/$Ni_{33}Fe_{67}$, (c),(d) Pt/$Ni_{81}Fe_{19}$, (e),(f) Pt/Ni. The corresponding magnetooptical profiles are displayed in (g).

The XRMR data on the Pt/Ni bilayer show only weak oscillations in the asymmetry ratio (Fig. 4.9(f)) corresponding to a moment of up to $(0.08 \pm 0.08)\,\mu_B$ per atom. In the Pt/Ni experiments the asymmetry ratio was recorded only once, which explains the comparatively small signal-to-noise ratio. Due to the small signal-to-noise ratio the simulation does not correspond to a curve fit, but was adjusted in order to obtain an upper limit for the Pt polarization. The respective magnetooptical profile is given in Fig. 4.9(g). In a previous work Wilhelm et al. have observed an induced moment of up to $0.29\,\mu_B$ in Pt/Ni multilayers with Pt thicknesses of only 2 monolayers [111] (see Fig. 2.12). This value is considerably larger than the limit found in our Pt/Ni bilayer. However, the data from Wilhelm et al. were recorded at 10K and are therefore likely to result in a

Tab. 4.3: Overview of induced magnetic moments derived from XRMR studies on Pt/FMM bilayers with different FMMs.

composition	Pt thickness (nm)	FM thickness (nm)	magnetic moment (μ_B per atom)
$Pt/Ni_{33}Fe_{67}$	3.3	8.3	0.44
$Pt/Ni_{81}Fe_{19}$	3.3	9.8	0.21
Pt/Ni	3.2	9.8	≤ 0.08

higher moment compared to RT measurements. The magnetic moments of the different Pt/FMM heterostructures are summarized in Tab. 4.3.

Additionally, Fig. 4.10 shows the induced Pt moment depending on the Fe content (red triangles). The induced spin polarization changes strongly with the amount of Fe in the FMM. Data for the magnetic bulk moments of various $Ni_{1-x}Fe_x$ compounds (reproduced from Ref. [167, 168]) show a comparable dependence on the Fe content x_{Fe}. Both the induced Pt moments and the bulk moments of the $Ni_{1-x}Fe_x$ compounds decrease significantly for decreasing Fe content in the FMM layer. The results presented suggest that the strength of the magnetic coupling between the two layers in terms of an induced spin polarization scales with the magnitude of the magnetic moment in the FMM. A similar result was found by Wilhelm et al. for Pt/Ni and Pt/Co [110] samples. The effective width of the spin polarized volume is in a range between 1.1 nm and 1.2 nm for the three samples. Thus, independently of the amplitude of the induced spin polarization, the penetration depth of the MPE does not vary considerably.

In general, it is well understood that static MPEs are mainly governed both by band hybridization at the interface between the NM and the FM and exchange interactions across the interface [54, 58]. However, Altbir et al. [169] stated that for a weak FM, i.e. a small splitting between the spin-up and spin-down bands, the expansion of the magnetization into the NM is very small even for the atomic layers closest to the interface. This

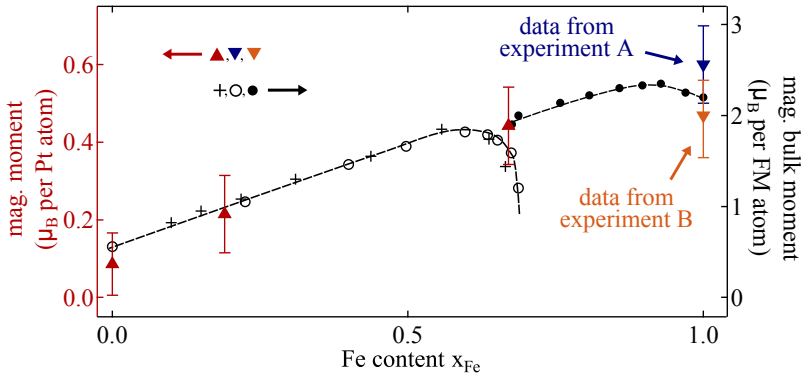

Fig. 4.10: Dependence of the Pt spin polarization on the Fe content in the underlying FMM (red triangles). The black circles and crosses are reproduced from Ref. [167,168] and display the magnetic bulk moment of $Ni_{1-x}Fe_x$. The solid circles [167] represent data for a crystallization in bcc structure and the open circles [167] and crosses [168] represent data from samples with fcc structure.

is consistent with a reduced Pt moment in Pt/Ni bilayers, as observed in this study. Nevertheless, a more detailed theoretical description of the underlying coupling mechanism in the investigated systems remains pending. Additional measurements on similar sample systems, e.g., $Co_{1-x}Fe_x$ hybrid structures, could also help in obtaining a more profound understanding of these correlations.

4.2.7 Pt on chemical vapor deposited $NiFe_2O_4$

In order to study the influence of static MPEs on Pt in contact to a ferromagnetic semiconductor or insulator, Pt/NFO bilayers were investigated with XRR and XRMR. The first NFO film was deposited by DLI-CVD on a (001) oriented MAO substrate, as outlined in section 3.1. A thin film of Pt was deposited on top of the stack in a subsequent sputter deposition. In between the deposition steps the vacuum was broken, therefore, slight contaminations of the interface cannot be excluded.

Resonant XRR and XRMR measurements were taken at beamline P09 at a photon energy of 11567.5 eV, as in the previous DESY studies. The XRR from Pt/NFO/MAO, as displayed in Fig. 4.11 (a), does not exhibit

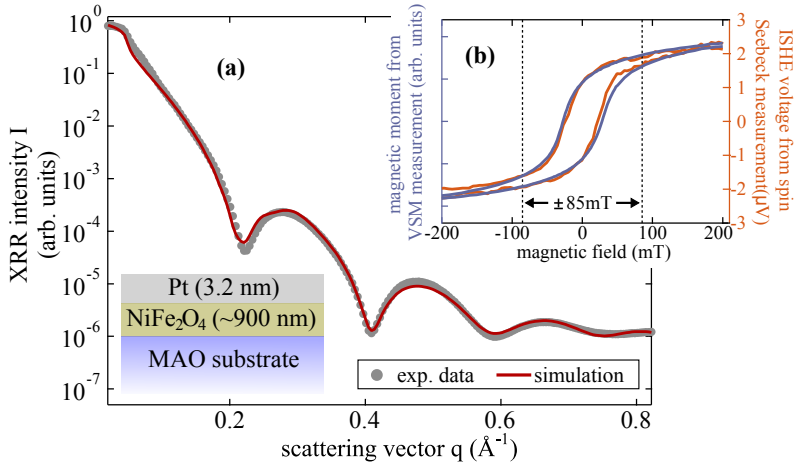

Fig. 4.11: (a) XRR intensity I and simulation for Pt on chemical vapor deposited NFO. Vibrating sample magnetometry (VSM) and LSSE measurements (ΔT= 18 K) for the Pt/NFO bilayer are displayed in the panel (b). The magnetic field of ±85 mT is marked by dashed lines and corresponds to the maximum field available in the XRMR studies.

oscillations corresponding to the NFO film, due to its large thickness of approximately $t_{\mathrm{NF0}} \approx 900$ nm. Determining the thickness and roughness of thick films (larger than 150 nm) via XRR is difficult since a large film thickness results in short period oscillations of the intensity, which might not be resolvable in XRR scans. The pronounced Kiessig fringes from the Pt layer, however, indicate a low roughness at both Pt interfaces. After all, the Kiessig oscillations of the intensity, generated from the Pt, are highly sensitive to the roughness on both sides of the Pt layer and are only visible if the two interfaces are very smooth. By fitting the intensity of the Kiessig fringes (Fig. 4.11 (a)) the Pt thickness can be determined to 3.2 nm while the roughness of the Pt/NFO and the air/Pt interfaces are 0.2 nm and 0.4 nm, respectively. Despite the large NFO film thickness, these values confirm smooth interfaces. In particular, the Pt/NFO interface roughness is of interest for the determination of a proximity induced Pt spin polarization. The roughness of the NFO/MAO interface is not accessible with this method due to the large film thickness of the NFO. However, simula-

tions of the XRR curve with a full heterostructure of Pt/NFO/MAO and with a single Pt film on an NFO substrate were carried out for different roughnesses at the NFO/MAO interface and the Pt/NFO interface, respectively, revealing that the reflectivity is influenced very weakly by the NFO/MAO interface roughness, while the Pt/NFO interface roughness has a large impact on the XRR [158]. Thus, the NFO/MAO interface can be neglected in the XRMR analysis and the NFO layer is treated as a substrate where only the surface is observable.

Since the chemical vapor deposited NFO films can exhibit variations in their properties, as discussed in section 3.1, it is imperative to study the physical properties, in particular the magnetic characteristics of each film, separately, prior to an experimental application. Therefore, VSM and LSSE measurements were performed on the film investigated in this experiment (see Fig. 4.11 (b)). The saturation magnetization can be derived from the VSM measurement and yields a value of about 244 kA/m, which corresponds to a moment of 1.9 μ_B/f.u. . The shape of the hysteresis loops reveal a magnetic moment in magnetic field direction of 70% saturation for magnetic fields of up to ± 85 mT, which is sufficient to observe dichroic effects.

From XAS studies (see Fig. 4.12), a whiteline intensity of about 1.39 for Pt/NFO can be obtained, which is somewhat larger than the value of 1.31 for Pt/Fe and the whiteline intensities reported by Geprägs et al. for Pt on YIG, which were lower than 1.30 [20, 21]. However, the value is still lower than the one found by Lu et al. [19] in Pt/YIG bilayers, which were also fabricated with a vacuum break in between the deposition steps. Their whiteline intensity can be determined to be 1.45 [21] which indicates partially oxidized Pt when compared to the value 1.50 for $PtO_{1.36}$ [164]. Thus, the Pt/NFO interface investigated here is more metallic than the films examined by Lu et al. but may still contain small amounts of partially oxidized Pt. It can only be speculated on the influence of a Pt oxidization at the interface. However, the observations of Lu et al. [19] imply that partial oxidization of the Pt does not necessarily suppress a static MPE, but might even enhance the effect.

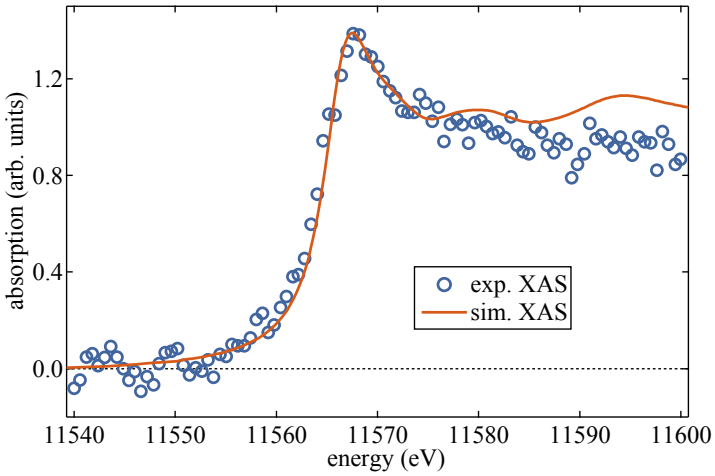

Fig. 4.12: Experimental absorption spectrum of Pt deposited on chemical vapor deposited NFO and theoretical absorption data for Pt from *ab initio* calculations. The theoretical spectrum was again shifted by 1.7 eV to higher energies and scaled in order to fit the experimental data.

In Fig. 4.13 XRMR measurements on Pt/NFO are shown. For comparison, the measured asymmetry ratio ΔI and a simulated asymmetry ratio are displayed in graph (b). Here, the magnetooptical profile of the spin polarization at a Pt/Fe interface (see Fig. 4.13(a)) was used for simulating a comparable spin polarization in the Pt/NFO sample. Note that the results from the evaluation of experiment A were used, assuming a magnetic moment of about $(0.61 \pm 0.10)\,\mu_B$ per Pt atom. Due to the different optical constants of NFO compared to Fe, the amplitude of ΔI would be larger for Pt/NFO compared to Pt/Fe using the same magnetooptical profile. The features obtained by this simulation are clearly absent in the experimental data, indicating that an induced spin polarization, if present, has to be considerably smaller.

In order to increase the sensitivity, the reflectivity was recorded in a range between $q = 0.2\,\text{Å}^{-1}$ and $q = 0.6\,\text{Å}^{-1}$ (two Kiessig fringes) and the average of 52 experiments was taken (see Fig. 4.13(c)). The averaged XRMR curve in Fig. 4.13(d) still shows a vanishing ΔI without any os-

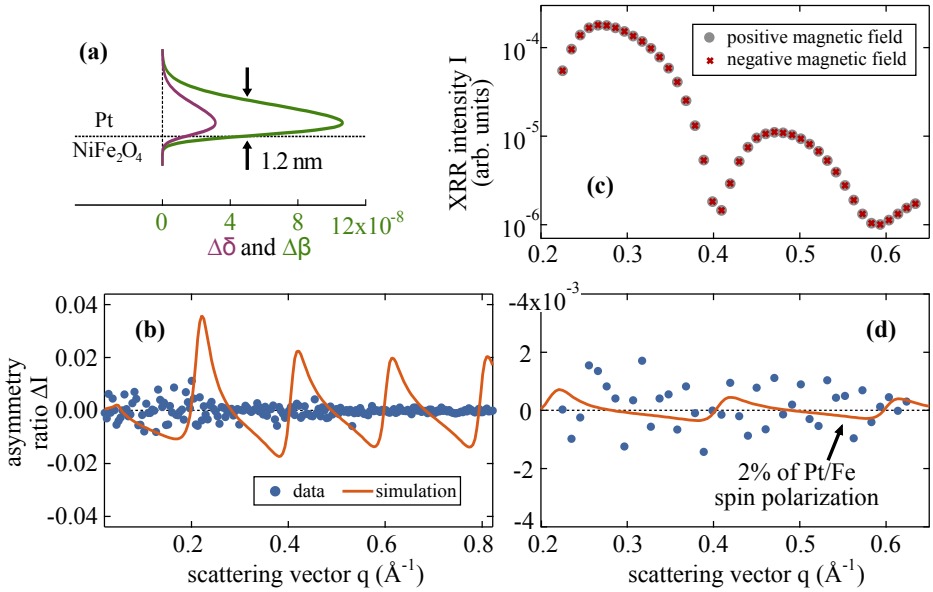

Fig. 4.13: XRMR intensity $I_{\pm}$ and corresponding asymmetry ratios ΔI for Pt(3.2 nm)/NFO($\sim$ 900 nm) (see XRR curve in Fig. 4.11(a)). (a) Magnetooptical profile used for the simulation in (b). (b) Asymmetry ratio ΔI (average of 8 curves). (c) XRMR intensity $I_{\pm}$ (average of 52 curves) for the reflectivity from $q = 0.2\,\text{Å}^{-1}$ up to $q = 0.6\,\text{Å}^{-1}$. (d) Asymmetry ratio ΔI from the XRMR in (c) and simulation assuming 2% of the Pt/Fe spin polarization.

cillations visible. A simulated asymmetry ratio assuming 2% of the Pt/Fe spin polarization leads to the lower detection limit and can be converted into a maximum magnetic moment in Pt on NFO of $0.02\,\mu_B$ per Pt atom using the Pt/Fe calibration and taking into account that NFO is only 70% magnetized for ± 85 mT (see. Fig. 4.11(b)). Therefore, a static MPE in Pt/NFO bilayers with chemical vapor deposited NFO can be neglected down to that limit. The absence of a static MPE in Pt/NFO samples is well in line with the results of Valvidares et al. on Pt/CFO bilayers [22]. They excluded an induced magnetic moment for Pt down to a limit of $0.002\,\mu_B$ per atom averaged over a 7 nm thick Pt layer. This value corresponds to a moment of about $0.01\,\mu_B$ per atom in a 1.2 nm thick spin polarized layer, similar to the limit given here. The good agreement is par-

ticularly consistent, since the two systems NFO and CFO both belong to the class of inverse spinel ferrites with insulating, ferrimagnetic character.

4.2.8 Pt on sputter deposited $NiFe_2O_4$

In addition to the studies on CVD NFO based heterostructures, the static MPE in Pt was also tested for samples with sputter deposited NFO films. The investigated film was sputtered at a substrate temperature of 610°C on (001) oriented MAO substrates, similarly to the process presented in section 3.2. Since the relatively small magnetic fields achievable with the applied four coil electromagnet at beamline P09 do not suffice to switch the magnetization of the thin sputter deposited NFO films, the examinations of the interfacial magnetic properties of Pt/NFO with sputter deposited NFO were carried out at beamline BM28, ESRF, with a field of ±200 mT. Thus, the resonant XRR and XRMR measurements on this system were taken at a photon energy of 11565 eV, while off-resonant XRR scans were performed at an energy of 11465 eV.

The magnetic properties in terms of the coercivity and the saturation field were checked by measuring the LSSE on the sample. The results are shown in Fig. 4.14. In graph (a), the ISHE voltage is plotted over the external field B for different out-of-plane temperature gradients. The amplitude of the ISHE voltage, i.e., of the LSSE scales linearly with the magnitude of the temperature difference across the sample (see Fig. 4.14(b)) and shows a sinusoidal dependence on the angle between the magnetic field and the voltage sensing (see Fig. 4.14(c)). The angle dependence is in line with the expected behavior for an ISHE and reflects the cross product of Eq. (2.13). The corresponding measurement geometry is sketched in the inset of Fig. 4.14(a). The sign of the effect is in agreement with previous LSSE measurements by Meier et al. [18, 23, 24, 170] on Pt/NFO bilayers with CVD prepared NFO and is in line with the sign convention proposed by Schreier et al. [171]. In the displayed loop measurements, the magnetic field range of ±200 mT is marked by dashed lines, which corresponds to the upper limit for the magnetic fields available in the setup at beamline BM28. This field value makes it possible to switch the mag-

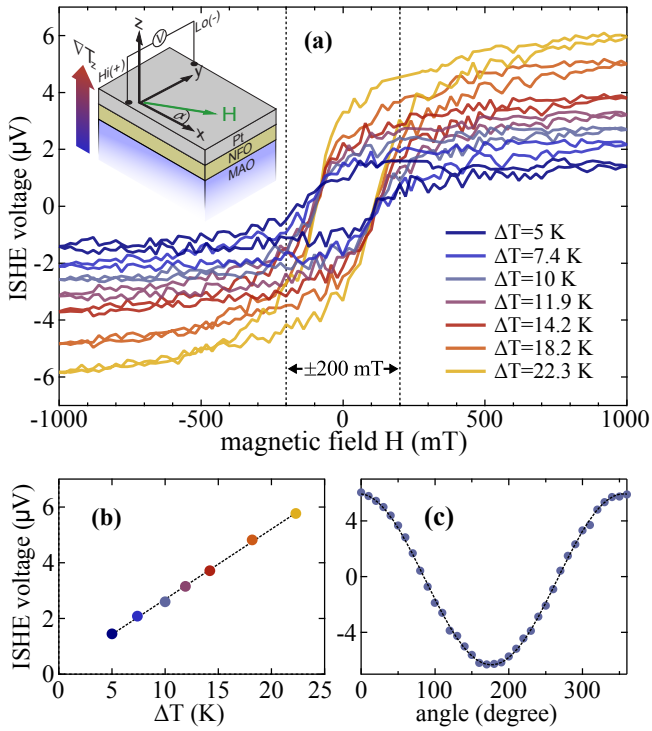

Fig. 4.14: LSSE measurements for Pt/NFO with sputter deposited NFO. (a) Magnetization loop for various temperature differences ΔT. Inset: Measurement geometry. (b) Saturation value of the ISHE voltage depending on ΔT. (c) Angular dependence of the ISHE voltage in magnetic saturation ($H = 1000\,\mathrm{mT}$, $\Delta T = 23\,\mathrm{K}$).

netization in the NFO film, however, it does not suffice to saturate the film completely. From the LSSE curves, the magnetization is estimated to reach about 70% saturation for ±200 mT, analogously to the XRMR experiment on the CVD NFO. From an AGM measurement the saturation magnetization is found to be 244 kA/m, i.e., 1.9 μ_B/f.u., like in the CVD NFO sample tested prior.

In order to obtain the structural and optical properties of the double layer, off-resonant and resonant non-magnetic XRR scans were collected without switching the external magnetic field. The resonant measure-

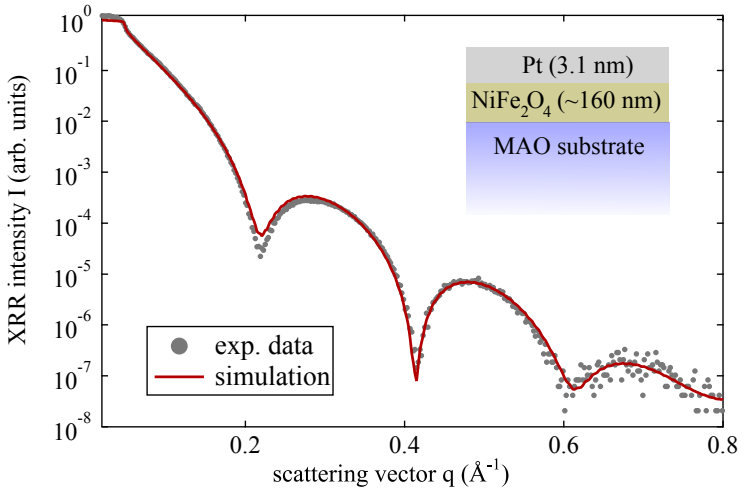

Fig. 4.15: XRR intensity I and simulation for Pt on sputter deposited NFO.

ment is displayed in Fig. 4.15 along with a simulation of the XRR curve. Again, the structural parameters were first fitted in the off-resonant curve and afterwards the resonant reflectivity was evaluated, in analogy to the procedure outlined in the previous chapters. The resulting structural parameters are given in the inset of Fig. 4.15. The Pt layer is 3.1 nm thick. For the NFO a thickness around 160 nm was estimated. However, this is only a rough extrapolation based on the thickness of a thinner sample, since the large NFO thickness does not show oscillations in the reflectivity data and, thus, hampers a more precise evaluation. Yet, despite the large NFO thickness the Pt layer exhibits smooth interfaces with low roughnesses of about 0.3 nm and 0.4 nm at the Pt/NFO and the air/Pt transition, respectively.

From the absorption spectrum displayed in Fig. 4.16 a whiteline intensity of about 1.35 can be determined. This value is slightly larger than in the Pt/Fe heterostructures, however, it is still smaller than the whiteline intensity obtained for the CVD NFO sample. Thus, the Pt exhibits a more metallic state when deposited directly on sputtered NFO without a vacuum break.

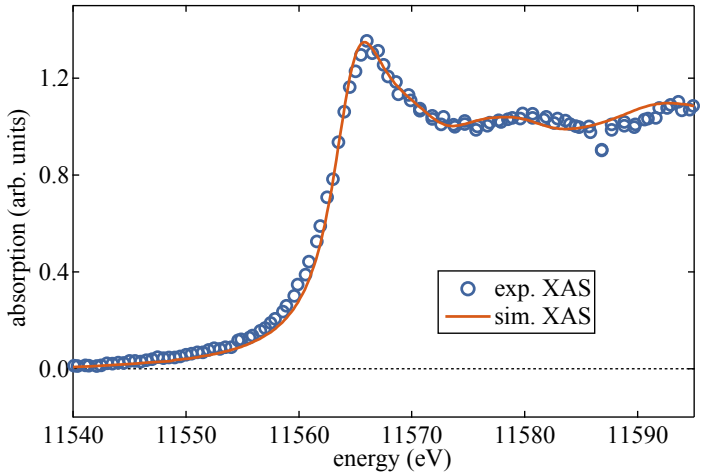

Fig. 4.16: Experimental absorption spectrum of Pt deposited on sputter deposited NFO and theoretical absorption data for Pt from *ab initio* calculations.

The subsequent XRMR measurements are presented in Fig. 4.17. The asymmetry ratio was monitored in a small range between $q = 0.04\,\text{Å}^{-1}$ and $q = 0.5\,\text{Å}^{-1}$, both for left- and right-handed photon helicity. Similar to the measurements on the CVD prepared NFO film in section 4.2.7, this region roughly spans two Kiessig fringes. Due to the comparatively low beam intensity at BM28, the noise level rapidly rises for larger scattering vectors and hinders the observation of small effects at larger q values.

4 curves were collected for each polarization. After inverting the sign of the curves taken with right handed helicity, the median of the 8 curves was calculated. This method was chosen here over the arithmetic mean, in order to exclude large outliers from the evaluation, which were present in the raw data due to computational errors during the data acquisition. The resulting experimental asymmetry ratio is plotted in Fig. 4.17. Graph (a) shows the asymmetry ratio along with a simulation for a magnetooptical profile equivalent to the one derived for the Pt(3.3 nm)/Fe(5.7 nm) sample from the Fe thickness series, as presented in section 4.2.5 (see inset of Fig. 4.17(a)). This profile was chosen for the simulation, as the measuring setup and the photon energy were identical in both experiments.

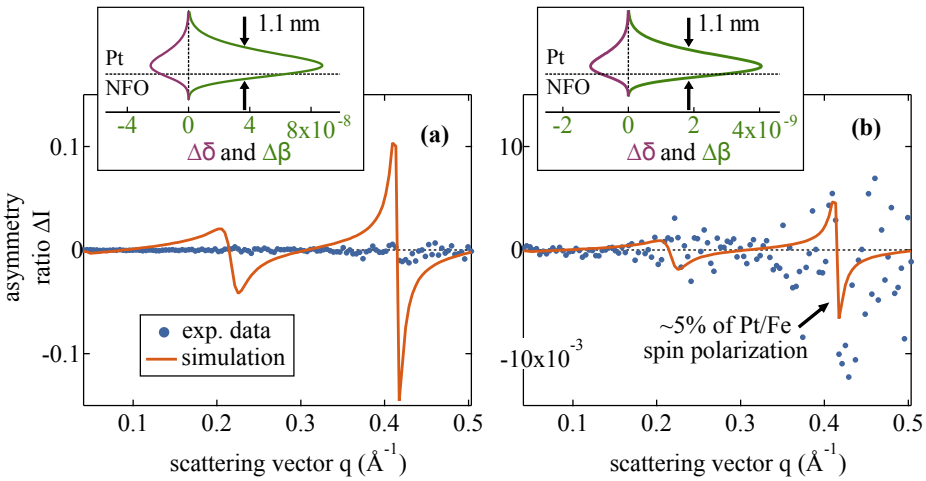

Fig. 4.17: Asymmetry ratio ΔI (median of 8 curves) for Pt on sputter deposited NFO. (a) displays the asymmetry ratio and a simulation equivalent to an induced spin polarization as found for the Pt(3.3 nm)/Fe(5.7 nm) bilayer discussed in section 4.2.5. The corresponding magnetooptical profile is shown in the inset of (a). A close-up of the asymmetry ratio ΔI with a simulation assuming 5% of the Pt/Fe spin polarization is presented in (b). The corresponding magnetooptical profile is sketched in the inset of (b).

Thus, the $\Delta\beta/\Delta\delta$ ratio was fixed at -3.5, according to the photon energy and the previously determined position of the maximal dichroism (see Fig. 4.8).

The applied magnetooptical profile yields a very large asymmetry ratio of more than 10% that should occur if the Pt has an induced magnetic moment of about $0.61\,\mu_B$ per atom. This value is much larger than the asymmetry ratio observed in the Pt(3.3 nm)/Fe(5.7 nm) sample and also far exceeds the simulations carried out for the previous CVD NFO based bilayer. The large differences in the effect amplitude between the heterostructures with sputter deposited and with chemical vapor deposited NFO can mainly be attributed to the different roughnesses at the Pt/NFO interface. As discussed in section 4.2.3, the roughness at the Pt/FM interface can have a large impact on the XRMR amplitude. Here a certain combination of structural and optical parameters induces the large fea-

tures around $q = 0.4\,\text{Å}^{-1}$. Even slight changes in the values of roughness and optical parameters can reduce the magnitude of these extrema rapidly, while the features around $q = 0.2\,\text{Å}^{-1}$ remain almost unaffected.

However, the large oscillations visible in the simulation are clearly not present in the experimental data, indicating that the static MPE, if present, is much smaller in this system. This is well in line with the findings for Pt on CVD NFO. Decreasing the magnitude of the magnetooptical parameters to about 5% of the Pt/Fe profile results in a more reasonable simulation of the observed asymmetry ratio, as displayed in Fig. 4.17(b) and the corresponding inset.

The increased noise around $q = 0.2\,\text{Å}^{-1}$ and $q = 0.4\,\text{Å}^{-1}$ originates from the drop in intensity at the minima of the Kiessig fringes in the reflectivity curve (see Fig. 4.15) and does not necessarily imply the presence of the features visible in the simulated XRMR asymmetry ratio. However, the large noise obscures a potential magnetic response and causes the upper limit for the observed effect displayed in the graph.

Taking into account the degree of circular polarization of the synchrotron radiation and the partial magnetic saturation of the NFO layer, this upper limit corresponds to a magnetic moment of $0.04\,\mu_\text{B}$ per Pt atom in a 1.1 nm thick spin polarized volume. Up to this limit a static MPE can be excluded for Pt on sputter deposited NFO. Due to the lower sensitivity in this experiment, this value is slightly larger than the value found for the chemical vapor deposited NFO. However, the absence of a static MPE is in good agreement with the prior results for CVD NFO and the report on Pt/CFO films [22]

4.2.9 XRMR on Pt/YIG

In the course of investigations on Pt/FMI heterostructures also Pt/YIG double layer systems have been examined. YIG is one of the most frequently used FMIs in spin caloritronic applications. Thus, the interface properties of Pt/YIG bilayers are particularly important for research progress in this field. Previous XMCD investigations on Pt/YIG heterostructures have caused some controversy, since different studies gener-

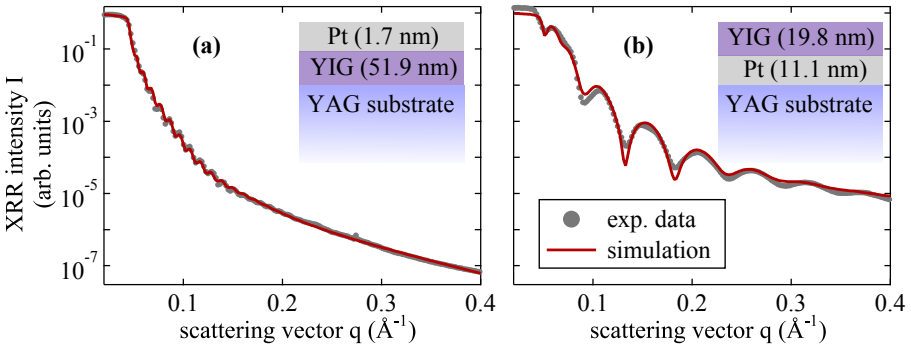

Fig. 4.18: XRR curves for (a) Pt(1.7 nm)/YIG(51.9 nm) and (b) an inverted layer stack with YIG(19.8 nm)/Pt(11.1 nm). The structure is sketched in the respective insets.

ated contradictory results [19–21]. Therefore, additional XRMR experiments were carried out on YIG based heterostructures at beamline I16, Diamond Light Source. The resonant curves were taken at a photon energy of 11567 eV with left handed photon helicity. A magnetic field of ±85 mT was again realized by a four coil electromagnet.

The Pt/YIG films investigated were provided by Stephan Geprägs and Matthias Opel from the Walther-Meißner-Institute in Garching and were fabricated by pulsed laser deposition similar to the samples in Refs. [20] and [21]. Two different hybrid structures were tested for an induced spin polarization in the Pt. Both samples are deposited on (111) oriented $Y_3Al_5O_{12}$ (YAG) substrates. The Pt/YIG sample from Ref. [21] was investigated with XRMR, in addition to the XMCD studies by Geprägs et al. [20, 21]. Apart from this, an inverted structure, i.e., a YIG/Pt/YAG heterostructure with reversed layer sequence, was examined.

The exact layer sequences and the corresponding film thicknesses are displayed in the insets of Fig. 4.18 (a) and (b), along with the respective resonant XRR curves. In graph (a) XRR from the Pt/YIG heterostructure is displayed. The Pt layer is found to be about 1.7 nm and the YIG film is about 51.9 nm thick. The roughnesses of the YIG/YAG interface and the Pt surface, as determined from the XRR curve, are very large

with 1.7 nm and 1.5 nm, respectively. The large roughnesses are mainly responsible for the steep drop of the XRR intensity and the fast decay of the Kiessig oscillations. It has to be noted that, since the features in the reflectivity are not very pronounced, a precise evaluation of the exact structural and optical parameters is challenging. Therefore, the derived values may contain uncertainties. However, the Pt roughness is in the same range as the Pt film thickness. Thus, the Pt does not correspond to a closed layer as indicated in the inset of Fig. 4.18(a), but more likely exhibits island growth on top of the YIG film. In the simulation model this manifests itself in the absence of a plateau in the optical profile. Instead it exhibits a gradual transition from YIG to Pt and from Pt to air. Still the model suffices to describe the system and reproduces the reflectivity data well. The Pt/YIG interface, however, is very smooth and exhibits a low roughness of only 0.2 nm. This is surprising, considering the large YAG roughness.

Graph (b) shows an XRR scan of the inverted structure (YIG/Pt). Here, the YIG film is about 19.8 nm on top of a 11.1 nm thick Pt layer. The YIG/Pt interface exhibits a comparatively large roughness of 0.9 nm.

XA spectra of both samples are displayed in Fig. 4.19(a) (Pt(1.7 nm)/YIG(51.9 nm)) and (b) (YIG(19.8 nm)/Pt(11.1 nm)). The conventional double layer stack exhibits a large whiteline intensity of about 1.5, which complies with the value found by Kolobov et al. for partially oxidized Pt [164]. The inverted structure shows a much smaller whiteline of about 1.25, in line with completely metallic Pt. The simulations from *ab initio* calculations have to be shifted by 2.5 eV to higher energies to fit the experimental data. This results in a $\Delta\beta/\Delta\delta$ ratio of 7.3 for the evaluation of the XRMR data.

XRMR asymmetry ratios and the corresponding simulations are depicted in Fig. 4.20. Graph (a) illustrates the magnetic response from the conventional stack (Pt/YIG). The displayed asymmetry ratio was averaged from 5 curves. The magnetooptical profile used for the simulation is shown in the inset. The thickness of 1.3 nm for the spin polarized Pt corresponds to almost the whole Pt volume. The small Pt thickness re-

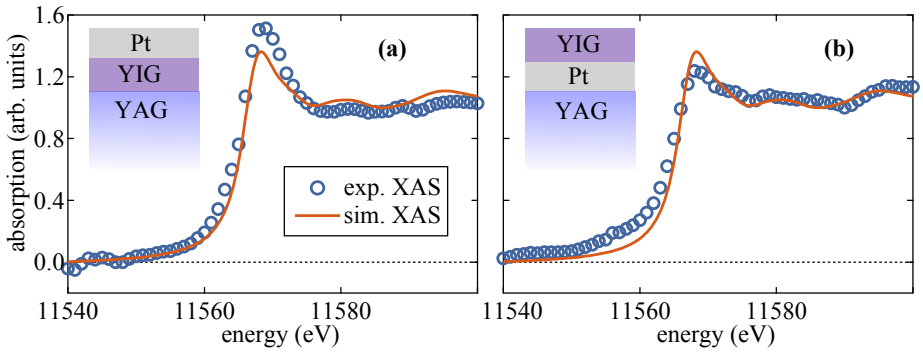

Fig. 4.19: Absorption spectra for (a) Pt(1.7 nm)/YIG(51.9 nm) and (b) the inverted YIG(19.8 nm)/Pt(11.1 nm) layer stack.

sults in only one minimum in the investigated q interval. However, the simulated feature is clearly not observable in the experimental data, thus, the applied magnetooptical profile represents an upper limit for a possible static MPE. The resulting maximum magnetic moment is only $0.002\,\mu_B$ per Pt atom. Note that the noise level is extremely low in this setup, enabling highly sensitive measurements and a very precise evaluation of the data. Geprägs et al. reported an upper limit of $0.003\,\mu_B$ per Pt atom in a 3 nm thick Pt film on YIG [21]. Assuming, that the polarized Pt is located in a 1.2 nm thick layer, this yields a maximum magnetic moment of $0.003\,\mu_B \cdot (3\,\text{nm}/1.2\,\text{nm}) \approx 0.007\,\mu_B$ per atom in the effective spin polarized volume. Therefore, the high sensitivity of XRMR at beamline I16 allows to decrease this limit by a factor of more than 3.

The experimental data from the inverted structure (YIG/Pt) is averaged over 8 curves and plotted in 4.20 (b). The graph clearly exhibits a pronounced oscillation corresponding to an induced spin polarization at the YIG/Pt interface. The data can be simulated using the magnetooptical profile from the inset. However, while the oscillation from the magnetized Pt is reproduced well, some systematic deviations between the simulation and the asymmetry ratio are apparent.

The discrepancies between simulation and experiment imply that the asymmetry ratio contains an additional contribution which is not repro-

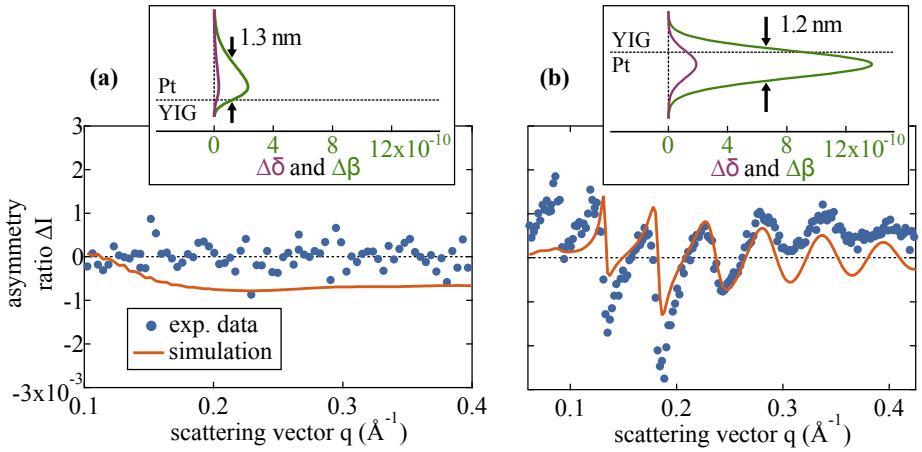

Fig. 4.20: Asymmetry ratio ΔI for (a) Pt deposited on top of a YIG layer (average of 5 curves) and (b) an inverted structure with YIG deposited on top of a Pt layer (average of 8 curves). The respective magnetooptical profiles used to simulate the scans are shown in the insets.

duced well within the applied model. A Fourier analysis is applied to the raw data, in order to identify the dominating frequencies. In particular, a constant offset ($f = 0$), as well as some long period oscillations ($f = 1$, $f = 2$, and $f = 3$ corresponding to 1, 2, and 3 oscillation periods in the considered interval, respectively), which do not correspond to the Kiessig fringes from the Pt or the YIG layer, show large Fourier coefficients. Subtraction of a background, generated from these frequencies, enables a much better simulation of the experimental data, as shown in Fig. 4.21(c). The subtracted background is illustrated in graph (a) of Fig. 4.21 and the corresponding Fourier spectrum is shown in panel (b).

However, the origin of this background is unclear and leaves room for speculation. In particular, it remains to be clarified whether an additional interlayer with a small thickness, e.g., a thin oxide layer at the interface, could generate the observed long period oscillation. The good agreement between the simulation and the corrected data within the applied XRMR model however indicates that the background might not correspond to a magnetic response, but possibly stems from non-magnetic effects. Yet, ad-

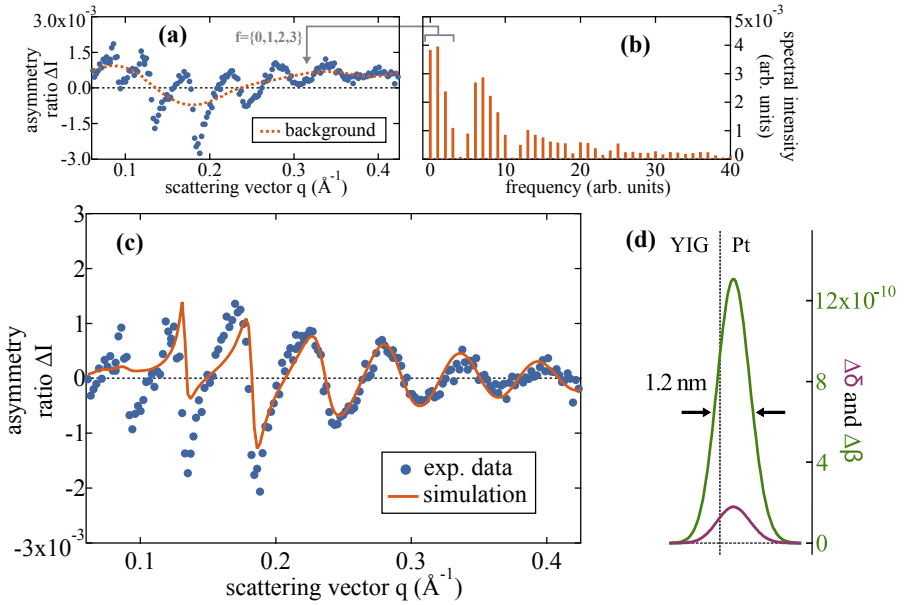

Fig. 4.21: (a) illustrates the subtracted background as derived from the back transformation of the Fourier transformed for frequencies $f = 0$, $f = 1$, $f = 2$, and $f = 3$, while (b) displays the corresponding Fourier spectrum. (c) shows the background corrected XRMR curve of the inverted structure along with a simulation of the asymmetry ratio. The corresponding magnetooptical profile is displayed in (d).

ditional XRMR measurements for opposite photon helicities are required to clarify this assertion with more certainty. Unfortunately, the studies on Pt/YIG bilayers have only been carried out for one photon polarization so far.

While the background corrected asymmetry ratio is reproduced well in the XRMR evaluation, i.e., much better than the raw curve, the resulting magnetooptical profiles differ only slightly. Thus, the application of a background subtraction yields a better fit, but does not considerably modify the outcome for the magnetic moment. Considering the degree of circular polarization at beamline I16, an induced magnetic moment of about $(0.008 \pm 0.002)\,\mu_B$ per Pt atom in a 1.2 nm wide spin polarized volume can be derived from the magnetooptical parameters

(see Fig. 4.21(d)). Assuming that the spin polarized Pt observed by Lu et al. [19] in a Pt(1.5 nm)/YIG bilayer using XMCD is also located in a 1.2 nm thick layer, one obtains an effective magnetic moment of $0.054\,\mu_B \cdot (1.5\,\text{nm}/1.2\,\text{nm}) \approx 0.068\,\mu_B$ per Pt atom in the spin polarized volume for their sample. This value is one order of magnitude larger than the moment found in this study for the inverted YIG/Pt structure.

The appearence of a static MPE is most likely due to an intermixing of Pt and YIG at the interface. In particular, the high deposition temperature of 500°C of the YIG layer on top of the Pt can contribute to the intermixing. This assumption is also supported by the comparatively large YIG/Pt interface roughness of 0.9 nm, found in the XRR evaluation. The strong intermixing potentially leads to a large amount of direct Pt-Fe neighbors, i.e., an increased hybridization between states from Fe atoms in the YIG film to interface states of the Pt atoms inducing the observed spin polarization. However, while a more detailed investigation of the exact interface coupling in these samples is pending, the results clearly suggest that the static MPE is highly sensitive not only to the material combination, but in particular to the interface properties, e.g., the roughness, which can possibly alter the interfacial bandstructure and introduce magnetic states around the Fermi level coupling to NM states. Therefore, carefully controlling the preparation conditions is imperative in order to gain samples suitable for spin caloritronic applications.

4.3 Conclusion

The technique of XRMR was applied as a very sensitive tool to investigate induced spin polarizations in terms of static MPEs in different Pt/FM bilayers. XRMR asymmetry ratios were quantitatively analyzed by fitting the magnetooptical parameters and comparing the experimental findings with *ab initio* calculations in order to determine the induced magnetic moment. Different magnetooptical profiles were applied to the asymmetry ratio of a Pt/Fe bilayer and evaluated in order to find the best fitting model. A convolution of a Gaussian shaped profile with the interface

roughness was found to yield the best results and was used for the analysis of the XRMR curves.

The energy dependence of the magnetic response was investigated by taking XRMR measurements at varying photon energies. Optical data from *ab initio* calculations are reproduced well by the experimentally derived magnetooptical parameters. From scaling the simulation to the observed values the magnetic moment per Pt atom was extracted. Deviations between two measurements on the same sample at different times were studied in detail by variation of different fit parameters. It was found that a precise knowledge of the structural and optical parameters is required for an accurate evaluation of the XRMR data. Therefore, for an optimum analysis of the XRR and XRMR scans and an exact determination of the interfacial spin polarization in heterostructures, it is convenient to rely on off-resonant XRR measurements for a first assessment of the structural parameters far from the absorption edge. Using these values as an input for the resonant XRR and the subsequent XRMR analysis enables a most precise assessment of the magnetic moments induced in the NM.

In the course of this work, most experiments were only performed at the resonance, introducing some uncertainties in the determination of the fit parameters and the resulting magnetic moments. However, the observed differences in the experimental values for the Pt/Fe system cannot be explained completely by uncertainties in the fitting procedure, which gives rise to the assumption that the sample had experienced a structural transformation in the interval between the two experiments.

Results for different Pt thicknesses on ferromagnetic Fe films demonstrate that XRMR is only sensitive to the spin polarization at the Pt/FM interface, independently of the Pt thickness. This film thickness independence is highly beneficial for the investigation of interface spin polarizations and endorses the use of XRMR in addition to the conventional XMCD for interface studies.

In addition, the FM thickness dependence of the static MPE was tested using XRMR on a series of Pt/Fe bilayers with different Fe thicknesses. No differences in the effect amplitude were observed within the investigated

Fe thickness range between 1.1 nm and 18.2 nm, which proves that the static MPE is solely an interface effect and does not depend on the whole film volume of the FM.

Additionally, samples with different FMM layers were studied. A strong correlation between the Pt spin polarization and the Fe content of the adjacent ferromagnet in Pt/Fe, Pt/$Ni_{33}Fe_{67}$, Pt/$Ni_{81}Fe_{19}$, and Pt/Ni bilayers was found. In particular, a significant reduction of the magnetic moment of Pt in proximity to Ni with respect to Pt/Fe bilayers was observed. A comparison with bulk magnetic moments for the different FMM compositions implies a correlation between the static MPE and the magnetization of the FM. However, the real origin of the differences in strength of the magnetic coupling has to be examined in more detail for an accurate explanation. An additional series with Co-Fe based FMM layers in proximity to Pt could yield a better understanding of these correlations and should be considered in future investigations.

Investigations of Pt/FMI double layers were carried out on different Pt/NFO and Pt/YIG or YIG/Pt samples, respectively. The Pt/NFO samples with both chemical vapor and sputter deposited NFO films do not show any evidence for an induced spin polarization. Therefore, a static MPE can be excluded in both heterostructures down to a limit of $0.02\,\mu_B$ per Pt atom and $0.04\,\mu_B$ per Pt atom, respectively, in an effective Pt thickness of about 1.1 nm - 1.2 nm around the interface.

Similarly, a Pt spin polarization can be excluded down to a limit of $0.002\,\mu_B$ per Pt atom in a Pt/YIG hybrid structure. The significant reduction of the upper limit for the potential spin polarization with respect to the Pt/NFO values is owed to the high sensitivity in the employed setup. The absence of a static MPE in Pt/NFO and Pt/YIG is well in line with the predicted behavior of NM/FMI bilayers in general, since the lack of states around the Fermi level should prohibit an interfacial coupling of states between the two materials involved. Also, the results are in good agreement with the findings of Geprägs et al. in Pt/YIG bilayers [20, 21] and Valvidares et al. in Pt/CFO hybrids [22]. Yet, this contradicts the observations of Lu et al., who found a spin polarization in Pt on YIG [19].

Tab. 4.4: Overview of induced magnetic moments derived from XRMR studies on different Pt/FM and FM/Pt sample systems.

composition	Pt thickness (nm)	FM thickness (nm)	magnetic moment (μ_B per atom)
Pt/Fe	1.8	9.7	0.42
	3.4	9.2	0.61 (exp. A)
			0.46 (exp. B)
	5.8	10.0	0.48
	20.0	9.8	0.44
	3.4	1.1	0.53
	3.3	5.7	0.53
	3.2	18.2	0.45
$Pt/Ni_{33}Fe_{67}$	3.3	8.3	0.44
$Pt/Ni_{81}Fe_{19}$	3.3	9.8	0.21
Pt/Ni	3.2	9.8	≤ 0.08
Pt/NFO(CVD)	3.2	~ 900	≤ 0.02
Pt/NFO(sputt.)	3.1	~ 160	≤ 0.04
Pt/YIG	1.7	51.9	≤ 0.002
YIG/Pt	11.1	19.8	0.008

Studies of an inverted layer stack, i.e., a YIG/Pt structure where YIG was subsequently deposited on the Pt, show a distinct magnetic response in the XRMR asymmetry ratio. The evaluation yields a magnetic moment of $(0.008 \pm 0.002)\,\mu_B$ per Pt atom in a 1.2 nm wide effective spin polarized volume. It is assumed that the induced spin polarization can be attributed to the increased interface roughness, corresponding to an intermixing of

the layers, which might introduce interfacial Fe states around the Fermi level. This potentially results in a substantial amount of Pt-Fe nearest neighbor coupling, inducing magnetic proximity. Therefore, it is evident that the interface configuration can strongly affect the occurence of a static MPE, even in Pt/FMI bilayers. Yet, it has to be noted that the observed value is far below the upper limits estimated for the Pt/NFO bilayers. Thus, the noise level in the experiments performed on Pt/NFO samples could be concealing an effect of that order as well. However, the induced magnetic moment is very small and it is questionable if such a small moment can induce substantial parasitic contributions in spin caloritronic experiments which obscure the investigated effects significantly. Detailed theoretical and experimental studies have to be conducted in order to clarify this aspect. An overview of all magnetic moments and the respective upper limits observed in the Pt/FM heterostructures is presented in Tab. 4.4.

5 Spin Hall magnetoresistance in $Pt/NiFe_2O_4$ bilayers

In this chapter first experiments on non-equilibrium MPEs in terms of the SMR in sputter deposited Pt/NFO bilayers are presented. In particular, rotational measurements were carried out in order to separate SMR and other MR contributions. Besides the detailed evaluation of the SMR, the origin of an additional AMR like effect in the films studied is investigated within different measurements. The measurements and evaluations in this chapter were performed in cooperation with Konstantinos Kontotolis, who was working on the SMR in Pt/NFO during his master's thesis and with Panagiota Bougiatioti who is currently working as a PhD student in this field. Some of the results can also be found in K. Kontotolis' master's thesis [172].

5.1 Experimental details

All Pt/NFO bilayers investigated in this chapter were fabricated by sputter deposition on (001) oriented MAO substrates, analogous to the films in section 3.2.2 and in section 4.2.8. In particular, the sample from section 4.2.8 was investigated here amongst others. Consequently, the NFO thicknesses correspond to the samples in the previous chapters, i.e., some of the layers are in the range of about 58 nm, while one sample exhibits a thickness of about 160 nm. In a subsequent procedure Pt was deposited on top of the NFO films by dc sputter deposition at ambient temperature without breaking the vacuum between the processes. The Pt layers are all in the range of about 3 nm. Althammer et al. have shown that the SMR

in Pt on top of an FMI exhibits a maximum for Pt thicknesses around 3 nm [12], therefore this value was chosen for the experiments presented here. The Pt/NFO interfaces were smooth with roughnesses in the range of about 0.3 nm to 0.4 nm. For electrical measurements the samples were patterned into a Hall-bar geometry with a length of 1000 μm and a width of 75 μm via optical lithography, identical to the one described in Ref. [12]. The longitudinal resistivity was measured using a 4-point probe technique. The input current was constant at 100 μA and the voltage was collected. Magnetic fields of up to 1 T were available and could be rotated. Temperature dependent measurements of the resistivity down to 20 K were performed in a He-cooled cryostat.

The most efficient way to distinguish between an AMR, either from the FM or from an induced spin polarization in terms of a static MPE and the SMR, is by performing resistivity measurements on the Pt strip, while the magnetization is rotated around different axes. As detailed in section 2.3.2, the AMR and the SMR show a different angle dependence of the FM magnetization and can thus be distinguished by measuring the longitudinal resistivity of the Pt strip for both an oopj and an oopt geometry (see Eqs. (2.2) and (2.16) and Fig. 2.8). Since the SMR and the AMR cannot be distinguished by rotating the magnetic field in-plane, only out-of-plane curves are presented here. Furthermore, only measurements of the longitudinal resistivity ρ_{long} are considered, since the transversal resistivity exhibits the same behavior for SMR and AMR.

5.2 Results and discussion

First rotational measurements in oopj and oopt geometry carried out on the Pt(3 nm)/NFO(160 nm) bilayer are shown in Fig. 5.1 (a) and (b). The measurement geometries are depicted in the insets of graphs (a) and (b). The rotated magnetic field was 1 T in this experiment. From the theory of the SMR the resistivity is expected to change with the direction of the magnetization in the oopj geometry, while no effect should be visible in the oopt rotation (see Fig. 2.9(b) and (c)). Note that here the different

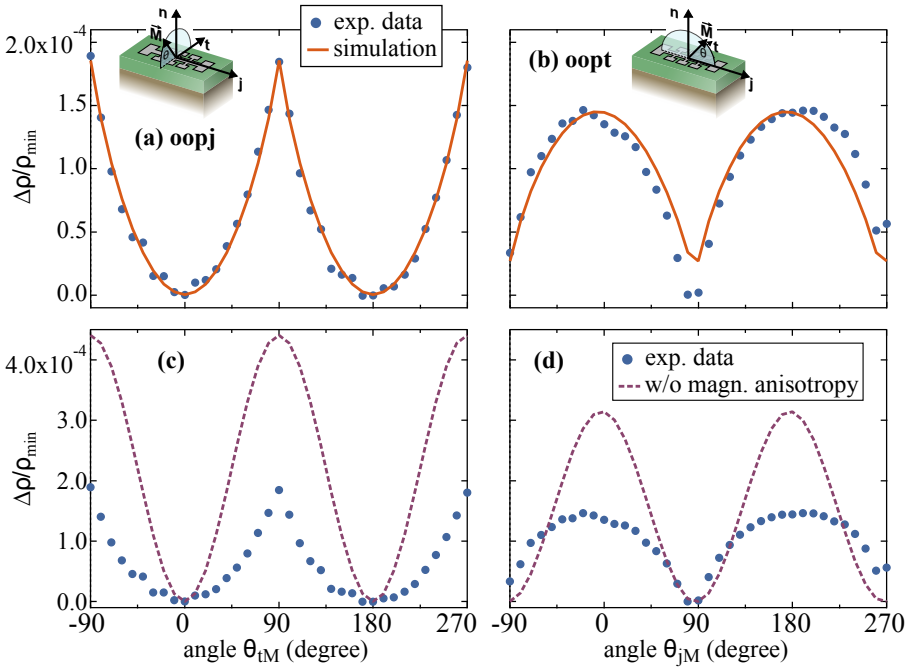

Fig. 5.1: Resistivity measurements with rotating magnetic fields in (a),(c) oopj and (b),(d) oopt geometry, as sketched in the respective insets. The curves in (a) and (b) are fitted using different models based on the SMR and the AMR, respectively, considering magnetic shape anisotropy with magnetic hard axis out-of-plane. (c) and (d) display simulations of the effects for oopj and oopt geometry in the absence of a magnetic anisotropy.

MRs are displayed in the ratio $\Delta\rho/\rho_{\mathrm{min}} = \frac{\rho-\rho_{\mathrm{min}}}{\rho_{\mathrm{min}}}$ in order to enable a comprehensive comparison of the SMR and other MR contributions. The absolute MRs amplitude are defined via $\Delta\rho_{\mathrm{abs}}/\rho_{\mathrm{min}} = \frac{\rho_{\mathrm{max}}-\rho_{\mathrm{min}}}{\rho_{\mathrm{min}}}$. This differs slightly from the definition of the SMR magnitude in Eq. (2.19), which is given by $-\rho_1/\rho_0 = \frac{\rho_{\mathrm{max}}-\rho_{\mathrm{min}}}{\rho_{\mathrm{max}}}$. However, the difference between these two values is an order below the significant digits considered here and can be neglected.

The experimental data from the oopj rotation is consistent with the expected $\cos(\theta_{\mathrm{tM}})^2$ signature, therefore, we attribute the observed effect in the oopj direction to an SMR. However, in the oopt geometry an MR

effect is visible as well, which is of the same order of magnitude as the SMR and shows the characteristics of an AMR, i.e., a pronounced $\cos(\theta_{\mathrm{jM}})^2$ behavior.

In order to get an estimate of the total effect amplitudes of the two effects, the absolute elevation between the maximum and the minimum values of the resistivity have to be calculated. However, the applied field of 1 T does not suffice to saturate the magnetization in the out-of-plane direction completely. This yields a strong deviation from the regular sinusoidal shape and results in sharp peaks in the experimental curves around 0° and 180°. A similar behaviour was observed by Valvidares et al. in Pt/CFO heterostructures for external magnetic fields of up to 9 T [22]. On the assumption that the films exhibit a pronounced magnetic shape anisotropy pulling the magnetization into the film plane, the curves can be fitted using the SMR and an AMR model based on Eq. (2.17) and Eq. (2.4), respectively, by including a uniaxial magnetic anisotropy (outlined in section 2.3.2). Strictly speaking, Eq. (2.4) is valid only for a polycrystalline film while our Pt layers show a high (111) texture. Therefore, the AMR model was adjusted for a (111) orientation according to the approach by Limmer et al. [76] (see Eq. (2.20)). Here it is assumed that the films can be saturated in the in-plane direction, however, the LSSE curves from Fig. 4.14 imply that the films are not fully saturated in-plane for a magnetic field of 1 T. Yet, considering the very strong magnetic shape anisotropy in the NFO thin films compared to the slight reduction of the in-plane magnetization, this approach yields a reasonable approximation.

The fitted curves are displayed in Fig. 5.1 (a) and (b). The SMR fit reproduces the experimental data very well. The fit based on the AMR model shows some deviations, but still describes the shape of the curve quite well. Taking into account a reduction of the effective magnetization in the out-of-plane direction due to the observed magnetic anisotropy, we find a corrected SMR amplitude of $\Delta\rho_{\mathrm{abs}}/\rho_{\mathrm{min}} = 4.4 \cdot 10^{-4}$, which is of the same order as the value $2.7 \cdot 10^{-4}$ reported by Althammer et al. for Pt/NFO structures with chemical vapor deposited NFO and a 10 nm thick

Pt layer [12]. The slightly enhanced magnitude in our samples compared to their films is in line with the different Pt film thicknesses.

The oopt rotation exhibits a corrected MR amplitude of $\Delta\rho_{\mathrm{abs}}/\rho_{\mathrm{min}} = 3.1 \cdot 10^{-4}$, which is of the same order as the SMR. The origin of this magnetoresistance is not evident and cannot be explained within the established SMR model; thus, different measurements are carried out in order to find a plausible explanation for the observations. In particular, it has to be clarified, whether the effect is associated with an AMR. The anisotropy corrected curves are illustrated in Fig. 5.1 (c) and (d).

The spin mixing conductance G_{r} can be determined from the corrected SMR magnitude and estimations of the spin diffusion length λ_{Pt} and the spin Hall angle α_{SH} of Pt. Althammer et al. derived values for λ_{Pt} and α_{SH} from a series of Pt/YIG bilayers with different Pt thicknesses by fitting the thickness dependent SMR magnitudes with the model from Eq. (2.19) for different values of G_{r}. They found the best agreement between experiment and model for $G_{\mathrm{r}} = 4 \cdot 10^{14}\,\Omega^{-1}\mathrm{m}^{-2}$, $\lambda_{\mathrm{Pt}} = 1.5\,\mathrm{nm}$, and $\alpha_{\mathrm{SH}} = 0.11$. Applying these values for λ_{Pt} and α_{SH} to Eq. (2.19) along with the specific characteristics of the Pt layer tested ($t_{\mathrm{Pt}} \approx 3\,\mathrm{nm}$, $\rho_{\mathrm{Pt}} \approx 1.6 \cdot 10^{-7}\,\Omega\mathrm{m}$) we find a value of $G_{\mathrm{r}} = 3.1 \cdot 10^{14}\,\Omega^{-1}\mathrm{m}^{-2}$, which is slightly lower than Althammer's approximation. Note that literature values for the spin diffusion length and the spin Hall angle of Pt are scattered over a large range. In particular, the spin Hall angle of 11% is comparatively large considering other publications. A comprehensive overview on current literature addressing this aspect is given in Ref. [95]. Therefore, the calculated G_{r} only gives a rough estimate of the spin mixing conductance across the interface of the tested bilayers.

5.2.1 Temperature dependence

The occurence of a pronounced MR in the oopt rotation geometry in Pt/FM heterostructures gives rise to the assumption that the effect stems from an AMR in the FM layer. Presupposing this explanation, changes in the stack resistivity would be governed by magnetization orientation dependent differences in the scattering cross section for charge carriers

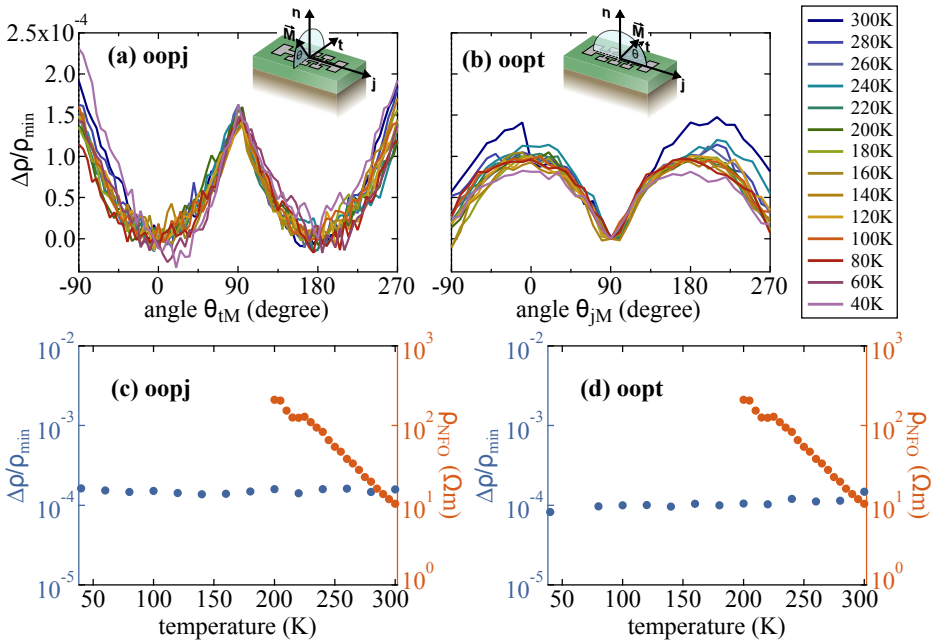

Fig. 5.2: Temperature dependent resistivity measurements for rotating magnetic fields in (a) oopj and (b) oopt geometry, as sketched in the respective insets. Graphs (c) and (d) display a comparison between the temperature dependent NFO resististivity and the effect amplitude in oopj and oopt configuration, respectively.

traveling through the FM layer. However, this effect should be absent in ferromagnetic insulating materials where no free charge carriers are available. Since the observations from section 3.2.2 clearly suggest that the sputter deposited NFO films are highly insulating at RT, they should not show an AMR. In order to test this hypothesis for validity and to unequivocally rule out an AMR from the FM in the examined sample structure, temperature dependent rotational measurements were performed on a Pt(3 nm)/NFO(58 nm) bilayer.

The resulting graphs for both geometries are displayed in Fig. 5.2. Graphs (a) and (b) depict the experimentally observed MR $\Delta\rho/\rho_{\mathrm{min}}$ in a range between 40 K and 300 K for the oopj and the oopt rotations, re-

spectively. In both geometries the effect does not alter significantly within the temperature region, ranging around $4.5 \cdot 10^{-4}$ in the oopj geometry and around $2 \cdot 10^{-4}$ in oopt. The oopt values are slightly smaller than the values observed before, since different samples were tested in the two experiments.

Comparing the temperature dependent changes of the MR effect amplitudes $\Delta\rho_{\mathrm{abs}}/\rho_{\mathrm{min}}$ with the NFO resistivity (data from section 3.2.2) does not reveal a correlation between the two properties. Both MR signatures are stable over the whole temperature range, while the NFO resistivity drops rapidly with increasing T. The large discrepancy between the MR behavior for both rotational geometries and the NFO resistivity indicates that the effects observed here are mainly independent of a charge transport in the NFO layer. Thus, the observed oscillation in the oopt rotational experiment cannot be explained by a conventional AMR from the FM layer, but probably originates from the Pt film.

5.2.2 Magnetic field dependence

In order to rule out an artificial effect generated by a misalignment of the magnetization regarding the magnetic field due to the strong magnetic shape anisotropy in the NFO films, the B-field dependence of the resistivity change was checked for the oopj and oopt rotations. The available magnetic field strenght of 1 T is not sufficient to fully rotate the magnetization out-of plane. Thus, the magnetization vector retains additional in-plane contributions even if the external field is collinear to the magnetic hard axis, i.e., the film plane normal. While a misalignment of the magnetization with the magnetic field reduces an SMR as well as an AMR, it can also induce artificial effects. In particular, in the oopt direction a misaligned magnetization might contain contributions oriented in the direction transverse to the current direction, i.e., perpendicular to the rotation plane, which introduces changes in the resistivity even in the absence of an AMR.

This effect should be more pronounced for small magnetic fields due to the weaker alignment. Therefore, it can be distinguished from an ac-

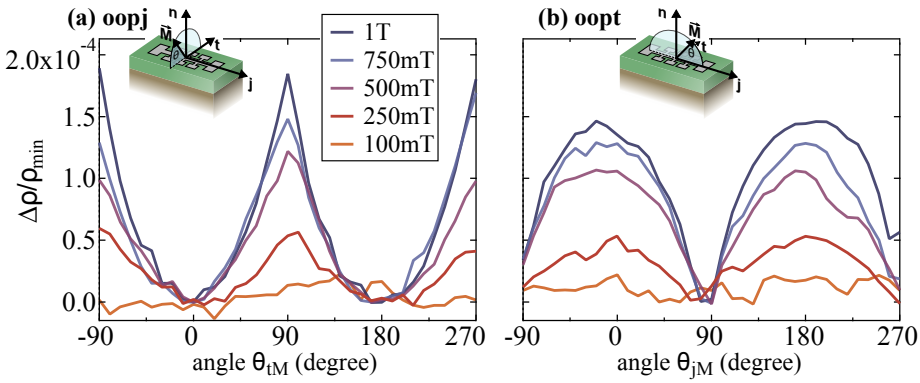

Fig. 5.3: Resistivity measurements with rotating magnetic fields with different field strengths in (a) oopj and (b) oopt geometry, as sketched in the respective insets. The effects exhibit a decrease in amplitude with reduced fields, as expected for both SMR and AMR.

tual MR effect by repeating the experiments for different field strengths. Fig. 5.3 shows the corresponding measurements. The field was varied in a range between 100 mT and 1 T and rotational measurements were performed. Both in the oopj and the oopt rotation the effects decrease with the field. In particular, the effects vanish completely for magnetic fields below 100 mT. This result clearly proves that neither of the two MRs can be attributed to artificial effects due to the magnetic anisotropy in the samples. Again, this is in agreement with an SMR in the oopj geometry but does not yield any further explanation for the observed oopt effect.

5.2.3 Other contributions - crystallinity, proximity AMR

Concluding from the previous results, a charge transport via mobile electrons in the NFO as well as a magnetic shape anisotropy with magnetic hard axis in the out-of-plane direction are excluded as the origin of the observed behavior. Additionally, the crystallographic structure of Pt can have an influence on the magnetoresistive response. Limmer et al. [76], McGuire et al. [75], Birss [77], and Muduli et al. [78] have shown that the AMR also depends on the crystallographic orientation of the material. In

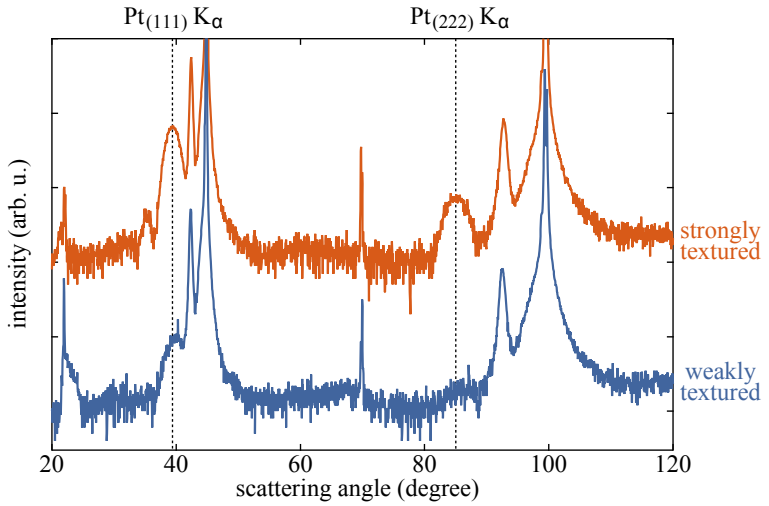

Fig. 5.4: Comparison between XRD scans of two Pt/NFO hybrids with strongly textured and weakly textured Pt films.

order to exclude the crystallography as a source of the observed AMR like effect, the impact of changes in the Pt structure was tested. XRD measurements illustrate that the investigated Pt layers exhibit a pronounced crystallization with a strong (111) texture when deposited on NFO (see upper curve in Fig. 5.4). However, by tuning the deposition parameters, bilayers with a much weaker Pt texture were obtained. Exemplary XRD scans of a bilayer with strongly textured Pt and a structure with weak Pt texture are shown in Fig. 5.4.

Analogously to the prior experiments the magnetization dependence of the resistivity was studied in rotational measurements on the films with weak texture (see Fig. 5.5). Similarly to the results obtained in the strongly textured films, the observations again show a magneotresistive behavior in both geometries, which is slightly reduced due to the different electrical properties of the Pt layers. In particular, the films with weaker texture exhibit a larger resistivity, in agreement with an increased charge scattering at impurities and grain boundaries. However, the effects are of the same order as before and no significant differences in the SMR/AMR

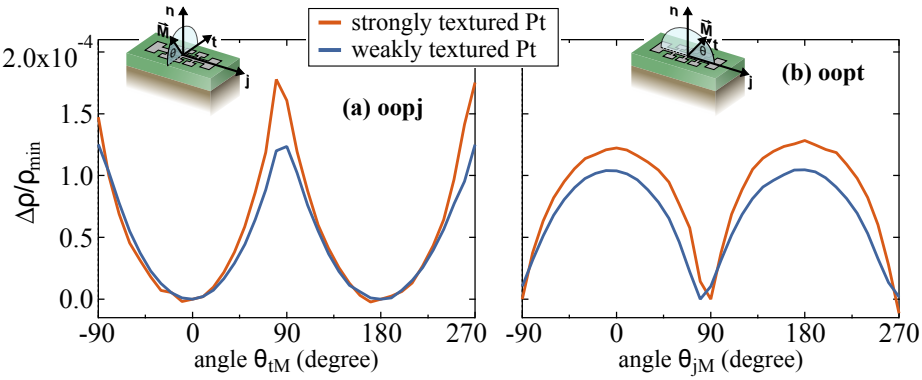

Fig. 5.5: Comparison between the observed MR contributions of two Pt/NFO hybrids with strongly textured and weakly textured Pt films in (a) oopj and (b) oopt configuration.

ratio occurs that could be ascribed to the crystallographic deviations. Therefore, the crystal texture does not account for the AMR signature in the experiments.

Another possible reason for the AMR like contribution to the resistivity is the static MPE inducing a spin polarization in the Pt layer. While in section 4.2.8 a magnetic moment in Pt was excluded down to a limit of $0.04\,\mu_B$ per atom in the sputter deposited Pt/NFO bilayer, it remains to be clarified if a spin polarization equal to or lower than this value can generate the observed magnetoresistive response. Comparing the AMR of different ferromagnetic materials like Fe, Ni, and Co shows a large scattering of the effect amplitudes [75], which illustrates that the AMR not only depends on the magnetic moment but mainly on the bandstructure and the scattering cross section of the orbitals. Therefore, it is crucial to consider the bandstructure to estimate whether a small induced magnetization in the Pt below the given limit suffices to generate the observed effect. Detailed *ab initio* calculations are necessary in order to gain a better understanding of the effect and to clarify the impact of a spin accumulation in the Pt layer on the resistivity.

An alternative explanation for the observed effect was given by Isasa et al. [173]. They observed a similar AMR like contribution in the oopt

geometry, which they attributed mainly to an ordinary magnetoresistance (OMR), where the Lorentz force from the external magnetic fields acts on the electron trajectory and causes differences in the resistivity for $\overrightarrow{M}$ parallel and perpendicular to the current. Yet, they carried out their measurements using very high external fields of up to 9 T, while their Pt films exhibited a very low resistivity, both promoting the occurrence of OMR. In this study much lower magnetic fields were applied and the Pt films show a much higher resistivity. Therefore, it is unlikely that the OMR accounts for the observed oopt signature completely. However, more detailed experiments have to be carried out in order to disambiguate this conclusively.

5.3 Conclusion

In this chapter sputter deposited Pt/NFO bilayers were tested for an SMR. In order to identify the effect and separate it from potential AMR contributions the resistivity was examined for rotational magnetic fields in the oopj and the oopt geometry. A pronounced $\cos(\theta_{\mathrm{tM}})^2$ oscillation corresponding to an SMR was observed in the oopj experiments in agreement with results from Althammer et al. on Pt/NFO heterostructures with chemical vapor deposited NFO [12]. Taking into account a strong shape anisotropy present in the NFO layers, the effect amplitude was determined to $\Delta\rho_{\mathrm{abs}}/\rho_{\mathrm{min}} = 4.4 \cdot 10^{-4}$, which is of the same order as the values found in the previous report on SMR in Pt/NFO. From this value a spin mixing conductance of $G_{\mathrm{r}} = 3.1 \cdot 10^{14}\,\Omega^{-1}\mathrm{m}^{-2}$ was calculated.

An oscillation in the oopt rotation gives rise to the assumption that the monitored samples exhibit an additional AMR. The effect amplitude in this configuration is $\Delta\rho_{\mathrm{abs}}/\rho_{\mathrm{min}} = 3.1 \cdot 10^{-4}$, thus slightly smaller but of the same order as the SMR. Since the investigated NFO layers should not generate an AMR, due to their semiconducting electronic properties, the occurence of this contribution is unclear and was studied in different measurements. Low temperature measurements show that the effect does not exhibit a strong temperature dependence like the NFO resistivity

and therefore is unlikely to originate from a charge transport in the NFO layer. An artifical MR induced by the misalignment of the magnetization regarding the magnetic field due to a magnetic shape anisotropy was ruled out via magnetic field strength dependent experiments. The decrease in amplitude for reduced magnetic fields contradicts the assumption that an additional in-plane contribution of the magnetization causes the AMR like effect. Next, the impact of the Pt crystallinity on a potential AMR was discussed. No significant influence of the Pt texture on the MR was observed, which proves that this property does not explain the observed signal either.

Thus, the origin of the AMR like effect in the oopt rotational measurements cannot be determined conclusively. Another possible explanation is given under the assumption of an induced spin polarization in the Pt layer from the adjacent NFO film. However, in order to evaluate a possible generation of an AMR from a static MPE below the previously determined limit, additional bandstructure calculations are necessary. Also, additional XRMR investigations on sputter deposited Pt/NFO samples with a higher precision than in section 4.2.8, e.g., at beamline BM28, would be beneficial in order to observe an induced magnetic moment below the given limit, if present.

6 Summary

In summary, this thesis focussed on the preparation and investigation of ferrimagnetic NFO films and NFO based heterostructures for an implementation in spin caloric and spintronic devices. The applicability of such devices critically depends on the exclusion of parasitic effects, which can originate from the FM itself or proximity induced interface effects. Therefore, the manufactured structures were carefully investigated for a static MPE in terms of an induced interface spin polarization in the Pt. Further, the samples were investigated for a non-equilibrium MPE in terms of the SMR.

Two different deposition techniques, i.e., CVD and reactive sputter deposition, were applied in order to synthesize NFO thin films. The respective samples were compared for their physical characteristics. From this, the benefits and deficiencies of the different layers were discussed and their applicability in different experiments was evaluated. It was found that in general reactive sputter deposition is well suited to obtain high quality NFO thin films with good crystallographic, electronic, and magnetic properties. In particular, the films produced in this way show a large resistivity and a well ordered cation distribution and are highly qualified for a utilization in spin caloritronic devices. Yet, the large coercivities and saturation fields require strong magnetic fields to align the magnetization, which limits the range of application. The thicker chemical vapor deposited films also show a high crystallinity and good magnetic properties. The comparatively small switching and saturation fields are beneficial for experiments where only small magnetic fields are available. However, the layers synthesized with this technique exhibit a larger divergence, i.e., a lower reproducibility, which makes a detailed characterization of each sample prior to a spin caloritronic utilization imperative.

Besides the film properties themselves, the interface properties of NM/FM bilayers also play a crucial role for application-oriented research, as they can give rise to parasitic effects. Therefore, in the next step the interfaces of different Pt/FM bilayers were tested for static MPEs using XRMR. First, a number of different Pt/FMM hybrids were monitored in order to gain a detailed understanding of this technique and the effect investigated. By measuring Pt/Fe heterostructures with different Pt thicknesses it was shown that XRMR does not exhibit a strong thickness dependence but is highly interface sensitive, which is beneficial for the investigation of induced interface spin polarizations. In an additional series of Pt/Fe bilayers with varying Fe thickness it could also be confirmed within this project that the static MPE is mainly independent of the whole FM film volume, but only depends on a couple of monolayers closest to the interface. The induced magnetic moments observed in the Pt/Fe hybrids are all well in line with a previous report on Pt/Fe bilayers studied with XMCD [114]. Further, XRMR on different Pt/$Ni_{1-x}Fe_x$ double layers shows a rapid decrease of the static MPE with decreasing Fe content. To examine this behavior in more detail and find the reason for this trend, additional XRMR measurements on $Co_{1-x}Fe_x$ are being planned.

XRMR investigations on Pt/NFO heterostructures with both chemical vapor deposited and sputter deposited NFO films presented here did not show any evidence of an induced spin polarization in the adjacent Pt layers, which is in line with the theoretical explanations of the static MPE in NM/FMI hybrids. Thus, for both sample structures, the effect can be excluded down to the resolution limit.

For comparison with other Pt/FMI systems, additional Pt/YIG bilayers were also tested with XRMR. It was found that the static MPE critically depends on the interface configuration and can even occur in Pt/FMI bilayers. While in a conventional Pt/YIG double layer no induced spin polarization was observed, an inverted YIG/Pt stack with the YIG deposited on top of the Pt layer produced a pronounced magnetic signature. The magnetic response is attributed to a strong intermixing at the YIG/Pt interface, which might introduce an exchange coupling of weakly oxidized

Fe and Pt interface states. However, the effect is very small and its impact on spin caloric and spintronic experiments remains to be investigated. Transport measurements on both Pt/YIG and YIG/Pt structures, respectively, are currently being performed by the group of S.T.B. Goennenwein at the WMI in Garching and will enable an evaluation of potential parasitic effects from a static MPE in these samples. Additionally, a cooperation with a large number of different groups involved in the fields of spin caloric transport and spin caloritronics is in progress in order to check their Pt/YIG films and rule out potential charge transport related effects in their experiments. Since the static MPE cannot be excluded instantly for Pt/FMI samples, but strongly depends on the interface configuration of each bilayer, this should lead to a more conclusive assessment of the observations reported in these fields. Also, in order to answer the question of a static MPE in NM/FMI hybrids more generally additional sample systems should be considered for upcoming investigations. As a continuation of this thesis a series of $NiFe_2O_x$ films with varying oxygen content is currently being prepared and studied for the influence of changes in the electronic properties on the static MPE. Furthermore, experiments on Pt/Fe_3O_4 bilayers above and below the Verwey transition, i.e., in a conducting and an insulating Fe_3O_4 state, are planned within this project.

In the final chapter of this thesis, sputter deposited Pt/NFO bilayers were examined for a non-equilibrium MPE, i.e., the SMR, and for possible parasitic MR contributions. The observed SMR is of the same order as reported in an earlier publication on chemical vapor deposited NFO films [12], however, an additional AMR like signature was also observed. The origin of this spurious contribution was tested in different experiments, but has not yet been explained. It is shown that the effect does not correspond to an AMR generated in the NFO layer, nor does it comply with an artificial effect induced by a strong magnetic in-plane anisotropy. Further measurements and theoretical calculations are needed for a more accurate explanation of the effect. In particular, the influence of a potential static MPE below the confirmed limit has to be evaluated.

As an additional result of this project Pt/NFO bilayers were provided for LSSE investigations in the studies of Meier et al. [23, 24] and for measurements of the SMR within the investigations of Althammer et al. [12].

A detailed conclusion of each experiment can also be found at the end of the corresponding chapters.

Bibliography

[1] S.A. Wolf, D.D. Awschalom, R.A. Buhrman, J.M. Daughton, S. von Molnár, M.L. Roukes, A.J. Chtchelkanova, D.M. Treger, Science **294**, 1488 (2001).

[2] K. Uchida, S. Takahashi, K. Harii, J. Ieda, W. Koshibae, K. Ando, S. Maekawa, and E. Saitoh, Nature **455**, 778 (2008).

[3] K. Uchida, H. Adachi, T. Ota, H. Nakayama, S. Maekawa, and E. Saitoh, Appl. Phys. Lett. **97**, 172505 (2010).

[4] G.E.W. Bauer, E. Saitoh, and B.J. van Wees, Nat. Mater. **11**, 391 (2012).

[5] S. Y. Huang, W.G. Wang, S.F. Lee, J. Kwo, and C.L. Chien, Phys. Rev. Lett. **107** 216604 (2011).

[6] A.D. Avery, M.R. Pufall, and B.L. Zink, Phys. Rev. Lett. **109**, 196602 (2012).

[7] M. Schmid, S. Srichandan, D. Meier, T. Kuschel, J.-M. Schmalhorst, M. Vogel, G. Reiss, C. Strunk, and C.H. Back, Phys. Rev. Lett. **111**, 187201 (2013).

[8] D. Meier, D. Reinhardt, M. Schmid, C.H. Back, J.-M. Schmalhorst, T. Kuschel, and G. Reiss, Phys. Rev. B **88**, 184425 (2013).

[9] H. Nakayama, M. Althammer, Y.-T. Chen, K. Uchida, Y. Kajiwara, D. Kikuchi, T. Ohtani, S. Geprägs, M. Opel, S. Takahashi, R. Gross, G.E.W. Bauer, S.T.B. Goennenwein, and E. Saitoh, Phys. Rev. Lett. **110**, 206601 (2013).

[10] Y.-T. Chen, S. Takahashi, H. Nakayama, M. Althammer, S. T. B. Goennenwein, E. Saitoh, and G. E. W. Bauer, Phys. Rev. B **87**, 144411 (2013).

[11] N. Vlietstra, J. Shan, V. Castel, B.J. van Wees, and J. Ben Youssef, Phys. Rev. B **87**, 184421 (2013).

[12] M. Althammer, S. Meyer, H. Nakayama, M. Schreier, S. Altmannshofer, M. Weiler, H. Huebl, S. Geprägs, M. Opel, R. Gross, D. Meier, C. Klewe, T. Kuschel, J.-M. Schmalhorst, G. Reiss, L. Shen, A. Gupta, Y.-T. Chen, G.E.W. Bauer, E. Saitoh, and S.T.B. Goennenwein, Phys. Rev. B **87**, 224401 (2013).

[13] A.A. Serga, A.V. Chumak, and B. Hillebrands, J. Phys. D: Appl. Phys. **43**, 264002 (2010).

[14] S. Geller, and M.A. Gilleo, J. Phys. Chem. Solids **3**, 30 (1957).

[15] S. Geller, H.J. Williams, R.C. Sherwood, and G.P. Espinosa, J. Phys. Chem. Solids **23**, 1525 (1962).

[16] R. Metselaar, and P.K. Larsen, Sol. State Commun. **15**, 291 (1974).

[17] P.K. Larsen, and R. Metselaar, Phys. Rev. B **14**, 2520 (1976).

[18] D. Meier, T. Kuschel, L. Shen, A. Gupta, T. Kikkawa, K. Uchida, E. Saitoh, J.-M. Schmalhorst, and G. Reiss, Phys. Rev. B **87**, 054421 (2013).

[19] Y.M. Lu, Y. Choi, C.M. Ortega, X.M. Cheng, J.W. Cai, S.Y. Huang, L. Sun, and C. L. Chien, Phys. Rev. Lett. **110**, 147207 (2013).

[20] S. Geprägs, S. Meyer, S. Altmannshofer, M. Opel, F. Wilhelm, A. Rogalev, R. Gross, and S. T. B. Goennenwein, Appl. Phys. Lett. **101**, 262407 (2012).

[21] S. Geprägs, S.T.B. Goennenwein, M. Schneider, F. Wilhelm, K. Ollefs, A. Rogalev, M. Opel, and R. Gross, arXiv:1307.4869 (2013).

[22] M. Valvidares, N. Dix, M. Isasa, K. Ollefs, F. Wilhelm, A. Rogalev, F. Sánchez, E. Pellegrin, A. Bedoya-Pinto, P. Gargiani, L.E. Hueso, F. Casanova, and J. Fontcuberta, arXiv: **1510.01080** (2015).

[23] D. Meier, D. Reinhardt, M. van Straaten, C. Klewe, M. Althammer, M. Schreier, S.T.B. Goennenwein, A. Gupta, M. Schmid, C.H. Back, J.-M. Schmalhorst, T. Kuschel, and G. Reiss, Nat. Commun. **6**, 8211 (2015).

[24] D. Meier, PhD thesis, Bielefeld University (2015).

[25] T. Kuschel, C. Klewe, P. Bougiatioti, O. Kuschel, J. Wollschläger, L. Bouchenoire, S. Brown, J.-M. Schmalhorst, D. Meier, and G. Reiss, accepted by IEEE Trans. Magn. (2015).

[26] K. Uchida, T. Nonaka, T. Ota, and E. Saitoh, Appl. Phys. Lett. **97**, 262504 (2010).

[27] T. Niizeki, T. Kikkawa, K. Uchida, M. Oka, K. Z. Suzuki, H. Yanagihara, E. Kita, and E. Saitoh, AIP Advances **5**, 053603 (2015).

[28] E. Guo, A. Herklotz, A. Kehlberger, J. Cramer, G. Jakob, M. Kläui, arXiv: **1509.03601** (2015).

[29] R. Ramos, T. Kikkawa, K. Uchida, H. Adachi, I. Lucas, M. H. Aguirre, P. Algarabel, L. Morellón, S. Maekawa, E. Saitoh, and M. R. Ibarra, Appl. Phys. Lett. **102**, 072413 (2013).

[30] E.J.W. Verwey, and E.L. Heilmann, J. Chem. Phys. **15** 174 (1947).

[31] M. Hoppe, S. Döring, M. Gorgoi, S. Cramm, and M. Müller, Phys. Rev. B **91**, 054418 (2015).
http://dx.doi.org/10.1103/PhysRevB.91.054418

[32] R. Pauthenet, Ann. Phys. **7**, 710 (1952).

[33] G.F. Dionne, J. Appl. Phys. **63**, 3777 (1988).

[34] S. Venzke, R.B. van Dover, J.M. Phillips, E.M. Gyorgy, T.Siegrist, C.-H. Chen, D. Werder, R.M. Fleming, R.J. Felder, E. Coleman, and R. Opila, J. Mater. Res. **11**, 1187 (1996).

[35] F. Rigato, S. Estradé, J. Arbiol, F. Peiró, U. Lüders, X. Martí, F. Sánchez, and J. Fontcuberta, Mat. Sci. Eng. B **144**, 43 (2007).

[36] U. Lüders, A. Barthélémy, M. Bibes, K. Bouzehouane, S. Fusil, E. Jacquet, J.-P. Contour, J.-F. Bobo, J. Fontcuberta, and A. Fert, Adv. Mater. **18**, 1733 (2006).

[37] G.A. Sawatzky, and J.W. Allen, Phys. Rev. Lett. **53**, 2339 (1984).

[38] G.P. Joshi, N.S. Saxena, R. Mangal, A. Mishra, and T.P. Sharma, Bull. Mater. Sci. **26**, 387 (2003).

[39] S. Balaji, R.K. Selvan, L.J. Berchmans, S. Angappan, K. Subramanian, and C.O. Augustin, Mater. Sci. Eng. B **119**, 119 (2005).

[40] S.N. Dolia, R. Sharma, M.P. Sharma, and N.S. Saxena, Indian J. Pure Appl. Phys. **44**, 774 (2006).

[41] J. Haetge, C. Suchomski, and T. Brezesinski, Inorg. Chem. **49**, 11619 (2010).

[42] Q.-C. Sun, H. Sims, D. Mazumdar, J.X. Ma, B.S. Holinsworth, K.R. O'Neal, G. Kim, W.H. Butler, A. Gupta, and J.L. Musfeldt, Phys. Rev. B **86**, 205106 (2012).

[43] R.C. Rai, S. Wilser, M. Guminiak, B. Cai, and M.L. Nakarmi, Appl. Phys. A **106**, 207 (2012).

[44] H. Lord, and R. Parker, Letters to Nature **188**, 929 (1960).

[45] E.J.W. Verwey, and P.W. Haayman, Physica **8**, 979 (1941).

[46] L.G. Van Uitert, J. Chem. Phys. **23**, 1883 (1955).

[47] I.G. Austin, and D. Elwell, Contemp. Phys. **11**, 455 (1970).

[48] E.J.W. Verwey, P.W. Haayman, F.C. Romeijn and G.W. van Oosterhout, Philips Research Report **5**, 173 (1950).

[49] J.H. De Boer, and E.J.W. Verwey, Proc. Phys. Soc. **49**, 59 (1937).

[50] P.K. Manna, and S.M. Yusuf, Phys. Rep. **535**, 61 (2014).

[51] J.J. Hauser, Phys. Rev. **187**, 580 (1969).

[52] E.P. Wohlfarth, J. Phys. Chem. Solids **1**, 35 (1956).

[53] J. Crangle, Phil. Mag. **5**, 335 (1960).

[54] B.N. Cox, R.A. Tahir-Kheli, and R.J. Elliott, Phys. Rev. B **20**, 2864 (1979).

[55] M.A. Ruderman, and C. Kittel, Phys. Rev. **96**, 99 (1954).

[56] T. Kasuya, Prog. Theor. Phys. **16**, 45 (1956).

[57] K. Yosida, Phys. Rev. **106**, 893 (1957).

[58] S. Blügel, B. Drittler, R. Zeller, and P.H. Dederichs, Appl. Phys. A **49**, 547 (1989).

[59] E.C. Stoner, Proc. R. Soc. Lond. A **165**, 372 (1938).

[60] S. Rüegg, G. Schütz, P. Fischer, R. Wienke, W.B. Zeper, and H. Ebert, J. Appl. Phys. **69**, 5655 (1991).

[61] S.K. Saha, V.S. Stepanyuk, and J. Kirschner, Phys. Lett. A **378**, 3642 (2014).

[62] Tao Lin, M.A. Tomaz, M.M. Schwickert, and G.R. Harp, Phys. Rev. B **58**, 862 (1998).

[63] M.M. Schwickert, R. Coehoorn, M.A. Tomaz, E. Mayo, D. Lederman, W.L. O'Brien, Tao Lin, and G.R. Harp, Phys. Rev. B **97**, 13681 (1998).

[64] M.M. Schwickert, G.Y. Guo, M.A. Tomaz, W.L. O'Brien, and G.R. Harp, Phys. Rev. B **58**, R4289 (1998).

[65] M.M. Sigalas, and D.A. Papaconstantopoulos, Phys. Rev. B **50**, 7255 (1994).

[66] S.Y. Huang, X. Fan, D. Qu, Y.P. Chen, W.G. Wang, J. Wu, T.Y. Chen, J.Q. Xiao, and C.L. Chien, Phys. Rev. Lett. **109**, 107204 (2012).

[67] Y.M. Lu, J.W. Cai, S.Y. Huang, D. Qu, B.F. Miao, and C.L. Chien, Phys. Rev. B **87**, 220409 (2013)

[68] T. Kikkawa, K. Uchida, Y. Shiomi, Z. Qiu, D. Hou, D. Tian, H. Nakayama, X.-F. Jin, and E. Saitoh, Phys. Rev. Lett. **110**, 067207 (2013).

[69] J.X. Li, M.W. Jia, Z. Ding, J.H. Liang, Y.M. Luo, and Y.Z. Wu, Phys. Rev. B **90**, 214415 (2014).

[70] M. Weiler, M. Althammer, F.D. Czeschka, H. Huebl, M.S. Wagner, M. Opel, I.-M. Imort, G. Reiss, A. Thomas, R. Gross, and S.T.B. Goennenwein, Phys. Rev. Lett. **108**, 106602 (2012).

[71] W. Thomson, Proc. R. Soc. Lond. **8**, 546 (1856).

[72] J. Smit, Physica XVI **6**, 612 (1951).

[73] I.A. Campbell, A. Fert and O. Jaoul, J. Phys. C: Metal Phys. Suppl. **1**, 95 (1970).

[74] N.F. Mott, Proc. Phys. Soc. **47**, 571 (1935).

[75] T.R. McGuire, and R.I. Potter, IEEE Trans. Magn. **11**, 1018 (1975).

[76] W. Limmer, M. Glunk, J. Daeubler, T. Hummel, W. Schoch, R. Sauer, C. Bihler, H. Huebl, M.S. Brandt, and S.T.B. Goennenwein, Phys. Rev. B **74**, 205205 (2006).

[77] R.R. Birss, Symmetry and Magnetism, North-Holland, Amsterdam, (1966).

[78] P.K. Muduli, K.-J. Friedland, J. Herfort, H.-P. Schönherr, and K.H. Ploog, Phys. Rev. B **72**, 104430 (2005).

[79] W. Limmer, J. Daeubler, L. Dreher, M. Glunk, W. Schoch, S. Schwaiger, and R. Sauer, Phys. Rev. B **77**, 205210 (2008).

[80] M.I. Dyakonov, and V.I. Perel, Phys. Lett. A **35**, 459 (1971).

[81] C. Lewiner, O. Betbecer-Matibet, and P. Nozières, J. Phys. Chem. Solids **34**, 765 (1973).

[82] P. Nozières, and C. Lewiner, J. Phys. (Paris) **34**, 901 (1973).

[83] J.N. Chazalviel, and I. Solomon, Phys. Rev. Lett. **29**, 1676 (1972).

[84] J.N. Chazalviel, Phys. Rev. B **11**, 3918 (1975).

[85] J. E. Hirsch, Phys. Rev. Lett. **83**, 1834 (1999).

[86] Y.K. Kato, R.C. Myers, A.C. Gossard, D.D. Awschalom, Science, **306**, 1910 (2004).

[87] S. Takahashi, and S. Maekawa, Sci. Technol. Adv. Mater. **9**, 014105 (2008).

[88] J. Sinova, S.O. Valenzuela, J. Wunderlich, C.H. Back, T. Jungwirth, Rev. Mod. Phys. **87**, 1213 (2015).

[89] L. Liu, T. Moriyama, D.C. Ralph, and R.A. Buhrman, Phys. Rev. Lett. **106**, 036601 (2011).

[90] C.-F. Pai, L. Liu, Y. Li, H. W. Tseng, D.C. Ralph, and R.A. Buhrman, Appl. Phys. Lett. **101**, 122404 (2012).

[91] L. Liu, C.F. Pai, Y. Li, H.W. Tseng, D.C. Ralph, and R.A. Buhrman, Science **336**, 555 (2012).

[92] N.F. Mott, Proc. R. Soc. Lond. A **117**, 610 (1928).

[93] V.V. Mkhitaryan and M.E. Raikh, Phys. Rev. B **77**, 245428 (2008).

[94] L. Berger, Phys. Rev. B **2**, 4559 (1970).

[95] A. Hoffmann, IEEE Trans. Magn. **49**, 5172 (2013).

[96] G. Vignale, J. Supercond. Nov. Magn. **23**, 3 (2010).

[97] W.-K. Tse, and S. Das Sarma, Phys. Rev. B **74**, 245309 (2006).

[98] E.M. Hankiewicz, and G. Vignale, Phys. Rev. B **100**, 026602 (2008).

[99] O.P. Sushkov, A.I. Milstein, M. Mori, and S. Maekawa, Europhys. Lett. **103**, 47003 (2013).

[100] A.K. Majumdar and L. Berger, Phys. Rev. B **7**, 4203 (1973).

[101] A. Fert, Physica **86-88B**, 491 (1977).

[102] W.C. Röntgen, *Ueber eine neue Art von Strahlen*, Sonderabbdruck aus den Sitzungsberichten der Würzburger Physik.-medic. Gesellschaft 1895, Vorläufige Mittheilung (1896).

[103] A. Kobs, S. Heße, W. Kreuzpaintner, G. Winkler, D. Lott, P. Weinberger, A. Schreyer, and H.P. Oepen, Phys. Rev. Lett. **106**, 217207 (2011).

[104] O. Bunău, Y. Joly, J. Phys.: Condens. Matter **21**, 345501 (2009).

[105] G. Schütz, W. Wagner, W. Wilhelm, P. Kienle, R. Zeller, R. Frahm, G. Materlik, Phys. Rev. Lett. **58**, 737 (1987).

[106] H. Wende, and C. Antoniak, Springer Proc. in Phys. **133**, 145 (2010).

[107] G. Schütz, E. Goering, and H. Stoll, Handbook of Magnetism and Advanced Magnetic Materials **3**, 1311 (2007).

[108] B.T. Thole, P. Carra, F. Sette, and G. van der Laan, Phys. Rev. Lett. **68**, 1943 (1992).

[109] P. Carra, B.T. Thole, M. Altarelli, and X. Wang, Phys. Rev. Lett. **70**, 694 (1993).

[110] F. Wilhelm, P. Poulopoulos, A. Scherz, H. Wende, K. Baberschke, M. Angelakeris, N. K. Flevaris, J. Goulon, and A. Rogalev, Phys. Stat. Sol. (a) **196**, 33 (2003).

[111] F. Wilhelm, P. Poulopoulos, G. Ceballos, H. Wende, K. Baberschke, P. Srivastava, D. Benea, H. Ebert, M. Angelakeris, N.K. Flevaris, D. Niarchos, A. Rogalev, and N.B. Brookes, Phys. Rev. Lett. **85**, 413 (2000).

[112] P. Poulopoulos, F. Wilhelm, H. Wende, G. Ceballos, K. Baberschke, D. Benea, H. Ebert, M. Angelakeris, N.K. Flevaris, A. Rogalev, and N.B. Brookes, J. Appl. Phys. **89**, 3874 (2001).

[113] M. Suzuki, H. Muraoka, Y. Inaba, H. Miyagawa, N. Kawamura, T. Shimatsu, H. Maruyama, N. Ishimatsu, Y. Isohama,. and Y. Sonobe, Phys. Rev. B **72**, 054430 (2005).

[114] W.J. Antel, Jr., M.M. Schwickert, Tao Lin, W.L. O'Brien, and G.R. Harp, Phys. Rev. B **60**, 12933 (1999).

[115] M.A. Tomaz, W.J. Antel Jr, W.L. O'Brien, and G.R. Harp, J. Phys. Condens. Matter **9**, L179 (1997).

[116] C. Ederer, M. Komelj, M. Fähnle, and G. Schütz, Phys. Rev. B **66**, 094413 (2002).

[117] J. Geissler, E. Goering, M. Justen, F. Weigand, G. Schütz, J. Langer, D. Schmitz, H. Maletta, and R. Mattheis, Phys. Rev. B **65**, 020405(R) (2001).

[118] S. Macke and E. Goering, J. Phys.: Condens. Matter **26**, 363201 (2014).

[119] D.K.G. de Boer, A.J.G. Leenaers, and W.W. van den Hoogenhof, X-ray Spectr. **24**, 91 (1995).

[120] J.D. Jackson, Classical Electrodynamics, Second Edition, John Wiley & Sons: New York (1975).

[121] L.G. Parratt, Phys. Rev. **95**, 359 (1954).

[122] D.G. Stearns, J. Appl. Phys. **65**, 491 (1989).

[123] L. Névot and P. Croce, Revue de Physique Appliquee **15**, 761 (1980).

[124] H. Zabel, Appl. Phys. A **58**, 159 (1994).

[125] J.P. Hannon, G.T. Trammell, M. Blume, and D. Gibbs, Phys. Rev. Lett. **61**, 1245 (1988).

[126] S. Macke, ReMagX - x-ray magnetic reflectivity tool, www.remagx.org

[127] J. Zak, E.R. Moog, C. Liu, and S.D. Bader, J. Magn. Magn. Mater. **89**, 107 (1990).

[128] M. Elzo, E. Jal, O. Bunau, S. Grenier, Y. Joly, A.Y. Ramos, H.C.N. Tolentino, J.M. Tonnerre, and N.Jaouen, J. Magn. Magn. Mater. **324**, 105 (2012).

[129] T. Kuschel, PhD thesis, University of Osnabrück (2011).

[130] B.L. Henke, E.M. Gullikson, and J.C. Davis, X-ray interactions: photoabsorption, scattering, transmission, and reflection at E=50-30000 eV, Z=1-92, Atomic Data and Nuclear Data Tables **Vol. 54** (no.2), 181 (1993).

[131] C. Klewe, M. Meinert, A. Boehnke, K. Kuepper, E. Arenholz, A. Gupta, J.-M. Schmalhorst, T. Kuschel, and G. Reiss, J. Appl. Phys. **115**, 123903 (2014).

[132] N. Li, Y.-H.A. Wang, M.N. Iliev, T.M. Klein, and A. Gupta, Chem. Vap. Deposition **17**, 261 (2011).

[133] D.T. Margulies, F.T. Parker, M.L. Rudee, F.E. Spada, J.N. Chapman, P.R. Aitchison, and A.E. Berkowitz, Phys. Rev. Lett. **79**, 5162 (1997).

[134] J. F. Bobo, D. Basso, E. Snoeck, C. Gatel, D. Hrabovsky, J. L. Gauffier, L. Ressier, R. Mamy, S. Visnovsky, J. Hamrle, J. Teillet, and A. R. Fert, Eur. Phys. J. B **24**, 43 (2001).

[135] R. Datta, S. Kanuri, V. Karthik, D. Mazumdar, J.X. Ma, and A. Gupta, Appl. Phys. Lett. **97**, 071907 (2010).

[136] E. Stavitski and F. M. F. de Groot, Micron **41**, 687 (2010).

[137] E. Arenholz, G. van der Laan, R. V. Chopdekar, and Y. Suzuki, Phys. Rev. B **74**, 094407 (2006).

[138] E. Arenholz, G. van der Laan, R. V. Chopdekar, and Y. Suzuki, Phys. Rev. Lett. **98**, 197201 (2007).

[139] M. Foerster, J.-M. Rebled, S. Estradé, F. Sánchez, F. Peiró, and J. Fontcuberta, Phys. Rev. B **84**, 144422 (2011).

[140] T. Kuschel, J. Hamrle, J. Pištora, K. Saito, S. Bosu, Y. Sakuraba, K. Takanashi, and J. Wollschläger, J. Phys. D: Appl. Phys. **45**, 495002 (2012).

[141] J.-B. Moussy, S. Gota, A. Bataille, M.-J. Guittet, and M. Gautier-Soyer, Phys. Rev. B **70**, 174448 (2004).

[142] D. Fritsch, and C. Ederer , Phys. Rev. B **82**, 104117 (2010).

[143] Z. Qiu, K. Ando, K. Uchida, Y. Kajiwara, R. Takahashi, H. Nakayama, T. An, Y. Fujikawa, and E. Saitoh, Appl. Phys. Lett. **103**, 092404 (2013).

[144] B.S. Holinsworth, D. Mazumdar, H. Sims, Q.-C. Sun, M.K. Yurtisigi, S.K. Sarker, A. Gupta, W.H. Butler, and J.L. Musfeldt, Appl. Phys. Lett. **103**, 082406 (2013).

[145] M. Meinert and G. Reiss, J. Phys. Condens. Matter **26**, 115503 (2014).

[146] C. Jin, Q. Zhang, W.B. Mi, E.Y. Jiang, and H.L. Bai, J. Phys. D: Appl. Phys. **43**, 385001 (2010).

[147] N. Ponpandian, P. Balaya, and A. Narayanasamy, J. Phys. Condens. Matter **14**, 3221 (2002).

[148] S. Uhlenbrock, C. Scharfschwerdt, M. Neumann, G. Illing, and H. Freund, J. Phys. Condens. Matter **4**, 7973 (1992).

[149] K.C. Prince, M. Matteucci, K. Kuepper, S.G. Chiuzbaian, S. Bartkowski, and M. Neumann, Phys. Rev. B **71**, 085102 (2005).

[150] D. Bruns, S.R. Lindemann, K. Kuepper, T. Schemme, and J. Wollschlager, Appl. Phys. Lett. **103**, 052401 (2013).

[151] M. Taguchi, M. Matsunami, Y. Ishida, R. Eguchi, A. Chainani, Y. Takata, M. Yabashi, K. Tamasaku, Y. Nishino, T. Ishikawa, Y. Senba, H. Ohashi, and S. Shin, Phys. Rev. Lett. **100**, 206401 (2008).

[152] M.A. Van Veenendaal, and G.A. Sawatzky, Phys. Rev. Lett. **70**, 2459 (1993).

[153] G. Hassnain Jaffari, A.K. Rumaiz, J.C. Woicik, and S. Ismat Shah, J. Appl. Phys. **111**, 093906 (2012).

[154] Y. X. Lu, J. S. Claydon, Y. B. Xu, S. M. Thompson, K. Wilson, G. van der Lann, Phys. Rev. B **70**, 233304 (2004).

[155] Z. Szotek, W.M. Temmerman, D. Ködderitzsch, A. Svane, L. Petit, and H. Winter, Phys. Rev. B **74**, 174431 (2006).

[156] G. van der Laan, C. M. B Henderson, R. A. D. Pattrick, S. S. Dhesi, P. F. Schofield, E. Dudzik, D. J. Vaughan, Phys. Rev. B **59**, 4314 (1999).

[157] T. Kuschel, C. Klewe, J.-M. Schmalhorst, F. Bertram, O. Schuckmann, T. Schemme, J. Wollschläger, S. Francoual, J. Strempfer, A. Gupta, M. Meinert, G. Götz, D. Meier, and G. Reiss, Phys. Rev. Lett. **115**, 097401 (2015).

[158] T. Kuschel, C. Klewe, J.-M. Schmalhorst, F. Bertram, O. Schuckmann, T. Schemme, J. Wollschläger, S. Francoual, J. Strempfer, A. Gupta, M. Meinert, G. Götz, D. Meier, and G. Reiss, Phys. Rev. Lett. **115**, 097401 (2015) *Supplementary material*.

[159] C. Klewe, T. Kuschel, J.-M. Schmalhorst, F. Bertram, O. Kuschel, J. Wollschläger, J. Strempfer, M. Meinert, and G. Reiss, submitted (2015), arXiv: **1508.00379**.

[160] J. Strempfer, S. Francoual, D. Reuther, D. K. Shukla, A. Skaugen, H. Schulte-Schrepping, T. Kracht, and H. Franz, J. Synchrotron Rad. **20**, 541 (2013).

[161] S.D. Brown, L. Bouchenoire, D. Bowyer, J. Kervin, D. Laundy, M.J. Longfield, D. Mannix, D.F. Paul, A. Stunault, P. Thompson, M.J. Cooper, C.A. Lucas, and W.G. Stirling, J. Synchrotron Rad. **8**, 1172 (2001).

[162] S.P. Collins, A. Bombardi, A.R. Marshall, J.H. Williams, G. Barlow, A.G. Day, M.R. Pearson, R.J. Woolliscroft, R.D. Walton, G. Beutier, and G. Nisbet, Conf. Proc.: 10th International Conference on Synchrotron Radiation Instrumentation (SRI 2010), 303 (2010).

[163] G. Evans, R. F. Pettifer, J. Appl. Crystallogr. **34**, 82 (2001).

[164] A.V. Kolobov, F. Wilhelm, A. Rogalev, T. Shima, and J. Tominaga, Appl. Phys. Lett. **86**, 121909 (2005).

[165] G. Schütz, R. Wienke, W. Wilhelm, W.B. Zeper, H. Ebert, K. Spörl, J. Appl. Phys. **67**, 4456 (1990).

[166] S. Brück, S. Macke, E. Goering, X. Ji, Q. Zhan, and K. M. Krishnan, Phys. Rev. B **81**, 134414 (2010).

[167] J. Crangle, and G.C. Hallam, Proc. R. Soc. London Ser. A **272**, 119 (1963).

[168] E.J. Kondorskii, and J.N Fedotov, Izv. Akad. Nauk. SSSR **16**, 432 (1952).

[169] D. Altbir, M. Kiwi, G. Martinez, and M.J. Zuckermann, Phys. Rev. B **40**, 6963 (1989).

[170] D. Meier, T. Kuschel, S. Meyer, S.T.B. Goennenwein, L. Shen, A. Gupta, J.-M. Schmalhorst, G. Reiss, accepted by AIP Advances (2015).

[171] M. Schreier, G.E.W. Bauer, V.I. Vasyuchka, J. Flipse, K. Uchida, J. Lotze, V. Lauer, A.V. Chumak, A.A. Serga, S. Daimon, T. Kikkawa, E. Saitoh, B.J. van Wees, B. Hillebrands, R. Gross, and S.T.B. Goennenwein, J. Phys. D: Appl. Phys. **48**, 025001 (2015).

[172] K. Kontotolis, Master thesis, Bielefeld University (2015).

[173] M. Isasa, E. Sagasta, A. Bedoya-Pinto., S. Vélez, N. Dix, F. Sánchez, L.E. Hueso, J. Fontcuberta, and F. Casanova, arXiv: **1510.01449** (2015).

Publications and Conferences

Publications

- M. Meinert, J.-M. Schmalhorst, **C. Klewe**, G. Reiss, E. Arenholz, T. Böhnert, and K. Nielsch, 'Itinerant and localized magnetic moments in ferrimagnetic Mn_2CoGa thin films probed by x-ray magnetic linear dichroism: Experiment and ab initio theory'. Phys. Rev. B **84**, 132405 (2011).

- **C. Klewe**, M. Meinert, J. Schmalhorst, and G. Reiss, 'Negative spin polarization of Mn_2VGa probed by tunnel magnetoresistance'. J. Phys.: Condens. Matter **25**, 076001 (2013).

- M. Althammer, S. Meyer, H. Nakayama, M. Schreier, S. Altmannshofer, M. Weiler, H. Huebl, S. Geprägs, M. Opel, R. Gross, D. Meier, **C. Klewe**, T. Kuschel, J.-M. Schmalhorst, G. Reiss, L. Shen, A. Gupta, Y.-T. Chen, G. E. W. Bauer, E. Saitoh, and S. T. B. Goennenwein, 'Quantitative study of the spin Hall magnetoresistance in ferromagnetic insulator/normal metal hybrids'. Phys. Rev. B **87**, 224401 (2013).

- **C. Klewe**, M. Meinert, A. Boehnke, K. Kuepper, E. Arenholz, A. Gupta, J.-M. Schmalhorst, T. Kuschel, and G. Reiss, 'Physical characteristics and cation distribution of $NiFe_2O_4$ thin films with high resistivity prepared by reactive co-sputtering'. J. Appl. Phys. **115**, 123903 (2014).

- L. Marnitz, K. Rott, S. Niehörster, **C. Klewe**, D. Meier, S. Fabretti, M. Witziok, A. Krampf, O. Schuckmann, T. Schemme, K. Kuepper,

J. Wollschläger, A. Thomas, G. Reiss, and T. Kuschel, 'Sign change in the tunnel magnetoresistance of Fe_3O_4/MgO/Co-Fe-B magnetic tunnel junctions depending on the annealing temperature and the interface treatment'. AIP Advances **5**, 047103 (2015).

- T. Kuschel, **C. Klewe**, J.-M. Schmalhorst, F. Bertram, O. Kuschel, T. Schemme, J. Wollschläger, S. Francoual, J. Strempfer, A. Gupta, M. Meinert, G. Götz, D. Meier, and G. Reiss, 'Static magnetic proximity effect in Pt/$NiFe_2O_4$ and Pt/Fe bilayers investigated by x-ray resonant magnetic reflectivity'. , Phys. Rev. Lett. **115**, 097401 (2015).

- D. Meier, D. Reinhardt, M. van Straaten, **C. Klewe**, M. Althammer, M. Schreier, S. T. B. Goennenwein, A. Gupta, M. Schmid, C. H. Back, J.-M. Schmalhorst, T. Kuschel, and G. Reiss, 'Longitudinal spin Seebeck effect contribution in transverse spin Seebeck effect experiments in Pt/YIG and Pt/NFO'. Nat. Commun. **6**, 8211 (2015).

- **C. Klewe**, T. Kuschel, J.-M. Schmalhorst, F. Bertram, O. Kuschel, J. Wollschläger, J. Strempfer, M. Meinert, and G. Reiss, 'Static magnetic proximity effect in Pt/$Ni_{1-x}Fe_x$ bilayers investigated by x-ray resonant magnetic reflectivity'. submitted to Phys. Rev. B (2015), arXiv:1508.00379.

- T. Kuschel, **C. Klewe**, P. Bougiatioti, O. Kuschel, J. Wollschläger, L. Bouchenoire, S. Brown, J.-M. Schmalhorst, D. Meier, and G. Reiss, 'Static magnetic proximity effect in Pt layers on sputter-deposited $NiFe_2O_4$ and on Fe of various thicknesses investigated by XRMR'. accepted by IEEE Trans. Magn. (2015).

Conferences

- C. Klewe et al., 'Inverse tunnel magnetoresistance with Mn_2VGa based magnetic tunnel junctions', DPG spring meeting, Berlin (2012), Poster
- C. Klewe et al., 'Structural and magnetic properties of $NiFe_2O_4$ thin films prepared by different deposition techniques', 510th WE-Heraeus seminar on non-magnetic control of spin, Bad Honnef (2013), Poster
- C. Klewe et al., 'Structural and magnetic properties of $NiFe_2O_4$ thin films prepared by different deposition techniques', DPG spring meeting, Regensburg (2013), Poster
- C. Klewe et al., 'Physical properties and cation distribution of $NiFe_2O_4$ thin films prepared for spincaloric and spintronic applications', SpinCaT PhD workshop, Dresden (2013), Talk
- C. Klewe et al., 'Investigations of static proximity effects in $NiFe_2O_4$/Pt bilayers by x-ray resonant magnetic reflectivity', 550th WE-Heraeus seminar on spin transport beyond Boltzmann, Bad Honnef (2014), Poster (Award for best 'shotgun poster presentation')
- C. Klewe et al., 'Investigations of static proximity effects in $NiFe_2O_4$/Pt bilayers by x-ray resonant magnetic reflectivity', DESY Photon Science users meeting, Hamburg (2014), Poster
- C. Klewe et al., 'Structural and magnetic properties of $NiFe_2O_4$ thin films prepared by different deposition techniques', DPG spring meeting, Dresden (2014), Poster
- C. Klewe et al., 'Static proximity effect in FM/Pt bilayers investigated by XRMR: Variation of energy and FM material', Spincaloritronics 6, Bad Irsee (2014), Poster
- Organizer of the SpinCaT PhD workshop, Bielefeld (2014)

- C. Klewe et al., 'Interface spin polarization in magnetic metal/Pt bilayers investigated by XRMR: Variation of photon energies and magnetic profile models', 59th Annual Magnetism and Magnetic Materials Conference, Honolulu (2014, Talk
- C. Klewe et al., 'Interface spin polarization in FM/Pt bilayers investigated by XRMR', DPG spring meeting, Berlin (2015), Talk

List of abbreviations

AFM	Atomic force microscopy
AGM	Alternating gradient field magnetometry
AHE	Anomalous Hall effect
AiMR	Anisotropic interface magnetoresistance
AMR	Anisotropic magnetoresistance
ANE	Anomalous Nernst effect
CFO	Cobaltferrite - $CoFe_2O_4$
CVD	Chemical vapor deposition
DLI	Direct-liquid-injection
DMF	N,N-dimethylformamide
DOS	Density of states
EDX	Energy-dispersive x-ray spectroscopy
EXAFS	Extended x-ray absorption fine structure
FDMNES	Finite difference method - near edge structure
FM	Ferromagnet
FMI	Ferromagnetic insulator
FMM	Ferromagnetic metal
ip	in-plane rotation of the magnetic field
ISHE	Inverse spin Hall effect
LSSE	Longitudinal spin Seebeck effect
MAO	$MgAl_2O_4$
MFP	Mean-free-path
MOKE	Magnetooptic Kerr effect
MPE	Magnetic proximity effect
MR	Magnetoresistance
NFO	Nickelferrite - $NiFe_2O_4$
NM	Non-ferromagnetic metal

OMR	Ordinary magnetoresistance
oopj	out-of-plane rotation around the current direction j
oopt	out-of-plane rotation around the transverse axis t
PLD	Pulsed laser deposition
RKKY	Rudermann-Kittel-Kasuya-Yosida interaction
RMS	Root mean square
RT	Room temperature
SEM	Scanning electron microscopy
SHE	Spin Hall effect
SMR	Spin Hall magnetoresistance
SOC	Spin orbit coupling
TEY	Total electron yield
TFY	Total fluorescence yield
uhv	Ultra high vacuum
VSM	Vibrating sample magnetometry
XANES	X-ray absorption near-edge structure
XAS	X-ray absorption spectroscopy
XMCD	X-ray magnetic circular dichroism
XMLD	X-ray magnetic linear dichroism
XPS	X-ray photoelectron spectroscopy
XRD	X-ray diffraction
XRF	X-ray fluorescence
XRMR	X-ray resonant magnetic reflectivity
XRMS	X-ray resonant magnetic scattering
XRR	X-ray reflectivity
YAG	Yittrium aluminium garnet
YIG	Yittrium iron garnet

Danksagung

Für die Unterstützung die ich beim Erstellen dieser Arbeit erhalten habe, bin ich zahlreichen Menschen zu großem Dank verpflichtet. An dieser Stelle möchte ich einigen von ihnen meinen besonderen Dank aussprechen.

Allen voran danke ich meinem Doktorvater Prof. Dr. Günter Reiss und Dr. Jan Schmalhorst, die es mir ermöglicht haben meine Arbeit in ihrer Gruppe durchzuführen und die mich während dieser Zeit durchgängig hervorragend betreut haben.

Besonders hervorheben möchte ich an dieser Stelle auch meinen Betreuuer Dr. Timo Kuschel für seine tatkräftige Unterstützung bei meinen Untersuchungen. Mit zahlreichen wissenschaftlichen Diskussionen, Ratschlägen und Anregungen hat er wesentlich zum Erfolg dieser Arbeit beigetragen.

Für die hervorragende Zusammenarbeit auf dem Thema der Spin Kalorik bedanke ich mich auch bei meinen Kollegen Alexander Böhnke und Daniel Meier, die ebenfalls in diesem Bereich arbeiten und mir durch ihr Teamwork oft eine große Hilfe waren.

Konstantinos Kontotolis und Panagiota Bougiatioti danke ich für ihre Hilfe bei den Untersuchungen zum SMR.

Für seine große Hilfsbereitschaft und die verständnisvolle Unterstützung bei jeglichen technischen Problemen mit den verwendeten Apparaturen danke ich Dr. Karsten Rott.

Für die Hilfe bei allen Verwaltungsaufgaben danke ich Aggi Windmann.

Für die sehr angenehme und stets hilfsbereite Arbeitsatmosphäre danke ich allen Mitgliedern von D2, insbesondere meinen Bürokollegen Christian Sterwerf, Lars Helmich, und Alexander Böhnke. Desweiteren danke ich auch meinen guten Kollegen Niclas Teichert, Alessia Niesen, Stefan Niehörster, Manuel Glas, Panagiota Bougiatioti, Orestis Manos, Robin

Silber, sowie meinen ehemaligen Kollegen Frank Wittbracht, Peter Hedwig und Kathrin Eckstedt dafür, dass sie mir die Zeit auf D2 sowohl in Bezug auf meine Arbeit als auch zwischenmenschlich sehr angenehm gestaltet haben.

Desweiteren Danke ich Prof. Dr. Arunava Gupta, der mir die Möglichkeit gegeben hat während eines dreimonatigen Aufenthalts in seiner Gruppe an der University of Alabama zu arbeiten. Die Arbeit in seiner Gruppe hat mir einen guten Einblick in die Herstellung und Charakterisierung von Nickelferrit und den Einstieg in meine Untersuchungen ermöglicht.

Desweiteren möchte ich mich bei all meinen Co-Autoren bedanken, die sowohl durch wissenschaftliche Diskussionen und Anregungen, als auch durch wichtige Messungen zu meinen Veröffentlichungen beigetragen haben.

Ich danke der Deutschen Forschungsgemeinschaft (DFG) für Ihre finanzielle Unterstützung im Rahmen des Schwerpunktsprograms Spin Caloric Transport (SPP 1538).

Großer Dank gilt auch den Gutachtern meiner Dissertation, die sich sehr kurzfristig dazu bereit erklärt haben meine Arbeit zu bewerten und meiner Disputation beizusitzen.

Mein größter Dank gilt aber vor allem meiner Familie und meinem engsten Freundeskreis. Sie haben mir sowohl während meines Studiums als auch während meiner Doktorandenzeit immer zur Seite gestanden und mich mit großem Verständnis unterstützt.